REPORT DOCUMENTATION PAGE

The public reporting burden for this collection of information is estimated to average 1 hour per response, including the time for reviewing instructions, searching existing data sources, gathering and maintaining the data needed, and completing and reviewing the collection of information. Send comments regarding this burden estimate or any other aspect of this collection of information, including suggestions for reducing the burden, to the Department of Defense, Executive Services and Communications Directorate (0704-0188). Respondents should be aware that notwithstanding any other provision of law, no person shall be subject to any penalty for failing to comply with a collection of information if it does not display a currently valid OMB control number.
PLEASE DO NOT RETURN YOUR FORM TO THE ABOVE ORGANIZATION.

1. REPORT DATE (DD-MM-YYYY)	2. REPORT TYPE	3. DATES COVERED (From - To)
21-08-2005	Final Technical Report	From 15-06-2002 to 14-06-2005

4. TITLE AND SUBTITLE	5a. CONTRACT NUMBER
Combustion Control in Industrial Multi-Swirl Stabilized Spray Combustor	02PR12898-01

5b. GRANT NUMBER
N00014-02-1-0756

5c. PROGRAM ELEMENT NUMBER

6. AUTHOR(S)
Gutmark, Ephraim J.
Li, Guoqiang

5d. PROJECT NUMBER
02PR12898-01

5e. TASK NUMBER

5f. WORK UNIT NUMBER

7. PERFORMING ORGANIZATION NAME(S) AND ADDRESS(ES)
University of Cincinnati
305 Clifton Ave
Cincinnati, OH 45221-0627

8. PERFORMING ORGANIZATION REPORT NUMBER

9. SPONSORING/MONITORING AGENCY NAME(S) AND ADDRESS(ES)
Office of Naval Research
Ballston Centre Tower One
800 North Quincy Street
Arlington VA 22217-5660

10. SPONSOR/MONITOR'S ACRONYM(S)
ONR

11. SPONSOR/MONITOR'S REPORT NUMBER(S)

12. DISTRIBUTION/AVAILABILITY STATEMENT
Publicly Available

13. SUPPLEMENTARY NOTES

14. ABSTRACT
The focus of this study is to investigate the emission characteristics and combustion dynamics of multiple swirl spray combustors either in premixing or non-premixed combustion (e.g. Lean Direct Injection), and correlate these combustion characteristics (emissions, combustion instability and lean flammability) to the fluids dynamics (flow structures and its evolution). This study covers measurement of velocity flow field, temperature field, and combustion under effects of various parameters, including inlet flow Reynolds number, inlet air temperature, swirl configurations, downstream exhaust nozzle contraction ratios, length of mixing tube. Knowledge obtained through this comprehensive study is applied to passive and active controls for improving gas turbine combustion performance in the aid of novel sensor and actuator technologies.

15. SUBJECT TERMS
Combustion Dynamics, Emissions, Control

16. SECURITY CLASSIFICATION OF:			17. LIMITATION OF ABSTRACT	18. NUMBER OF PAGES	19a. NAME OF RESPONSIBLE PERSON
a. REPORT	b. ABSTRACT	c. THIS PAGE			Ephraim J. Gutmark
U	U	U	U	97	19b. TELEPHONE NUMBER (Include area code) 513-556-1227

INSTRUCTIONS FOR COMPLETING SF 298

1. REPORT DATE. Full publication date, including day, month, if available. Must cite at least the year and be Year 2000 compliant, e.g. 30-06-1998; xx-06-1998; xx-xx-1998.

2. REPORT TYPE. State the type of report, such as final, technical, interim, memorandum, master's thesis, progress, quarterly, research, special, group study, etc.

3. DATES COVERED. Indicate the time during which the work was performed and the report was written, e.g., Jun 1997 - Jun 1998; 1-10 Jun 1996; May - Nov 1998; Nov 1998.

4. TITLE. Enter title and subtitle with volume number and part number, if applicable. On classified documents, enter the title classification in parentheses.

5a. CONTRACT NUMBER. Enter all contract numbers as they appear in the report, e.g. F33615-86-C-5169.

5b. GRANT NUMBER. Enter all grant numbers as they appear in the report, e.g. AFOSR-82-1234.

5c. PROGRAM ELEMENT NUMBER. Enter all program element numbers as they appear in the report, e.g. 61101A.

5d. PROJECT NUMBER. Enter all project numbers as they appear in the report, e.g. 1F665702D1257; ILIR.

5e. TASK NUMBER. Enter all task numbers as they appear in the report, e.g. 05; RF0330201; T4112.

5f. WORK UNIT NUMBER. Enter all work unit numbers as they appear in the report, e.g. 001; AFAPL30480105.

6. AUTHOR(S). Enter name(s) of person(s) responsible for writing the report, performing the research, or credited with the content of the report. The form of entry is the last name, first name, middle initial, and additional qualifiers separated by commas, e.g. Smith, Richard, J, Jr.

7. PERFORMING ORGANIZATION NAME(S) AND ADDRESS(ES). Self-explanatory.

8. PERFORMING ORGANIZATION REPORT NUMBER. Enter all unique alphanumeric report numbers assigned by the performing organization, e.g. BRL-1234; AFWL-TR-85-4017-Vol-21-PT-2.

9. SPONSORING/MONITORING AGENCY NAME(S) AND ADDRESS(ES). Enter the name and address of the organization(s) financially responsible for and monitoring the work.

10. SPONSOR/MONITOR'S ACRONYM(S). Enter, if available, e.g. BRL, ARDEC, NADC.

11. SPONSOR/MONITOR'S REPORT NUMBER(S). Enter report number as assigned by the sponsoring/ monitoring agency, if available, e.g. BRL-TR-829; -215.

12. DISTRIBUTION/AVAILABILITY STATEMENT. Use agency-mandated availability statements to indicate the public availability or distribution limitations of the report. If additional limitations/ restrictions or special markings are indicated, follow agency authorization procedures, e.g. RD/FRD, PROPIN, ITAR, etc. Include copyright information.

13. SUPPLEMENTARY NOTES. Enter information not included elsewhere such as: prepared in cooperation with; translation of; report supersedes; old edition number, etc.

14. ABSTRACT. A brief (approximately 200 words) factual summary of the most significant information.

15. SUBJECT TERMS. Key words or phrases identifying major concepts in the report.

16. SECURITY CLASSIFICATION. Enter security classification in accordance with security classification regulations, e.g. U, C, S, etc. If this form contains classified information, stamp classification level on the top and bottom of this page.

17. LIMITATION OF ABSTRACT. This block must be completed to assign a distribution limitation to the abstract. Enter UU (Unclassified Unlimited) or SAR (Same as Report). An entry in this block is necessary if the abstract is to be limited.

Final Technical Report for Office of Naval Research

N00014-02-1-0756

Combustion Control in

Industrial Multi-Swirl Stabilized Spray Combustor

Dr. Ephraim J. Gutmark

Dr. Guoqiang Li

University of Cincinnati

Aug. 21, 2005

ABSTRACT

The focus of this study is to investigate the emission characteristics and combustion dynamics of multiple swirl spray combustors either in premixing or non-premixed combustion (e.g. Lean Direct Injection), and correlate these combustion characteristics (emissions, combustion instability and lean flammability) to the fluids dynamics (flow structures and its evolution). This study covers measurement of velocity flow field, temperature field, and combustion under effects of various parameters, including inlet flow Reynolds number, inlet air temperature, swirl configurations, downstream exhaust nozzle contraction ratios, length of mixing tube. Knowledge obtained through this comprehensive study is applied to passive and active controls for improving gas turbine combustion performance in the aid of novel sensor and actuator technologies.

Emissions and combustion characteristics are shown closely related to the shape and size of central recirculation zone (CRZ), the mean and turbulence velocity and strain rate, and dynamics of large vortical structures. The passive controls, mostly geometry factors, affect the combustion characteristics and emissions through their influences on flow fields, and consequently temperature and radical fields. Air assist, which is used to adjust the momentum of fuel spray, is effective in reducing NO_x and depress combustion oscillation without hurting LBO. Fuel distribution/split is also one important factor for achieving low NO_x emission and control of combustion dynamics. The dynamics of combustion, including flame oscillations close to LBO and acoustic combustion instability, can be characterized by OH*/CH* radical oscillations and phase-locked chemiluminescence imaging. The periodic fluctuation of jet velocity and formation of large vortical structures within CRZ are responsible for combustion instability in multiple swirl combustors.

1. INTRODUCTION

The combustion dynamics, including combustion instability or lean combustion stability, pose challenges for conventional diffusion combustion systems and especially, for modern lean burn combustion systems. The occurrence of dynamics in diffusion flames can be depressed by modification of fueling system or carefully scheduling operating conditions by calibration. But for premixed combustors, the dynamics are more persistent and can only be damped partially by empirical tools and controls (Mongia, et al. 2003). For DLE engine, the instability was observed at equivalence ratio 0.55 (Pandalai and Mongia, 1998) based on its design and operating features. DLE engines have stronger corner recirculation zones and smaller central recirculation zone compared with conventional Single Annular Combustor (SAC) (Pandalai and Mongia, 1998). It is also interesting to notice that the flame instability improved when central recirculation zone was either absent or minimal for certain design. The reduction of central recirculation may eliminate the PVC and avoid the potential oscillation from PVC dynamics of premixed combustion. The coupling between heat release and acoustics pressure fields (also called thermo-acoustic instability) are normally recognized as the mechanism for driving combustion instability; lean combustion instability are mostly caused by local flame extinction and re-ignition when fuel/air ratio approaches lean burn limit. These two types of dynamics can also occur simultaneously.

The driven mechanism for thermo-acoustic combustion dynamics can be categorized into two groups according to Mongia et al. (2003). First category, which is often associated with high frequency (>1 kHz), is the coupling between the pressure oscillation and the instantaneous flame position and shape as the flame surface responds to the pressure disturbance. The second is the coupling between pressure oscillation and local fuel/air ratio, with frequency ranged from 100 to

1000 Hz. Several sub-mechanisms can affect local fuel/air ratio, including fuel line/air feeding perturbation and unsteady flow structures. Also, according to the source term, i.e. which one comes first as to heat flux and pressure oscillation, Ducruix et al. (2003) classify the driven mechanisms into: flame/boundary interaction, flame/vortex interaction, in which heat flux leads pressure oscillation, flame response to acoustic wave, and unsteady strain rate and equivalence ratio fluctuation, in which these unsteady parameters cause pressure or/and velocity fluctuation and finally heat release fluctuation. It is hard to isolate one from the other among all these mechanisms. For instance, the oscillation in fuel/air equivalence is possibly caused by dynamics of large vortical structure and consequently results in heat release oscillation.

For swirl-dump gas turbine combustors, the large vortical structures formed in the dump plane and within central recirculation zone (PVC) are likely to be the driven source of combustion instability provided certain phase relation with flame satisfied. Strong instability occurs when the shear layer preferred mode frequency matches the chamber acoustic resonant frequency (Schadow and Gutmark et al, 1992) or the vortex shedding frequency coupled with one of the acoustic mode of inlet duct (Poinsot et al. 1992). For a dump combustor, Poinsot et al. observed that vortex shed from the dump plane when the velocity oscillation was the maximum and this vortex caused flame periodic change when traveling downstream.

Large-scale structures, such as PVC mentioned above and large coherent structure associated with shear layer instability, play an important role in the mixing between fuel and air. The dynamical nature of these structures controls the dynamics of combustion and heat release process. The thermo-acoustic instability is therefore strongly dependent on the dynamical large-scale structures. The temporal and spatial evolution of large coherent structures in shear layer is reasonably well understood for simple flows such as mixing layers (Ho and Huang, 1982), shear

layers (Ho and Huerre, 1984), jets (Hussain, 1983), and even back-step flows (Hasan, 1992), but in more complex, multi-phase flows (such as sprays) this behavior is not as well understood. Recent research conducted by Paschereit et al. (1998, 2000) investigated and controlled unstable thermoacoustic modes in an experimental low-emission swirl stabilized combustor, in which several axisymmetric and helical unstable modes were identified for fully premixed and diffusion combustion. These unstable modes were associated with flow instabilities related to the recirculation wake-like region on the combustor axis and shear layer instabilities at the sudden expansion (dump plane). Sivasegaram and Whitelaw (1991) showed that swirl reduced instability for disk-stabilized combustion, but increased the instability for flames stabilized behind sudden expansions and annuli with a small clearance at the wall. Unlike the large body of literature dealing with control of non-swirling gaseous flames, there is less work reported on the control of swirling combustion, especially in the presence of multi swirlers. To control swirl induced/modified instability, and to enhance the combustion performance, controlling or manipulating the large-scale structures and the interaction between fuel and these structures is of critical importance.

Flame off in lean burn combustion is an important issue and obtained increasing attention recently. Early detection and proper control is the key to extend and prevent Lean Blow Off (LBO). Muruganandam et al. (2003) identified the precursor of LBO by setting up a threshold for OH* or CH* signal and counting the times these signals over the threshold based on the observation that normally the flame tends to get stronger oscillation approaching LBO. This approach has been tested on gaseous and liquid fuel for swirl-stabilized combustor at Georgia Tech. It was demonstrated that LBO was extended by adding more pilot fuel. But the sacrifice of

NO_x emission was not clearly stated in this study. Acoustic detection of LBO is study by Nair and Lieuwen (2003) with similar statistical approach.

Considerable amount of work in the area of passive and active combustion dynamics control for gaseous and liquid fueled combustion has been reported during the last two decades (Gutmark, et al., 1992; McManus et al., 1993; Annaswamy and Ghoniem, 1995). Studies reported in these reviews have dealt mostly with bluff-body-stabilized combustor and dump combustors where the recirculation induced by a bluff-body or by a sudden expansion was used to stabilize the flame, and were more recently extended to swirl stabilized combustors (Paschereit, Gutmark, and Weisenstein, 2000). Active control strategies have been used to suppress thermo-acoustic instabilities in the combustors. These control strategies have generally relied on modulating the fuel injection and phase shifting it so as to decouple the pressure oscillation and heat release with respect to each other. Control strategies have also looked at improving fuel efficiency and reducing pollutants (Paschereit, Gutmark, and Weisenstein, 2000) and in extending flammability limits (Gutmark et al., 1990).

The major goals of the proposal:

2. EXPERIMENTAL SETUP

2.1 Experimental Facilities

2. 1.1. Triple Annular Research Swirler

A Triple Annular Research Swirler (TARS) was developed to apply the concept of variable nozzle geometry by Delavan Gas Turbine Products (DGTP, a division of Goodrich Aerospace) with the collaboration of General Electric Aerospace Engines (GEAE). To simulate Dry Low Emission (DLE) combustor, all the air needed for combustion flows through the fuel injector and no additional dilution air is provided. When a short section of mixing tube inserted between TARS and combustion chamber, the combustor will simulate DLE combustor; without mixing tube it more ensembles Lean Direct Injection combustor.
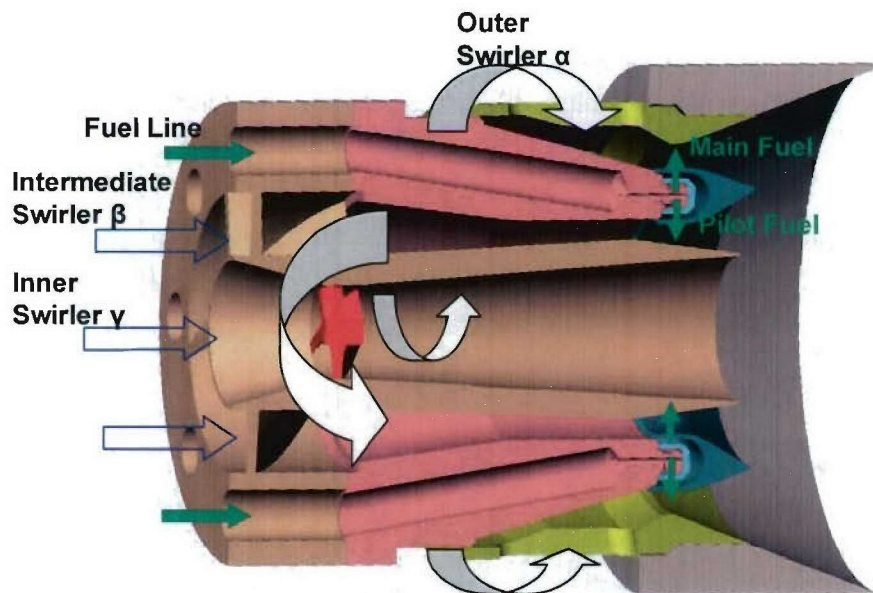
Figure 2.1 Triple Annular Research Swirler with its fuel circuits.

TARS (Fig. 2.1) features three air passages with each passage having its own swirler that can be changed independently. Different configurations of TARS can be formed by changing the

swirlers---outer swirler α, intermediate swirler β, and inner swirler γ--- either to different swirling angles or different rotating directions, to form different swirling flow fields (for instance, some configurations are listed as Fig. 2.2). The inner and intermediate swirlers are axial swirlers whereas the outer swirler is a radial one. Hereafter, the swirler configuration will be labeled with the swirler angle in the order of outer, intermedicate and inner, and with "C" labeling the counter-rotating swirl direction. For example, S5545C45 means that the swirler configuration has 55° outer swirler, 45° intermediate swirler in counter-rotating direction and 45° inner swirler.

Inner Swirler			
	30°, 4 vanes, CCW	45°, 4 vanes, CCW	45°, 4 vanes, CW
Intermediate Swirler			
	30°, 8 vanes, CCW	45°, 4 vanes, CCW	45°, 4 vanes, CW
Outer Swirler			
	30°, 8 vanes, CCW	55°, 8 vanes, CW	30°, 8 vanes, CW

Figure 2.2 Different inter, intermediate and outer swirler configurations with co-rotating rotating (CW) and counter-rotating (CCW) (not all configurations listed here).

Two sets of distributed liquid fuel injection circuits are integrated within TARS assembly: pilot fuel circuit injects fuel inward into the intermediate swirling air passage and the main fuel circuit injects fuel outward into the outer swirling air passage. The pilot and main fuel was separated inside the cone of the fuel nozzle. The fuel was first injected through 13 mil diameter holes in the dome inside the cone and then through the 30 mil diameter holes on the cone that separates the outer and intermediate swirling air. The number of injection holes for the pilot and main fuel is four and eight, respectively. All fuel injection holes were identical in size for pilot and main fuel, with flow number of 0.0017 $kg \cdot s^{-1} \cdot Mpa^{-1/2}$ (calibrated on Mil-C-7024 with density of 762 kg/m^3). Another important feature of this nozzle/swirler assembly is the design of air-assist system. There are two air-assist lines that are inserted into the fuel nozzle, feeding small amount of air to premix the liquid fuel inside the cone. The mixture of air and fuel was injected through the 30 mil holes. This design provides the controllability of fuel outgoing momentum through the modulation of the air assist, which is investigated in this study as an active control method for combustion dynamics and emissions. These two air-assist lines can also be used as fuel supply lines for gaseous fuel. In that case, the gaseous fuel occupies total 12 injection holes.

2.1.2. Combustion Test Rig

The atmospheric combustion test rig for TARS is depicted in Fig. 2.3. The combustor is set up vertically with the air fed from below, preheated by a 36kW electrical heater and conditioned by a set of fine mesh screens and a honeycomb straightener that are installed sequentially in the air conditioning chamber. Static pressure transducer (Druck PMP 4000 series, ±0.04%FS accuracy, 1psi range) and type K thermocouple were mounted on this chamber to monitor the pressure drop, dynamics pressure oscillation, and inlet air temperature, respectively. TARS is
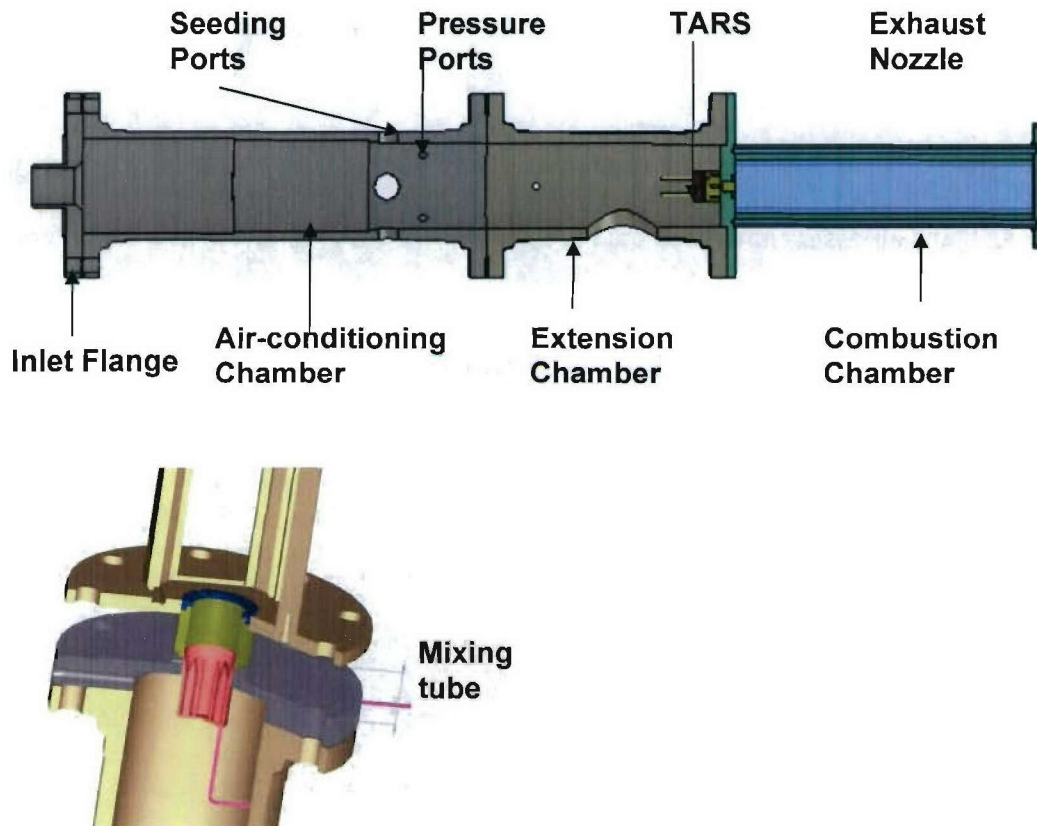
Figure 2.3 .Combustion test rig for TARS and the enlargement view of mixing tube.

centered in a mounting plate that is installed in a 6" inner diameter plenum chamber. Downstream of TARS, a cylindrical section of the mixing tube may be inserted between the TARS exit and combustion chamber inlet to form mixing duct for fuel/air and configure the test rig into a pre-mixed combustor. The combustion chamber is 45.7 cm long, with four flat walls assembled by four posts to form an octagon shape cross-section. The walls can be made either of quartz glass to allow optical access and OH/CH chemiluminescence monitoring of the flame, or an instrumentation plate for installation of pressure transducers and thermocouples. The cross sectional area of this chamber is identical to that used in the cold flow tests, a 10cm inner diameter cylindrical tube. A circular exhaust nozzle is mounted downstream of the combustion

chamber as a contraction for the exhaust combustion gas. Circular quartz tube (4" in diameter) was also used as the combustion chamber to provide full view of the flame for chemiluminescence and video imaging.

A fuel supply system was designed to supply, control and meter the flow rates of the pilot fuel, main fuel, and air-assist flow. The liquid fuel (Ethanol or Jet-A) is stored in a stainless steel tank that is pressurized by nitrogen up to 160 psi. The fuel is delivered to a main control valve and turbine flow meter (Hoffer Mini-Flow meter, MF1/70B, ±1% accuracy FS) and then split into the pilot and main fuel branches, with each having its own controller and on-off valve. Another turbine flow meter was installed on the main fuel line to meter the fuel split between main and pilot fuel circuits. The air-assist flow is regulated to 30 psi and controlled by a needle valve and metered by a digital gas flow meter (Alicat M series, ±1% FS accuracy). This meter can also meter the flow rate of gaseous fuel, such as propane and natural gas. This fuel metering system is fully digitalized and is ready for integrated into a data acquisition system.

Different types of pressure transducers have been used for this study. Normally, a water-cooled Kistler piezoelectric pressure transducer (Model 7061B with charge amplifier 5010B) was mounted on the wall 5 cm above the inlet plane of combustion chamber to monitor the oscillations of pressure. When optical tube was used as the combustion chamber, a Brüel & Kjær microphone (Model 4939-A-011) was set up 0.5m away from the combustor to detect the pressure oscillations. The static pressure transducer mounted on the plenum chamber can also detect pressure oscillations in addition to the static pressure. This signal is used for measuring flow oscillations of the inlet section of the combustion chamber.

Two types of combustion gas analyzer have been used in this four years span study. Most of the emission data of the octagon shape combustor were from IMR 3000P electrochemical gas

analyzer. The sampling probe was inserted 40cm above the inlet plane and centered on the centerline. CO, NO, NO_2 (there two items are combined to NO_x hereafter), and O_2 are analyzed independently. This analyzer has ±2 ppm accuracy for CO and NOx.

The second system is basically an extractive sample conditioning and control system, which provides a representative sample to a chemiluminescent NOx monitor and an infrared CO monitor with an installed paramagnetic O2 sensor. The system has 10ppb resolution for NO/NOx, 0.1ppm for CO, 0.1% for CO2 and O2. The sampling probe is heated to above 100°C for eliminating water vapor from the sample. The CO analyzer is designed to be in serial arrangement using a pneumatic type differential sensor to minimize the interference from CO_2 or water vapor. For the operating principle please refer to the book written by Jahnke (2000).

All the process parameters, including main air flow rate (m_a, in SCFM), air inlet temperature (T_3, in °C), plenum pressure (p_3, in psi), pressure inside combustion chamber (p_4, in psi), combustion temperature (T_4, in °C) , combustor wall temperature (T_w, in °C), total fuel flow rate (W_f, in GPM), liquid fuel split (fuel flow rate between main and total) are recorded by Labview program, as well as emission data from gas analyzer. The dynamic data, including pressure, optical signals, are recorded at 5000Hz simultaneously.

2.1.3. Setup for Laser Diagnostics

Particle Image Velocimetry

Stereoscopic PIV system (TSI) was used to measure the flow field in the combustion chamber and investigate the influences to the flow fields from swirler configurations, mixing tube length, air flow rate, and exhaust nozzle diameter. The system included: two 120 mJ 15 Hz pulse Nd-Yag laser (New Wave Research Gemini PIV laser Model 120-15), signal synchronizer
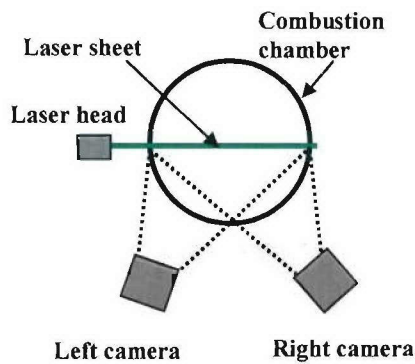
(a) PIV setup for streamwise plane
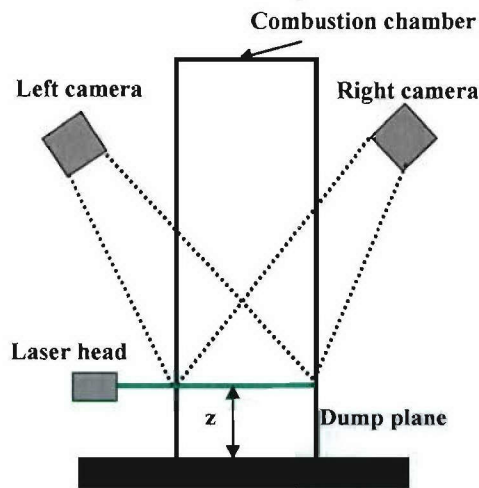
(b) PIV setup for cross-sectional plane

Figure 2.4: Experimental setup for PIV measurement on (a) streamwise plane and (b) cross sectional plane.

(Model 610034), two 2048x2048 pixels 12-bit Powerview CCD cameras (Model 630049), and two high performance frame grabbers (Model 600069). The 4mm diameter laser beam from the laser head formed a laser sheet by a cylindrical lens (Focus Length = -15mm or -25 or combination of two) and a spherical lens (Focus Length =500mm). The laser sheet has a width of 130mm at the waist location and thickness of about 1mm, overlapping the centerline of the combustion chamber.

For streamwise plane measurement, the two CCD cameras were mounted on the same sides of the laser sheet with a separation angle of 30°, focusing on the field of view created by the pulsed laser sheet on the streamwise plane (Figure 2.4a). Based on the calculation of the displacement of pixels between two laser pulses (for this experiment this laser pulse interval was set between 6 μs to 12 μs), radial velocity (V_r) and axial velocity (V_z) were obtained with units of pixels per second. To obtain the third velocity component, which is perpendicular with the laser sheet, a calibration procedure was applied to generate the correlation

equation by imaging several (normally two) planes with different depth in the perpendicular direction.

For cross-sectional plane measurement, the two cameras are looking from above with a separation angle of 60°. Because the camera only has one perspective angle adjustment, the centerline of the combustor chamber and the centerlines of the camera lens have to be in the same plane, as shown in Fig. 2.4b.

2.1.4. Optical Fiber Detector

Optical fibers are used for monitoring the dynamic signals of flame. The light emitted by the flame was received by the optical fiber in a narrow cone angle of about 23°. The light is filtered by narrow band pass filters, then amplified and converted to voltage signal by a photomultiplier tube (PMT). Filter centered at 308nm is used for OH* radical and 430nm for CH* radical. The optical fiber can be put outside the combustion chamber horizontally monitoring the flame or integrated into the fuel nozzle looking the flame vertically along the flow direction. For the fiber integrated TARS (Fig. 2.5), a bundle of PMT with four OH* channels and three CH* channels was assembled by Goodrich Sensing Technology Department. Fibers are installed at four locations: OH*/CH*_CRZ labels the fiber at the centerline of the nozzle; OH*/CH* 2 and OH*/CH*3 and OH*4 are the fibers circumferentially installed on the expansion cone of outer swirler. The angle between the three circumferential fibers is about 120°.

2.1.7. OH* and CH* Chemiluminescence Imaging

We use intensified CCD camera (Roper Scientific Super Blue 1024x1024 pixels, 12-bit) with timing generator that can handle minimum about 2ns time delay. This camera can be used in either free run mode or gate mode that can be phase-locked with dynamic signals. Narrow band-

pass filters were used for radical chemiluminescence: 432 nm center wavelength with Full-Width Half-Maximum (FWHM) 4 nm (Omega Optical) for CH*-line ($A^2\Delta$, $v'=0 \rightarrow X^2\Pi$, $v''=0$, $\lambda=431.2$ nm); and 310.02 nm center wavelength with FWHM 10 nm (Andor 310FS10-50) for OH*-line ($A^2\Sigma+$, $v'=0 \rightarrow X^2\Pi$, $v''=0$, $\lambda=306.4$ nm).
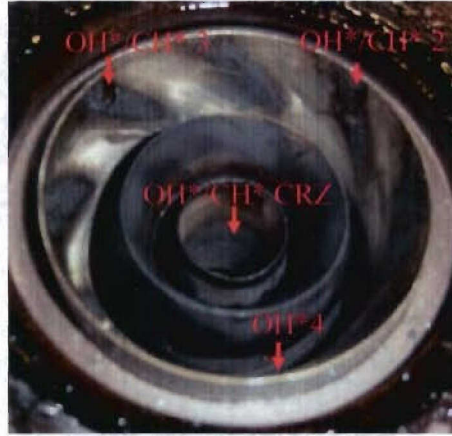
Figure 2.8: Arrangement of optical fibers integrated with the fuel nozzle.

2.2 Error analysis

The error sources for this study may come from different sources because the instrumentation involves multiple measurements of flow rate, velocity, temperature, pressure, and light emissions. The aspects of error sources are listed as following.

All the flow meters in this study have accuracy of ±1%. For fuel/air equivalence ratio, which is defined as the real fuel/air ratio versus stoichiometric, the error in fuel flow rate and air flow rate will contribute ±1.4 % by root mean square method (Moffat, 1988). The Reynolds number in this study is calculated from the air mass flow rate, fluids property (density and viscosity) and geometry. Since the error for fluids property and geometry is fairly small, the error in Reynolds number is estimated to be 1%.

Inlet air temperature is measured by type K thermocouples that have ±1°C accuracy. The combustion temperature is measured with a type B thermocouple and precision thermometer with accuracy ±0.1°C.

The error for velocity measurement by LDV is in the range lower than 1% error because the data rate was maintained about 3 kHz and 40000 samples were taken for each location. Due to the non-uniformity in seeding and reflection of laser from the confined wall, the error for PIV measurement is difficult to estimate. When these problems are minimized through iteration of laser sheet alignment and camera setup, the velocity from PIV is in the error range of ±10% compared with the LDV measurement.

The signals from optical fibers are not calibrated so the data comparison is not real quantitative but rather proportional to the light or radical intensity. Therefore, theses signals are represented as voltage instead of intensity. However, this won't affect the conclusion we will draw bases on these data because absolute value is not necessary for the comparison of parameters which are measured with the same optical setup.

The microphones used in this study, including high temperature and low temperature ones, are in the accuracy of ±0.05%. The signals detected by these microphones are sufficient for FFT analysis and comparison of RMS values.

3 DYNAMIC STRUCTURES IN SWIRLING FLOW

Swirling flow is unsteady three dimensional in nature. The large vortical structures involved in swirl-dump combustors mainly include Precessing Vortex Core (PVC) and Large Vortex Shedding from the Dump plane (LVSD). PVC was extensively investigated by research group leading by Syred and O'Doherty et al. (1974, 1997) and LSVSD by Gutmark and Shadow (1992), and Poinsot (1987). The combustion dynamics are shown closely related to these flow structures; therefore depicting dynamic flow structures for this multiple swirl flow is essential to build up the logic correlating flow structures to combustion dynamics and emissions, which are affected by combustor geometries we investigated before, namely, length of mixing tube, exhaust nozzle contraction ratio and swirler configurations.

In swirl-dump combustors, the co-existence of two different large coherent structures complicates the flow and the combustion dynamics. Time resolved flow structures and combustion dynamics have to be applied to trace these dynamics when either PVC or LSVSD or both dominates the flow and the combustion dynamics during instability occurrence. The large coherent structures in swirl-dump combustors, PVC and LVSD, were measured with phase-locked stereo PIV for isothermal flows based on the different characteristic frequencies identified by microphones. The experimental setup is shown in Fig. 2.7. Meanwhile, the flame dynamics were measured with OH* chemiluminescence that was phase-locked with pressure oscillation signals.

3.1 Precessing Vortex Core

It is not trivia to identify PVC from the complex swirling flow because the definition of PVC requires detailed measurement of instantaneous velocity fields. Syred et al. (1974) specified PVC lying *on the boundary of the mean reverse flow zone between the zero velocity and zero*

stream line. Fick et al. (1997) stated that PVC was represented by *the point of zero velocity in the tangential flow*, and this structure was displaced from the geometric axis of the burner and precessed around the axis in certain frequency, but not necessary in a circular manner but rather in a helical style. To reveal the PVC inside swirling flow field downstream of TARS, we first discuss the instantaneous vector of unconfined case and then move on to confined case with different inlet air temperatures that more ensembles the real gas turbine combustor.

3.1.1 Unconfined Swirling Flow

The simple case for revealing PVC dynamics is from unconfined isothermal flow. Velocity fields on the streamwise plane of Swirler S554545 are shown in Fig. 3.1, in which (a), (b), and (c) are instantaneous vector plots at random times t1, t2 and t3. The combustor inlet plane is located at Y=-40mm. X=0mm is at the combustor geometry centerline. Multiple large vortical structures along the winkled swirling jet shear layer are clearly shown in these instantaneous images, highlighting the three dimensional unsteady features of this complex flow. These large vortices, especially the two located near the combustor inlet, are most likely to be PVC and its associated eddies as was identified by Fick et al. (1997). The downstream evolution of this pair vortices wrinkle the swirling jet, causing its wave-like motion in instantaneous images. This pair vortices manifest as axisymmtric (Figs. 3.1a and 3.2b) or non-axisymmetric form (Fig. 3.1c), travel downstream and are visible even after 100mm (2D). The averaged vector plot smoothes out these dynamic features and depicts only the pair vortices axisymmetrically located at the inlet as normally seen from PIV averaged image. The comparison of velocity profiles at Y=10mm (about in the middle of measured flow field) for instantaneous and averaged flow fields are shown in Fig. 3.2. It can be seen that the average velocity field only partially represent this flow

in keeping the overall trends: reversed axial velocity within CRZ; Rankine vortex like profile for tangential velocity and fairly small magnitude of radial velocity. There are significant fluctuations between instantaneous velocity fields for axial, tangential, and radial components. These fluctuations governs the real time flow fields and will impact tremendously on combustion performance when local fuel/air mixing and emission optimization have to be considered for ultra-low emission gas turbine combustions.

3.1.2 Characteristics frequency of PVC

PVC is characterized by certain frequency because PVC regularly modifies flow structures and generates periodic large pressure oscillations (Fick et al., 1997, 1998). Pressure transducer mounted on the rim of combustor inlet (Fick et al, 1998) can be used detecting this pressure signal. The sensor can also be installed many burner diameters downstream of the combustor inlet (Yazdabadi et al., 1994). In this study, A low noise, high sensitivity microphone was mounted 2 cm above the combustor exit and 2 cm away from the combustion chamber wall, aligned with the chamber diameter. FFT spectral analysis of the microphone signal (sampling at 5 kHz) identified the dominant frequency f that had the peak magnitude across the spectra. Figures 4.3a and b plot this frequency (in Hz) versus R_{eD} and the characteristic frequency parameter fD^3/Q versus R_{eD}, respectively. This dominant frequency increases linearly with R_{eD} (Fig.4.3a), but slightly higher for shorter tubes (L = 40 cm and 45 cm, normalized with combustion diameter D_c as L/D_c = 4, 4.5) than that of the longer tube (L= 65 cm, L/D_c = 6.5). For tubes with similar lengths (L/D_c = 4, 4.5), the frequency lines versus Reynolds number were identical. fD^3/Q is constant for tubes with a certain length: 0.20 for L/D_c = 4, 4.5 and 0.18 for L/D_c = 6.5 . The characteristics of this frequency match closely with the observations of PVC in

swirling flows from Syred and Beer (1974), and Cassidy and Falvey (1970). They found fD^3/Q in the range of 1.0~1.5 for $S_N= 0.91 \sim 1.86$ for cyclone combustion chambers. Therefore, this frequency may be interpreted as the PVC frequency and the signal corresponding to this frequency can be used as a trigger signal to phase-lock PIV and resolve the dynamics of the PVC.
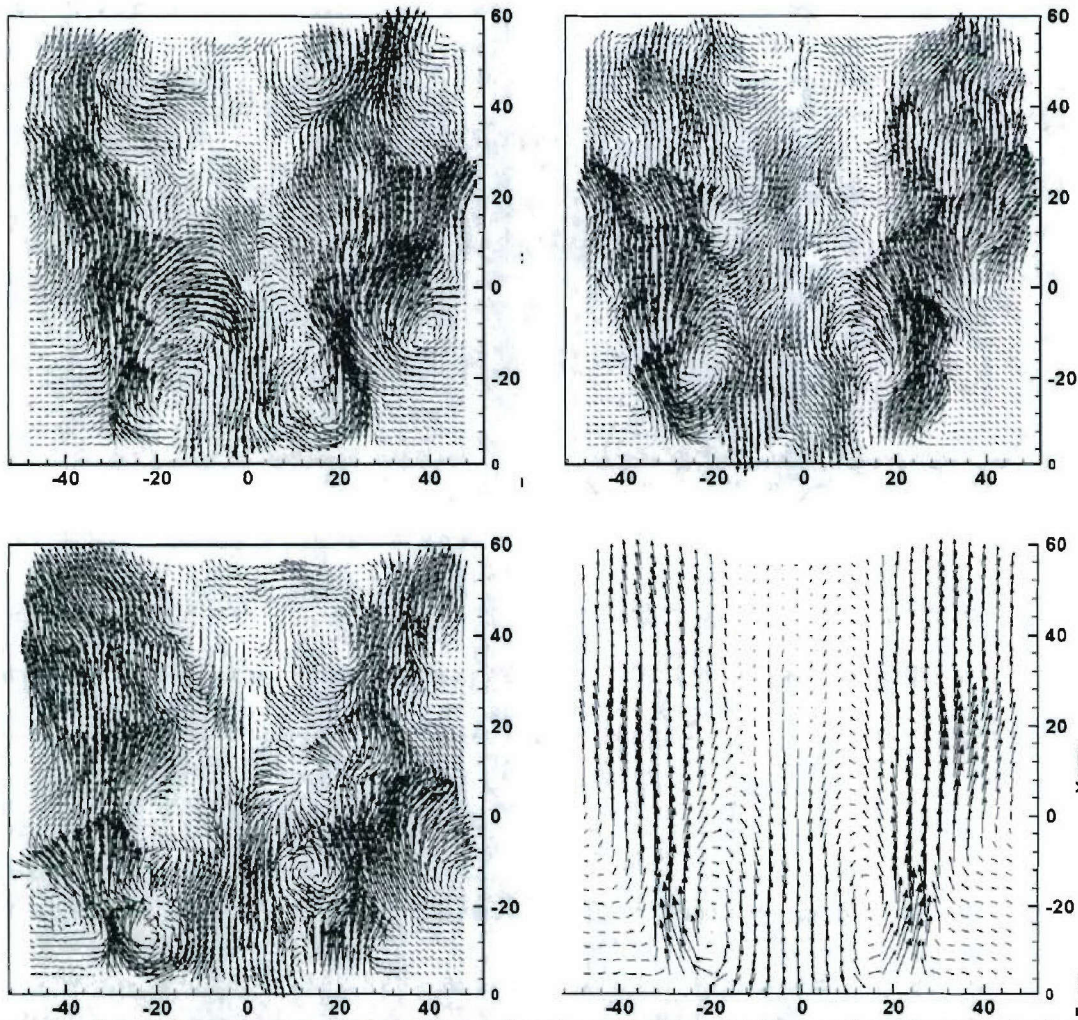
Figure 3.1: Instantaneous vector field on streamwise plane (a), (b) and (c) at random times t1, t2, t3 and (d) Averaged vector plot of unconfined case: S554545, T_{in}=25°C, R_{eD}=4.4x10^4. X is horizontal axis and Y is vertical axis in mm.

The PVC frequency is also a function of inlet air temperatures in addition to Reynolds Number
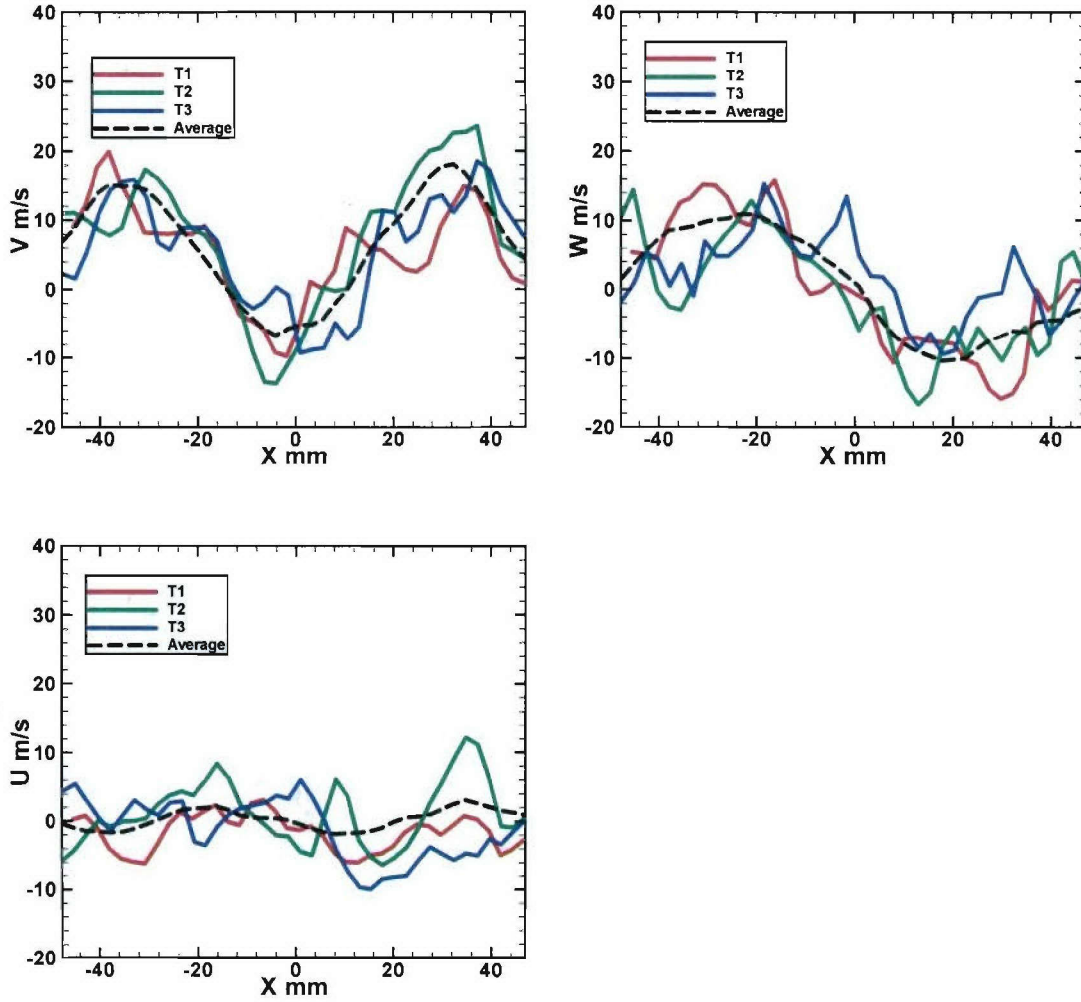
Figure 3.2: Profiles of axial (V), tangential (W) and radial (U) velocity components at Y=10mm of instantaneous vector field T1, T2, T3 and averaged vector of unconfined case: S554545, T_3=25°C, R_{eD}=4.4x10⁴.

(Fig. 3.3a). As the inlet air temperature (T_3) increased from 20°C to 400°C, the slope of the frequency versus R_{eD} became greater although there is still a linear relationship between PVC frequency and R_{eD} (Fig. 3.4a). It indicates that this frequency is more sensitive to Reynolds number when the air temperature gets higher. We also noticed that in Fig. 3.4b the normalized frequency fD^3/Q increased linearly with the inlet air temperature; but the shorter burner (L/D_c =

4) features greater slope than the longer one ($L/D_c = 6.5$). As observed in Fig. 3.3a, the frequencies fall on different lines for burners with different lengths. This disparity can be attributed to the friction effect of the wall (Syred and Beer, 1974) and it is not so significant for lower temperature than for high temperature because the viscosity effect is not so considerable for high Reynolds number flow at low temperature. As T_3 increases, the increase of air viscosity causes the Reynolds number to decrease (refer to Eq. (1)), even though the decrease of air density also causes average velocity increase. Due to the same effect of viscosity, fD^3/Q is a linear function of the air temperature (Fig. 3.4b). The change of viscosity affects the PVC characteristic frequency more at high air temperatures.
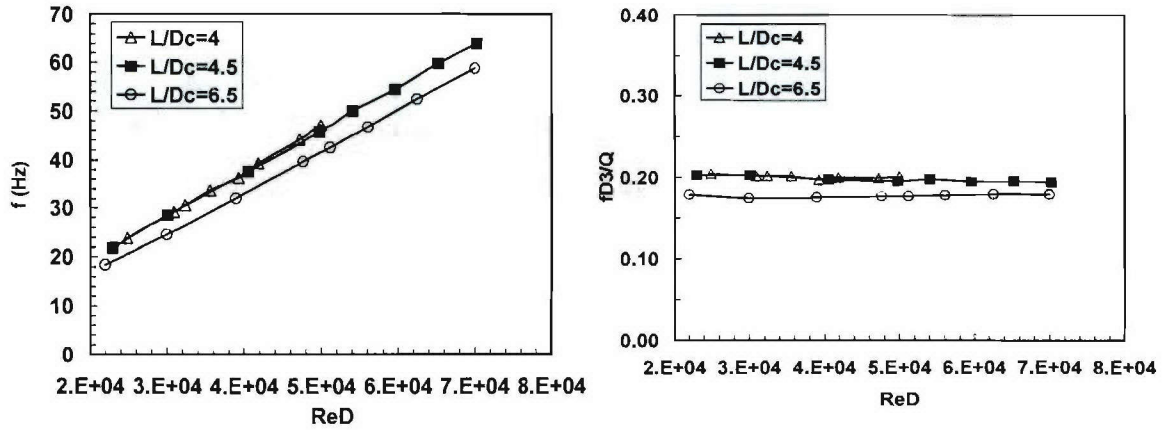
Figure 3.3: (a) Frequency of PVC versus Reynolds number (R_{eD}); and (b) frequency characteristic parameter fD^3/Q versus R_{eD} for L/D_c=4, 4.5 and 6 at T_3=20°C.

If we extrapolate the PVC frequency of $L/D_c = 4$ from the isothermal temperature to combustion temperature, the fundamental PVC frequency will be 216 Hz if assuming the combustion gas temperature to be 1400°C. When combustion occurs, the dominant frequency detected by the microphone was between 410-430Hz for stable combustion with $R_{eD} = 2\times10^4 \sim 3\times10^4$ (T_{in}=230°C, $L/D_c = 4$) while the coherent instability happened at a frequency of 414 Hz.

The coincidence of the secondary harmonics of PVC and the instability frequency may imply that PVC could possibly play a role in the instability dynamics. This point needs to be further verified by combustion dynamics discussed in later sections.

(a)   (b)
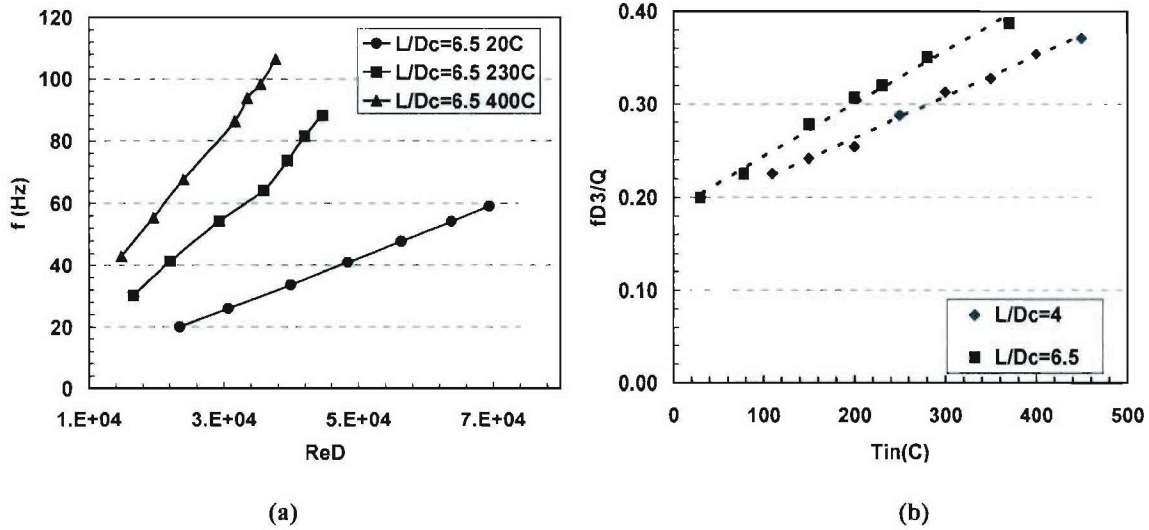
Figure 3.4: Temperature effects on the frequency of PVC: (a) frequency versus R_{eD} for T_{air}=20, 230 and 400°C, L/D_c=6.5; (b) frequency versus T_{air} for L/D_c=4, 6.5 at R_{eD} (20°C) =26,000.

3.1.3 Confined Swirling Flow

Confinement, like combustion chamber, affects the swirling flow field both in its recirculation zone shape (Fig. 4.5) and dynamic structures. The formation of corner recirculation zone helps in jet expansion and enlarges CRZ, pushing the high velocity jet against the combustor wall. The pressure signal detected by the microphone is used to generate the trigger signal for phase-locked PIV measurement. Both streamwise plane and cross-sectional plane vectors are measured to reveal PVC structure and related eddies for swirling flow in a 10cm diameter optical combustion chamber.

It is realized that the phase-averaged PIV image can smooth out some features instantaneous images depict (Fick et al., 1998) due to the helical motion of PVC and the evolutions of vortices

inside swirling flow, as is demonstrated for unconfined flow in Fig. 3.1. For confined swirling flows, the comparison between instantaneous vectors and averaged vector plots is shown in Figure 3.5. As is expected, the phase-averaged flow field shows fairly organized structure compared with instantaneous pictures: emanating jets associate with large vortices along their inner sides and these vortices shrinks when traveling downstream. Because of expansion of the CRZ, the vortices are displaced away from combustor centerline. Figure 3.5 highlights this observation with circular red dot line. The vortex formed near the combustor inlet (Fig. 3.5a) appears to peal from the jet inner side (Fig. 3.5b), moves away from the jet (Fig. 3.5c) and forms large vortical structure downstream (Fig. 3.5d).

More information of flow dynamics can be revealed from the cross-sectional measurement. On the cross-sectional plane at z/R=0.125, the instantaneous vectors show single vortex around the geometric center of the combustion chamber (Fig. 3.6). Although it is hard to distinguish the exact location of PVC, the red dotted circles highlight the different orientation of this central vortex, which is possible a manifestation of vortex precessing around the geometric center. The axis of this elliptical vortex switches from vertical to horizontal or from 135° angle to 45° angle although the phase-averaged vector shows a vortex almost perfectly located at center X=0, Y=0mm.

(a)

(b)

(c)

(d)

(e)
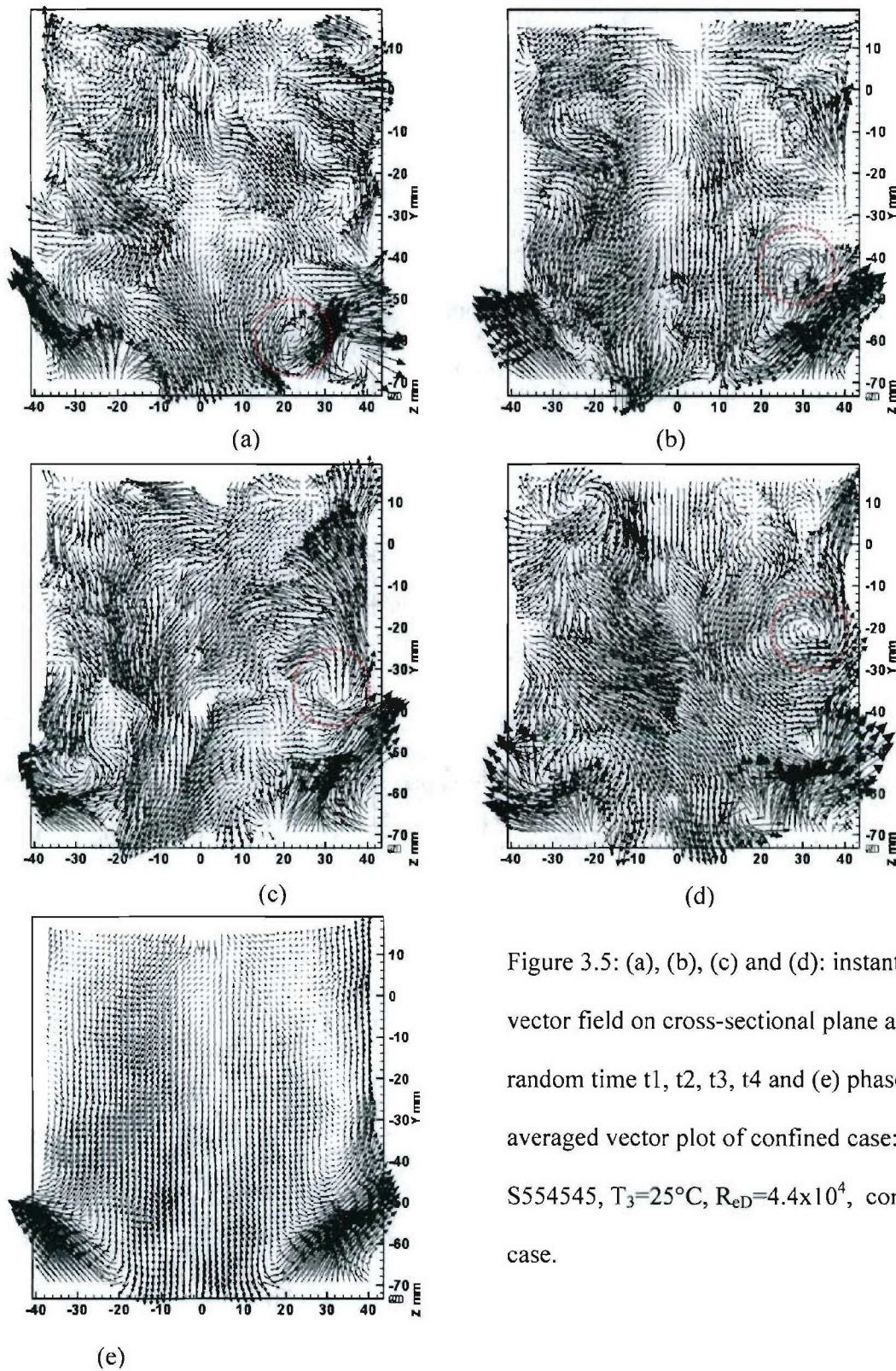
Figure 3.5: (a), (b), (c) and (d): instantaneous vector field on cross-sectional plane at random time t1, t2, t3, t4 and (e) phase-averaged vector plot of confined case: S554545, $T_3=25°C$, $R_{eD}=4.4\times10^4$, confined case.

(a)

(b)

(c)

(d)

(e)
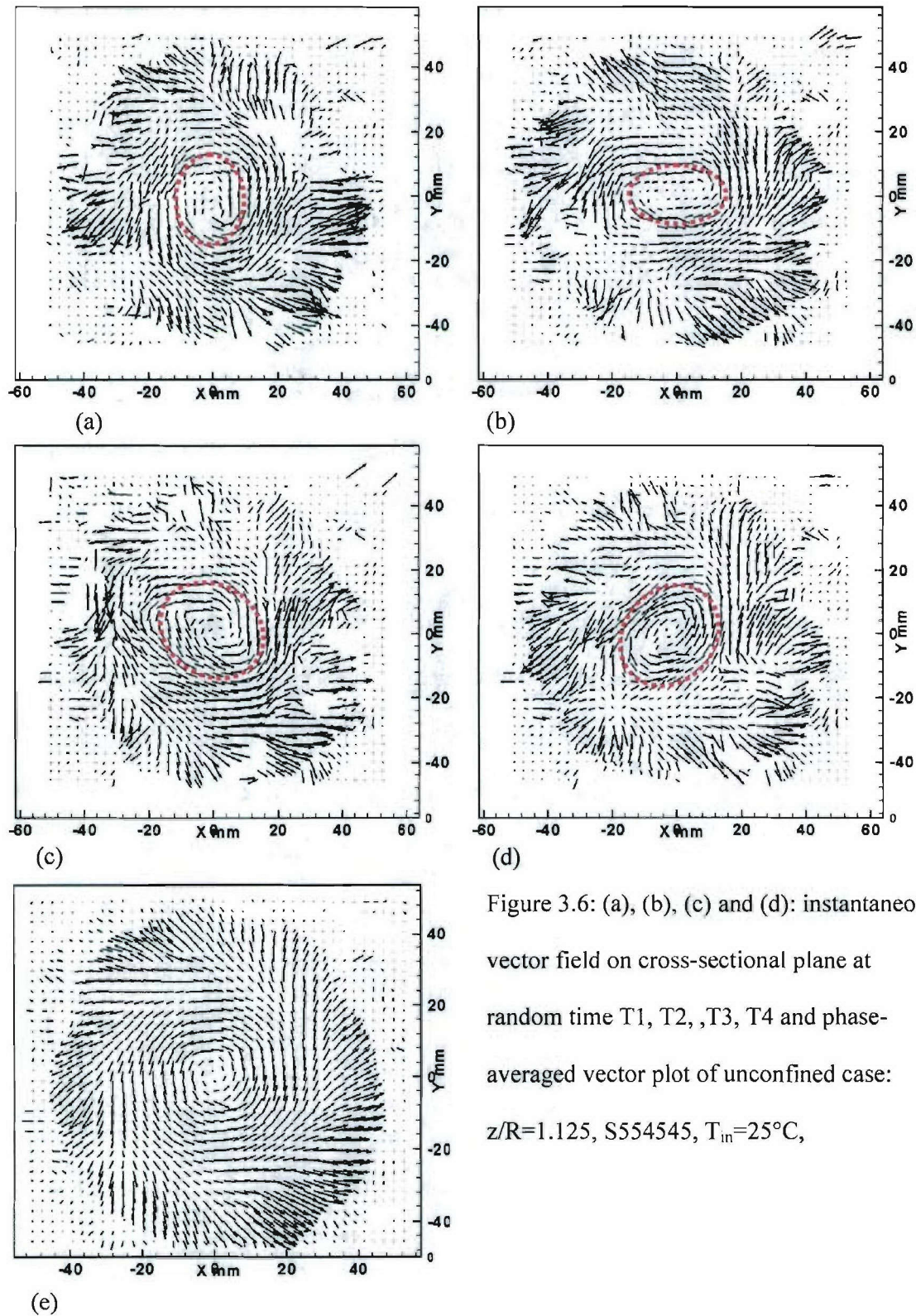
Figure 3.6: (a), (b), (c) and (d): instantaneous vector field on cross-sectional plane at random time T1, T2, ,T3, T4 and phase-averaged vector plot of unconfined case: z/R=1.125, S554545, T_{in}=25°C,

Phase-averaged Flow Fields

(1): On Streamwise Plane

The airflow rate for all the isothermal flow tests was maintained at 0.033kg/s, corresponding to R_{eD}=4.4x10^4 for isothermal flow (T_3=20°C) and 3.2x10^4 for the combustion case (T_3=230°C). For L/D_c=4.5, the PVC frequency at R_{eD}=4.4x10^4 was 40 Hz with a period of 25 ms. Phase-locked images were taken at phases 0°, 58°, 116°, 174°, 232°, 290°, and 348°. For each angle a total of 36 images were captured to maximize the average image quality. In order to avoid the interference due to the strong reflection caused by the laser sheet passing through the burner wall, especially from the incoming side (left side of the test setup), the field of view was made slightly larger on the right side. Therefore, velocity field are shown more on the right side than on the left side.

The 3-D vector plots and contours of the axial velocity component on streamwise plane are shown in Fig. 3.7. For 3-D vector plot, X= 0 is at the chamber centerline and Y indicates the axial direction. For contours, r/R and z/R are used for radial and axial coordinates. The PVC is usually located at the region enclosed by the zero velocity line, i.e. inside the central recirculation zone. A large vortex was formed Along the inner edge of the emanating jets (clearer on the right side) at Y=-40 mm and this vortical structure extended downstream to gradually connect with another smaller vortex at about y=0 mm (dash line circle zone in Fig. 3.7 3-D vector) as the phase angle increased from 0° to 232°. Axial velocity contours show a bubble shape CRZ. The strong reversed flow (the deeper blue on the central region close to the TARS exit) first tilted to the left (0°) and then reduced its reversed flow magnitude on the left side and became more axisymmetric (116°). At 232° the reversed flow strength gains its strength back on

the left side. Although the overall shape of CRZ seems stable versus phases, its core takes the motion in the circumferential direction.

0°

116°

232°

3-D vector   Axial Velocity
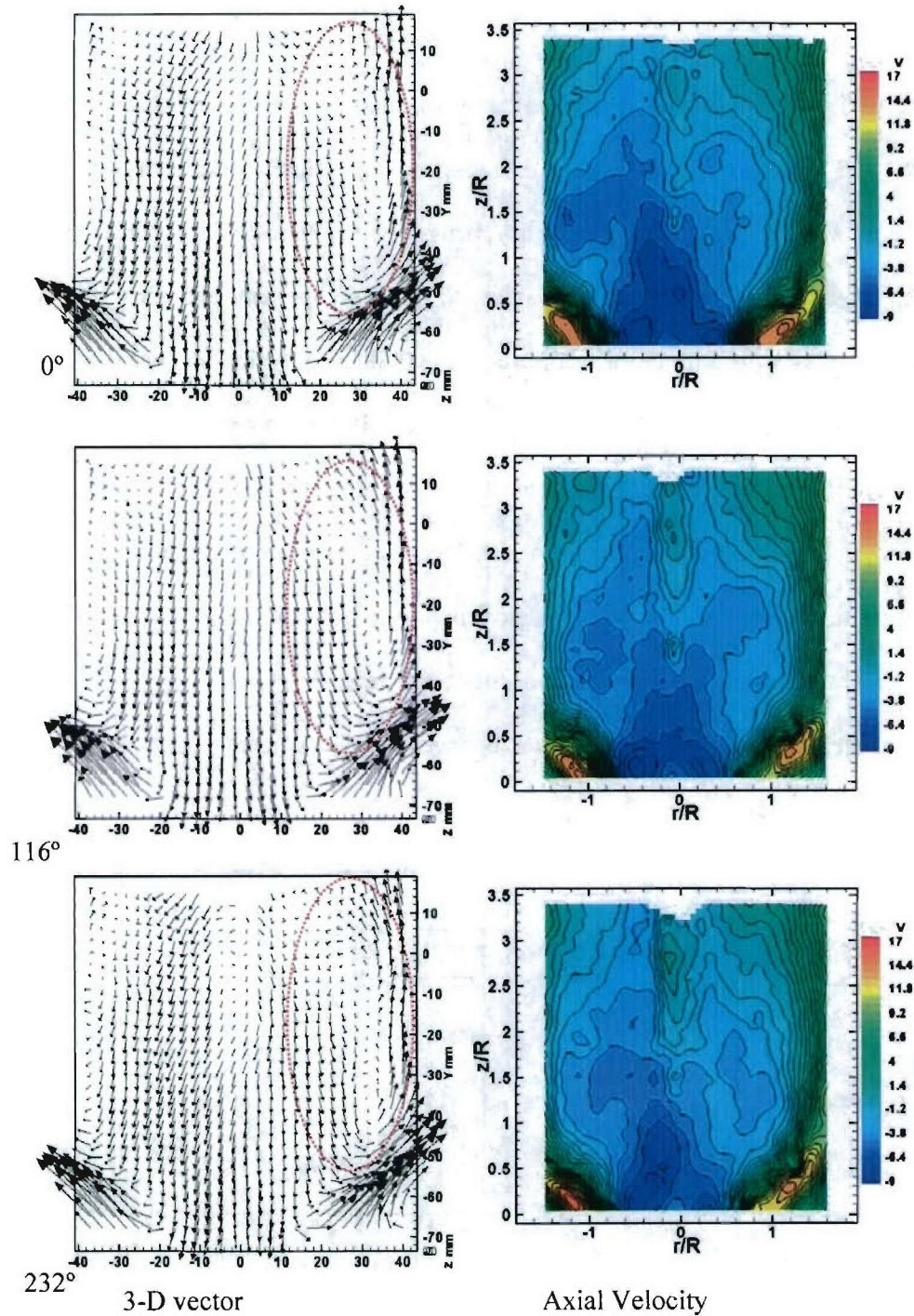
Figure 3.7: Flow Field in the streamwise plane: (a) 3-D vector plot, X=0 is centerline of the chamber; Y=-70 is flush with the TARS exit; (b) axial velocity contours, r is radial direction and z is the axial direction, coordinates normalized with R. T_3=20°C; R_{eD}=5x10^4.

The influence of PVC to flow fields was further quantified by profiles of three velocity components at z/R=0.2 and 2 in Figures 3.8 and 3.9, respectively. Close to the combustor inlet (z/R=0.2), peak axial velocity magnitude gradually changed with phase angle whereas taking different evolution directions on the left and right sides. All three components are fairly clustered together with phase angles within the vortex core region (±0.5R). Outside this core, the mean and RMS of three velocity components become oscillating for different phase angles, indicating this region was most affected by PVC. Further downstream at z/R=2, the vortex core region gets smaller and the reversed flow starts to recover back to incoming flowing direction at this point (see Fig. 3.7 axial velocity contour). The central region manifests large differences in mean axial, tangential and RMS tangential velocity around the centerline. Interestingly, the standard deviation of radial velocity is averaged 3~4m/s between ±1.5R whereas the mean radial component is fairly close to zero.
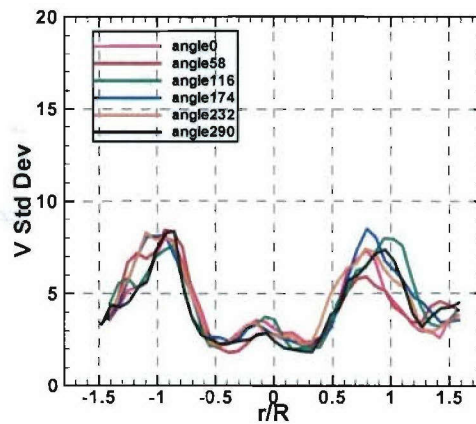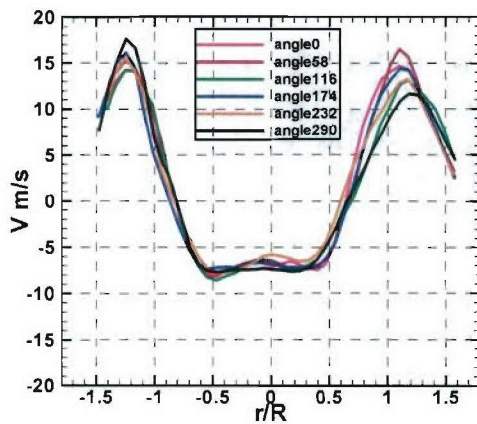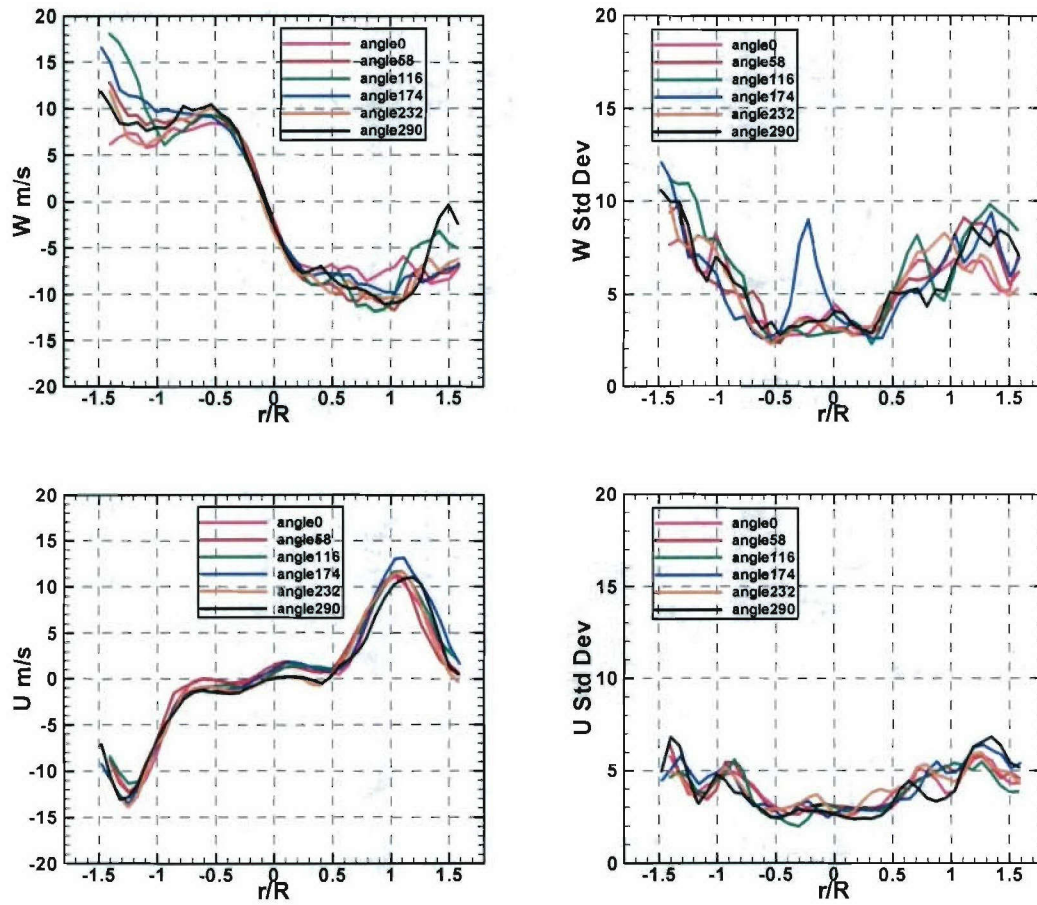
Figure 3.8: Profiles of mean and RMS velocity components at different phase angles: axial (V), tangential (W) and radial (U) at z/R=0.2 of contours in Fig. 4.7: T_3=20°C; R_{eD}=4.4x10^4.

31
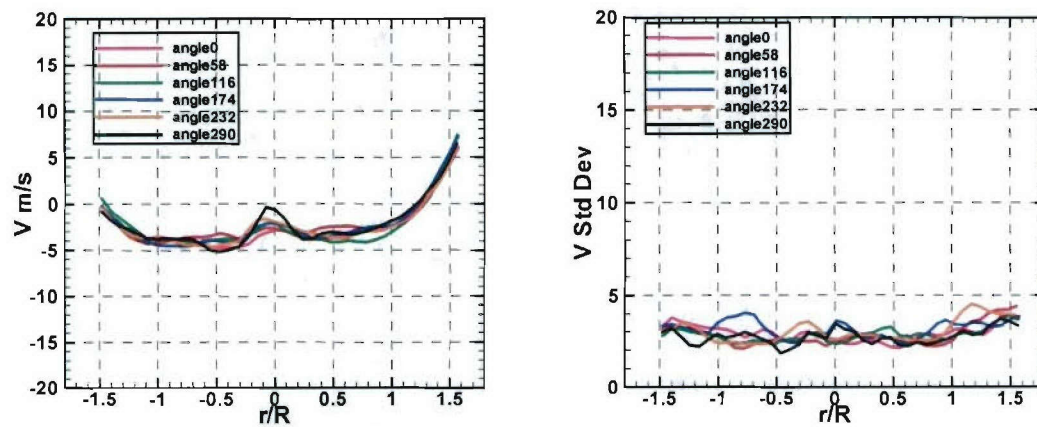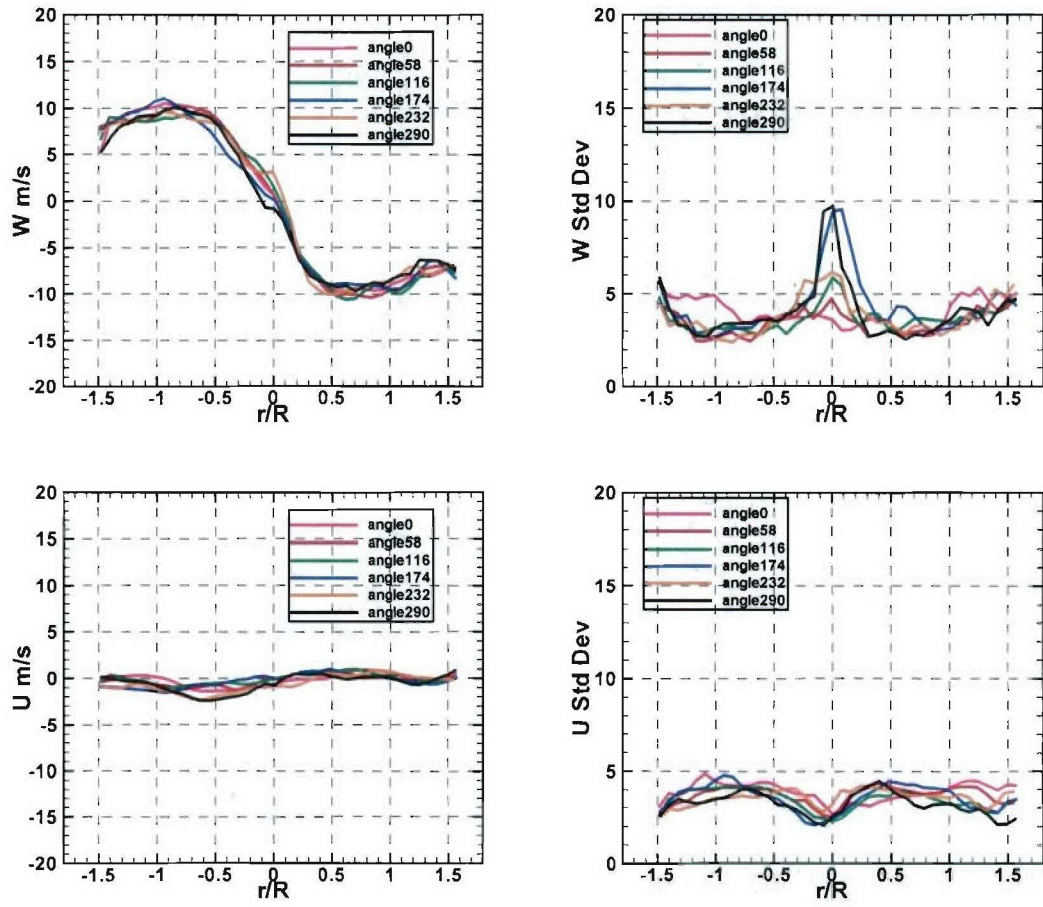
Figure 3.9: Profiles of mean and RMS velocity components at different phase angles: axial (V), tangential (W) and radial (U) at z/R=0.2 for contours in Fig. 4. 7: T_3=20°C; R_{eD}=5x10^4

(2) On Cross-sectional Plane

PVC motion in the circumferential direction can be further clarified by measurement in the cross-sectional plane. 3-D vector plots in the crosswise planes at three axial locations: z/R= 0.25, 1.125 and 2 are shown in Fig. 3.10. Very close to the nozzle exit (z/R=0.25), the flow had very strong radial and tangential movement concentrated on a 1.6R (40 mm) radius circle. With the flow traveling downstream, a solid body rotation zone appeared at the center and its diameter grew with z/R. This core had a radius of 1R (25 mm) at z/R=1.125 and increased to 1.6R (40 mm) at z/R=2. No apparent differences can be discerned on the vector plots for different phase angles. The PVC, which is supposed to be a small vortex or several vortices around the center core, does not show up in these vector plots either. This may relate to the smooth effect of phase-locked measurement.

More information about PVC can be found from the tangential velocity and vorticity contours (Fig. 3.11) for phase angles between 0° to 290° on the plane z/R=1.125. The confining tube complicated the flow region near the wall, forming stronger tangential velocity gradients as shown by the clustered contour lines. Very close to the centerline, there is a compact circular core of high tangential velocity gradients with a radius less than 0.4R . Vorticity contour also confirmed that this core had very intense vorticity and opposite sign from the vorticity near the wall. There are two strong tangential velocity spots surrounding this core and forming a larger core with a radius of 1R that was shown as a solid body rotation region in the vector plots. These two spots changed with the phase angle: the area of the left side spot increased from 0° to 116°, decreased from 116° to 232° and increased again after that, whereas the right side exhibited the opposite evolution. Between this region and the wall, several high tangential velocity spots with

strong negative vorticity moved circumferentially with the phase angle. It may conjecture that the PVC mostly impacts the region outside the vortex core.

The results from streamwise and cross-sectional planes demonstrate that motion of PVC in helical mode, affecting the mean axial and tangential velocity magnitude and their rms components in a fairly big region outside the central vortex core.

z/R=0.25

z/R=1.125
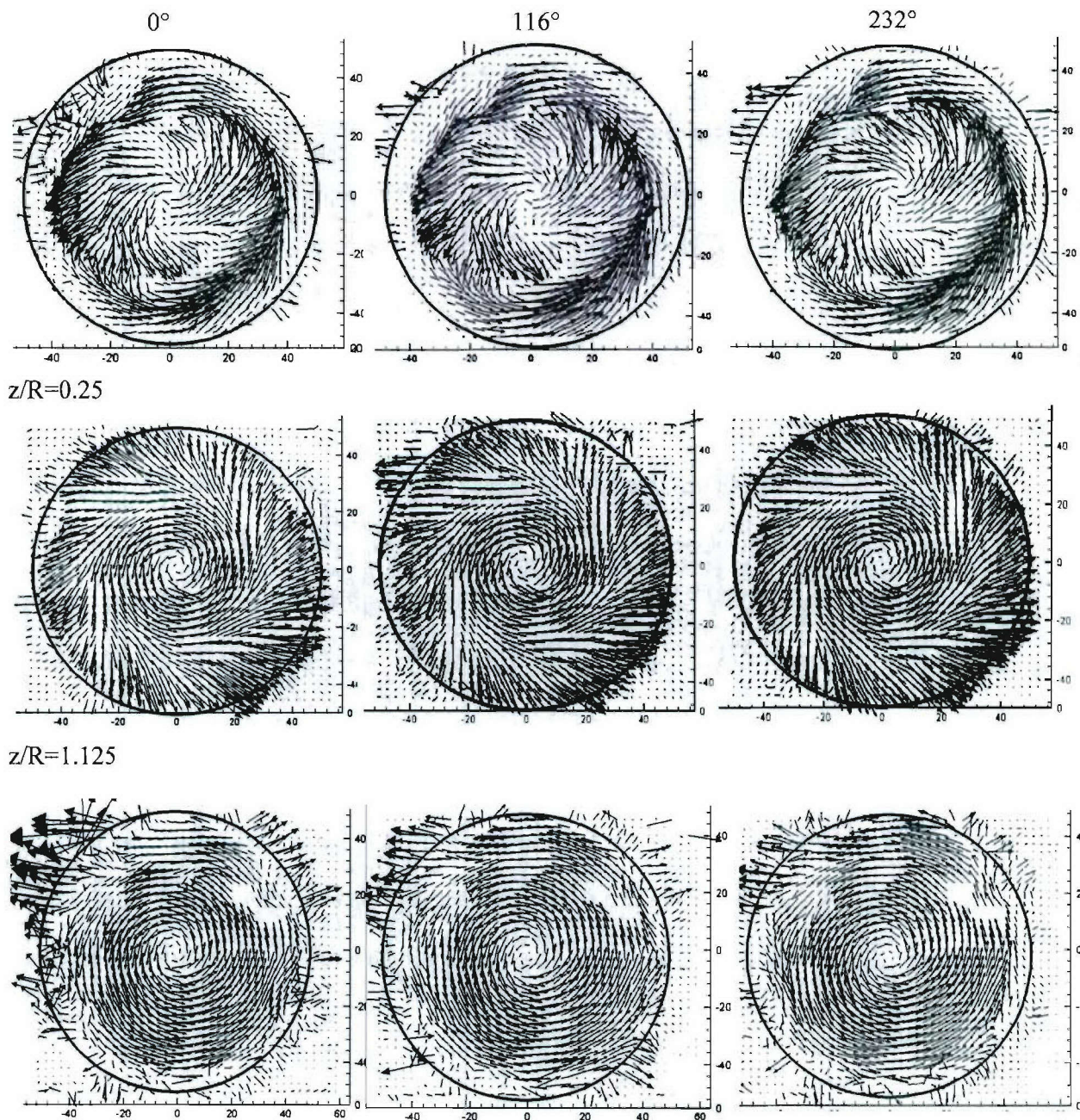
Figure 3.10: 3-D vector plots at cross-sectional planes z/R=0.25, 1.125 and 2 for different phase angles. The black circle shows the 50 mm diameter combustor wall. T_3=20°C; R_{eD}=4.4x10^4.

Tangential Velocity   Vorticity
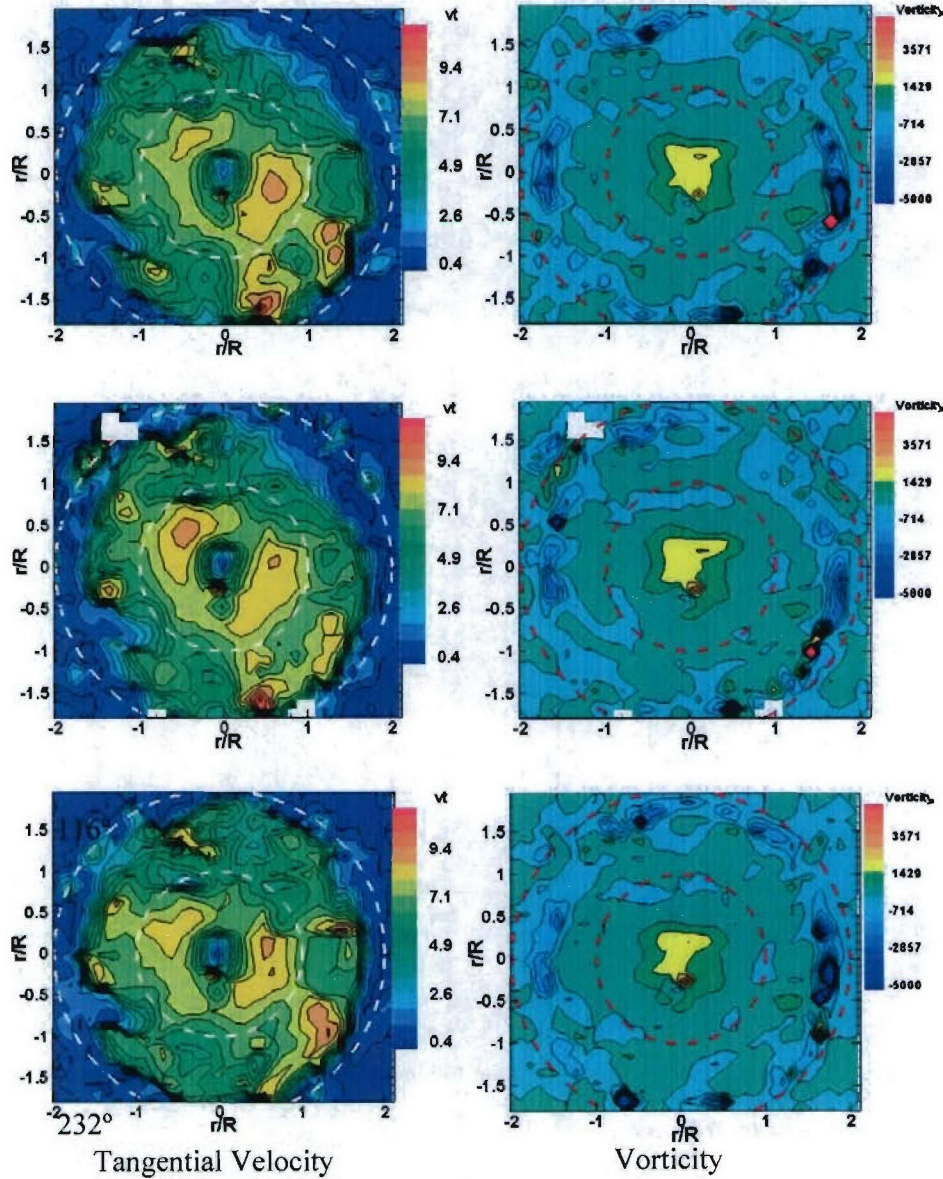
Figure 3.11: Contours of tangential velocity and vorticity on crosswise plane z/R=1.125 at different phase angles. The dotted circle shows the 50 mm diameter tube wall and 25mm vortex core. T_3=20°C; R_{eD}=5x10^4; cold flow.

3.2 Large Vortex Shedding from Dump Plane (LVSD)

In order to find out the preferred mode of swirling flow in this burner, two loudspeakers of total 150 Watts were used to acoustically force the flow field at ambient condition with R_{eD}=4.4x10^4. The forcing frequency ranged from 110 to 440 Hz. FFT spectra analysis showed the dominant frequency and its magnitude at two driving frequencies (Fig. 3.12a for 340 and 360 Hz as examples). The peak magnitude versus the driving frequencies is shown in Fig. 3.12b. 180Hz and 360Hz are the two most amplified frequencies of this system with a Strouhal number of 0.62 and 1.24, respectively, based on the average exit jet velocity and TARS exit diameter. The two frequencies were interpreted as the preferred modes of the vortex shedding from the dump plane. Because 360 Hz caused stronger system response it was chosen as the driving frequency for phase-locked PIV measurement of the LVSD.

(a)	(b)
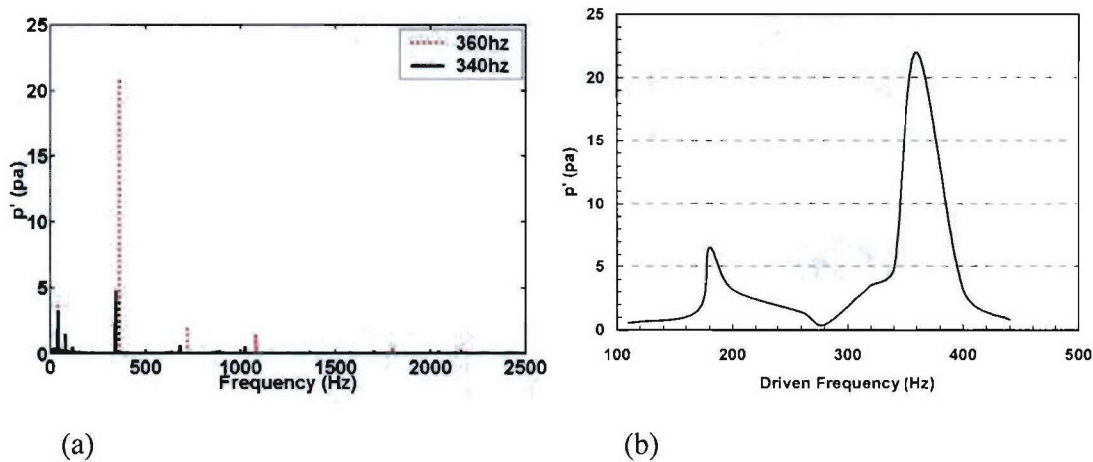
Figure 4.12: Acoustic response of the combustion chamber system to loudspeakers driven signals: (a) spectra for 340 and 360 Hz; (b) peaks of dominant frequency.

Velocity field acoustically forced at 360 Hz was measured with phase-locked PIV in the streamwise plane. The trigger signal was generated by a time-delay board with a sinusoidal signal from the function generator that was also used to drive the speakers. The vortex sheds

from the dump plane at 0°, starts merging into the jet at phase 104°, becomes almost totally buried in the jet at 208°, and resumes at 312° (Fig. 3.13: 3-D vectors). Along with the vortex movement, the jet increases its vorticity strength when the vortex merges into it (Fig. 3.13: vorticity). Concurrently, the strong vorticity spot of the vortex moved towards the wall at the same direction of the jet movement as is labeled with arrow in Fig.3.13. The simultaneous movement of the vortex and the swirling jet indicates the periodic movement is responsible for the periodic shedding of the vortices. The bond of the jet and the corner vortex may lie in the "kidney" vorticity structure that is formed at the interface. This structure may be one possible carrier for transfer energy between the jet and vortices and thus linking them together. Fig. 3.13 illustrates that the vortex shedding closely relates to the jet dynamics at the system resonance frequency.

Bridged by the swirling jet, the central flow field that is mainly dominated by the PVC may interconnect with the corner flow regions where the vortices shedding from the dump plane are the dominant structures. Large vortices are formed on both sides of the swirling jet, with the inner vortices traveling downstream as shown in Fig. 3.7a whereas the outer vortices circulating around the corner. All these large vortices will take part in the combustion process and contribute to thermo-acoustic combustion instability when excited.

3-D vector   Vorticity

0°

104°

208°

312°
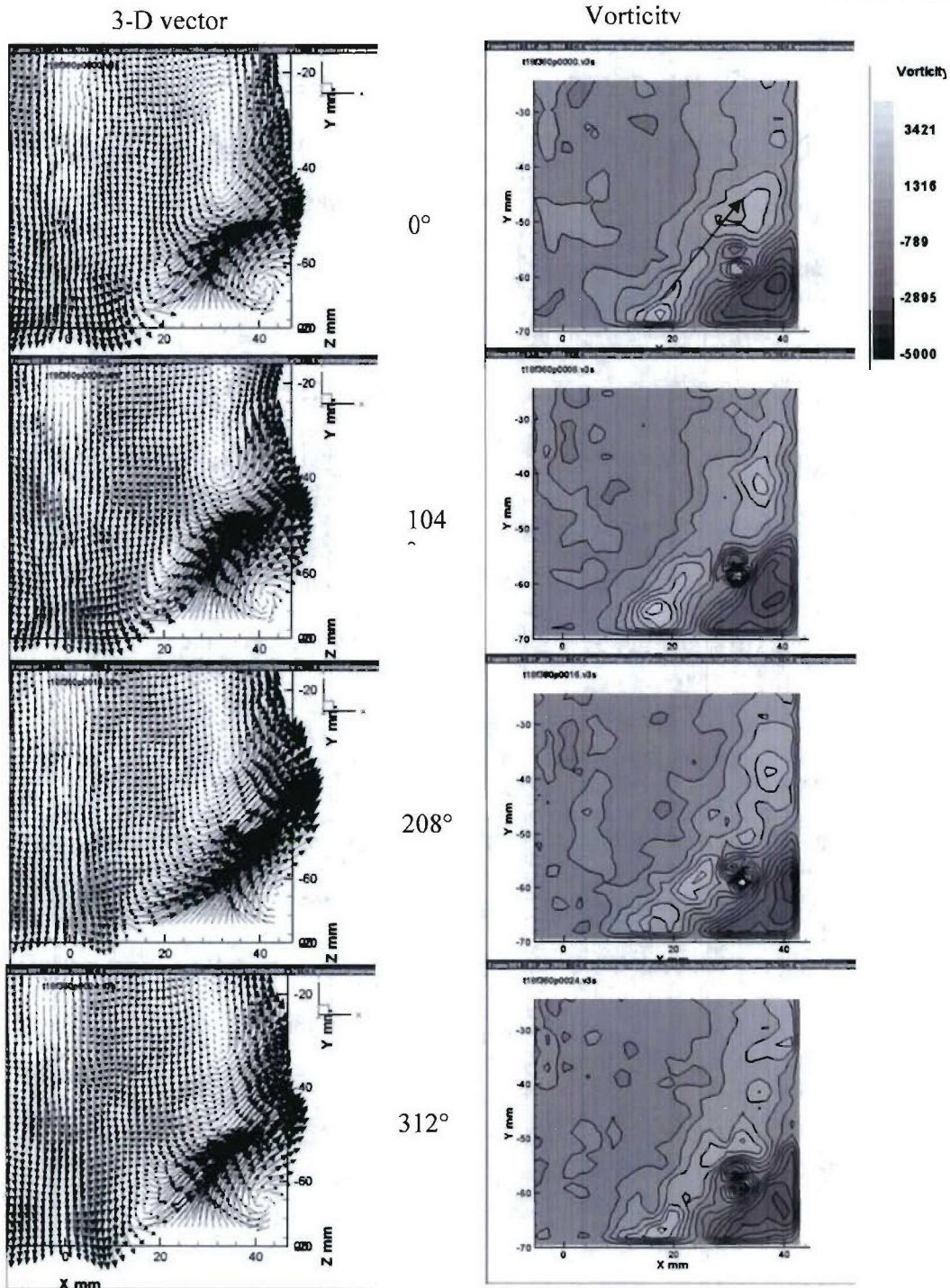
Figure 3.13: 3-D vector plots and vorticity contours of the large vortex shedding at the dump plane. Forcing at 360 Hz, T_3=20°C; R_{cD}=5x10^4; cold flow.

38

3.3 Effects of Inlet Air Temperature on Swirling Flow Field

Inlet air temperature is a major factor for gas turbine combustion performance therefore knowledge of its effects on swirling flow field will be helpful for combustor design and combustion performance improvement. For the same air mass flow rate, high temperature will increase the bulk velocity and viscosity, significantly changing the inlet Reynolds number and potentially affecting the swirling flow dynamics.

Contours of V_z, V_θ and total RMS velocity at different inlet air temperature T_3 are shown in Figure 3.14. The magnitude of the reversed flow velocity increases about two times when T_3 increases from 23°C to 300°C (see contour of V_z=-10m/s in Fig. 3.14) and so is the axial velocity gradient at the border of the CRZ. The magnitude of tangential velocity increases from 9 m/s to about 17 m/s when T_3 increases from 25 to 300°C. The total turbulence, represented by RMS velocity, increases at least 1.5 times at the jet region and CRZ.
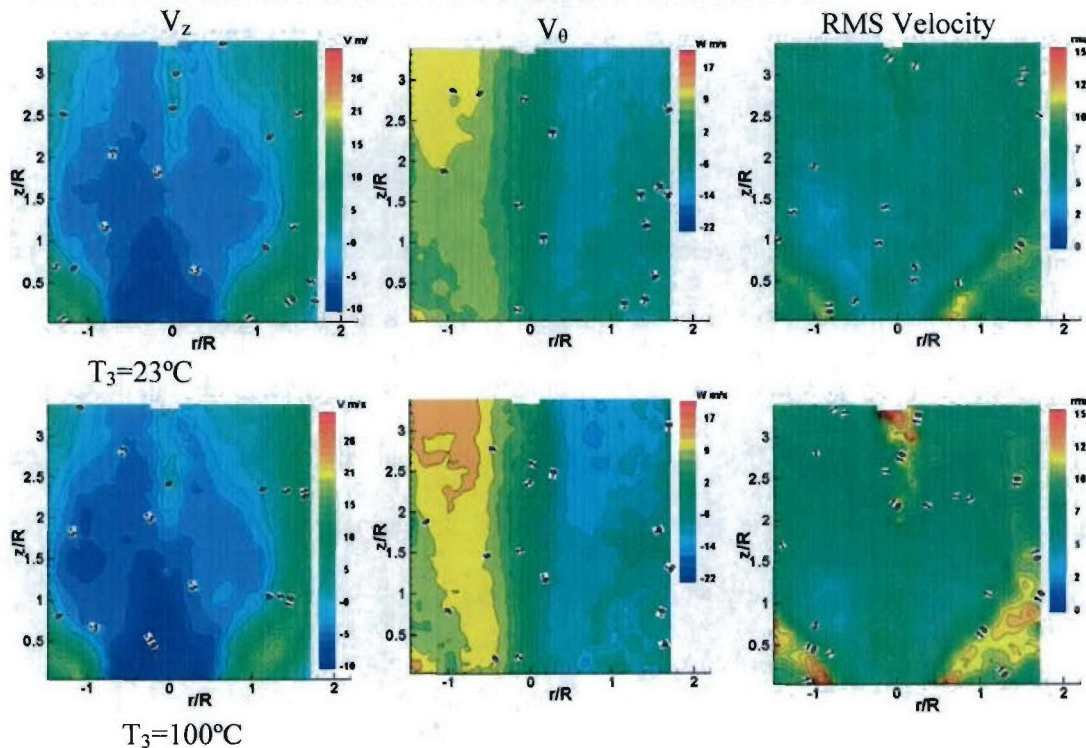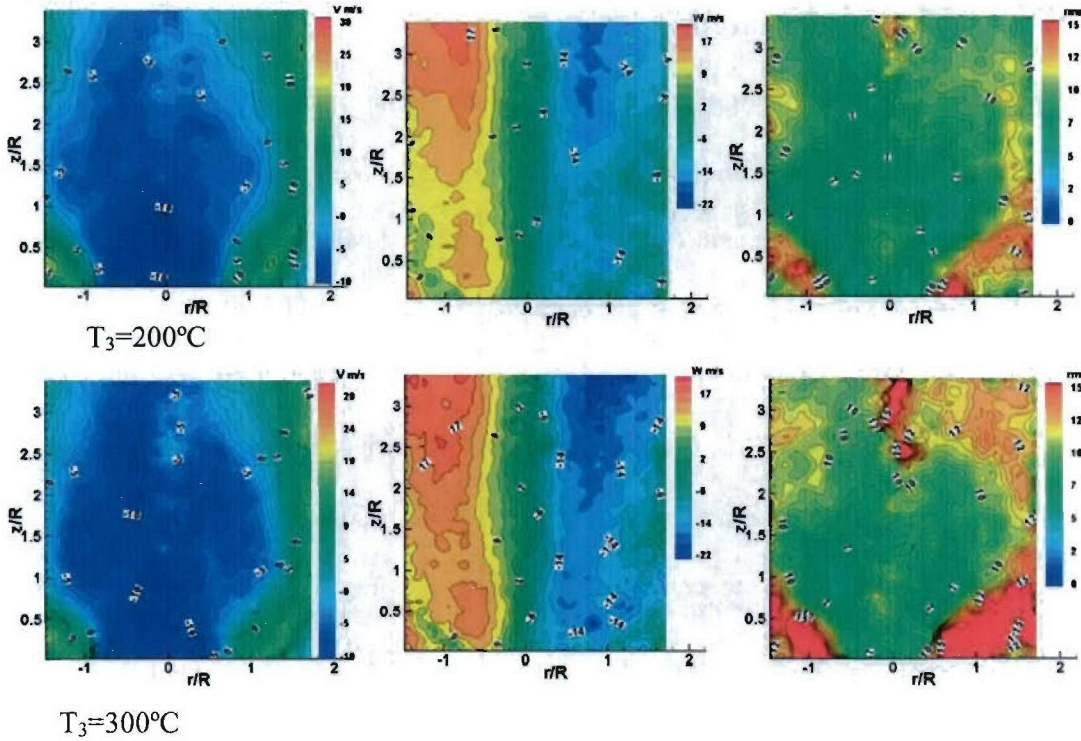
Figure 3.14: Contours of axial, tangential velocity components and total RMS velocity fluctuation at T_3=23, 100, 200, 300°C: m_a=0.032kg/s.

These observations are confirmed by the velocity profiles extracted at z/R=0.5 (Fig. 3.15). Surprisingly, the positive peak axial velocity only increases 3m/s, about 30%, when the volume flow rate increases about two times because the mass flow rates are same but density drops to half with T_3 from 23°C up to 300°C. The total turbulence, however, substantially increases with higher inlet air temperature: the RMS axial, tangential and radial velocity components increase more than 50%. In addition to these velocity components, the components of Reynolds stress are also significantly enhanced especially when T_3 gets to 300°C.

We can also evaluate the effect of inlet air temperatures on turbulence intensity by normalizing the total turbulence velocity with the average TARS exit velocity. Because the tests

are kept at the same mass flow rates, the average TARS exit velocity can be calculated based on the density, i.e. 13, 16, 21, 25m/s for T_3 =23~ 300°C. Figure 3.16 depicts the profiles of normalized turbulence intensity along radial direction. Different from the observation for absolute turbulence velocity in Fig. 3.15, the normalized curve shows high relative turbulence intensity for lower inlet air temperature. It is also noticed that inlet temperature will mostly affect the shear layer regions and the core of the CRZ, as is supported by the large variation of axial and tangential velocity in these regions in Fig. 3.15.
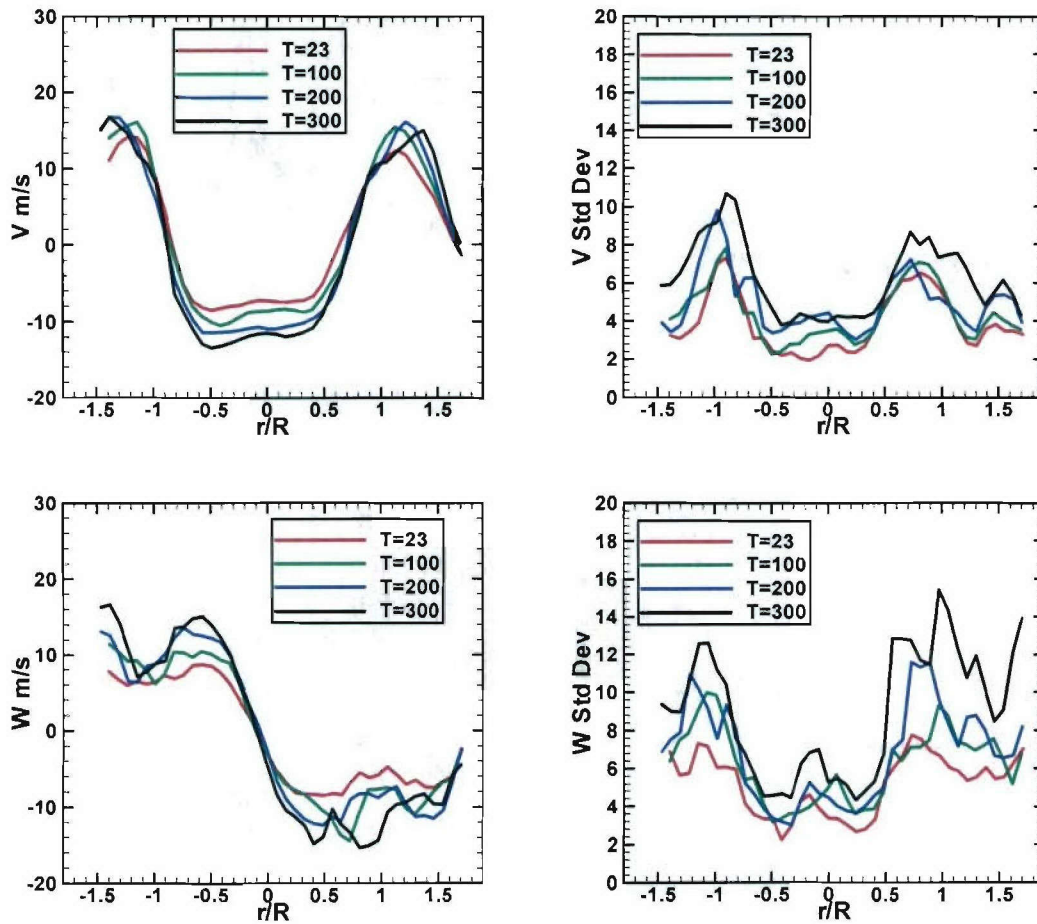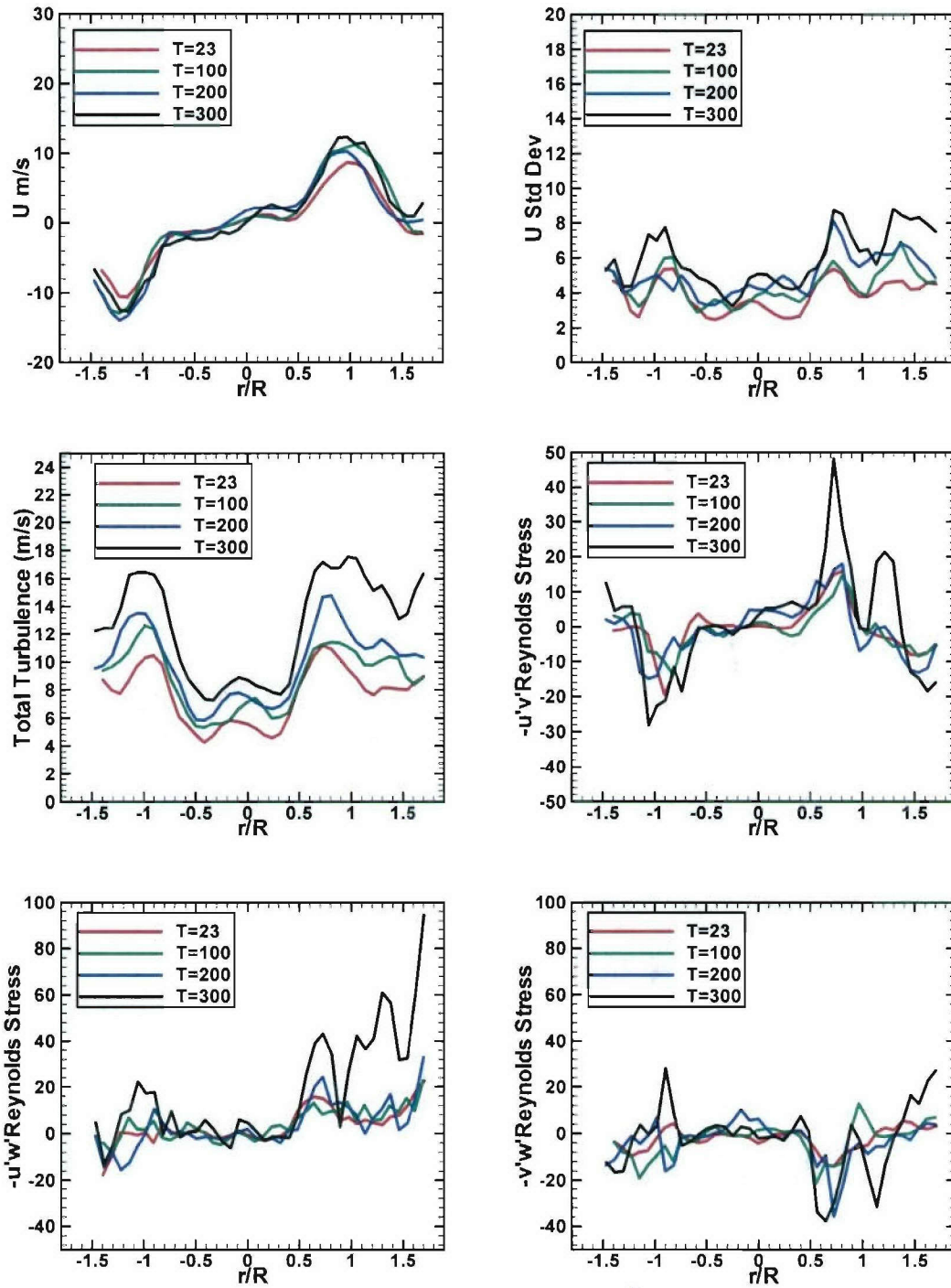
Figure 3.15: Profiles of mean and standard deviation of axial (V), tangential (W) and radial (U) components and total turbulence, Reynolds stress at z/R=0.5 for T_3=23~300°C, m_a=0.033kg/s.

Therefore, the most significant effect of high inlet temperatures on flow field is on the turbulent velocity fluctuation and the Reynolds stress. These effects can impact fuel/air mixing, the combustion process and its dynamics, and consequently emissions. As will be observed in combustion tests, higher inlet temperature increases NO_x emission. Enhanced turbulence intensity and Reynolds stress from higher T_3 may be the reason for the extra NO_x formation in addition to the increment of the flame temperature.

4.4 Effects of combustion on swirling flow

Swirling flow fields will be different for combustion cases than that of isothermal ones because the heat release from combustion changes the temperature, density and therefore velocity fields. The comparison of the axial, tangential and radial velocity components for combustion and isothermal flows is shown in Fig. 3.16. The recirculation zones are all in bubble shape but the size and location are quite different. For stable combustion, CRZ is lifted and the neck becomes significantly smaller, only ±0.2R, compared with ±0.7R of the isothermal case. When unstable combustion occurs, the CRZ gets compact and intensified.
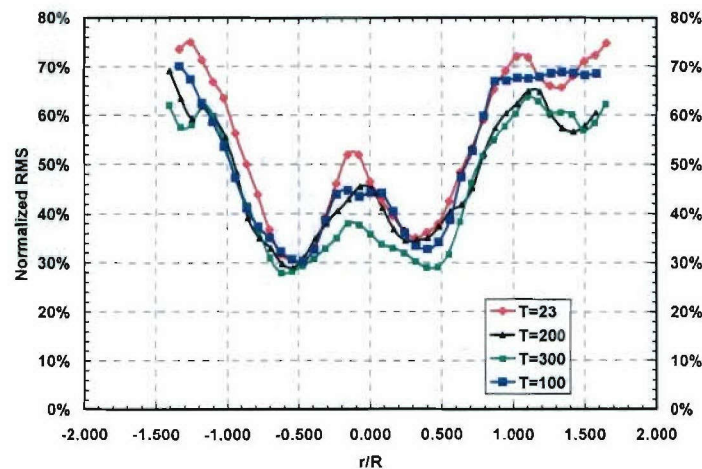
Figure 4.16: Normalized turbulence velocity versus radial dimension (r/R) for T_3= 23~300°C at m_a=0.032kg/s.

The unstable combustion also cause uneven distribution of velocity components on the left and right sides, which is shown in Chapter VI to be related with the combustion instability. Stable combustion has comparable tangential velocity compared with the isothermal case whereas unstable combustion significantly enhances tangential component at certain locations. Combustion has dramatic effect on the radial velocity: it enhances radial velocity to 20m/s for stable combustion and 30m/s for unstable case compared with 10m/s of isothermal case. The strong radical direction movement of combustion swirling flow will help transport fuel/air mixture towards the wall. The total turbulence in the vicinity of the nozzle exit does not impacted too much by the combustion as long as it is stable. Further downstream, however, combustion increases the turbulence fluctuation and unstable combustion increases the RMS turbulence about twice. Velocity profiles at $z/R=0.2$ (Fig. 3. 17) highlights the effects on three mean velocity components from unstable combustion: the significance of combustion on central axial velocity, tangential and radial velocities outside the $r/R=\pm0.5$ core region, and enhancement of the RMS. This figure also illustrates the similarity in tangential velocity and RMS turbulence between the isothermal and combustion cases.
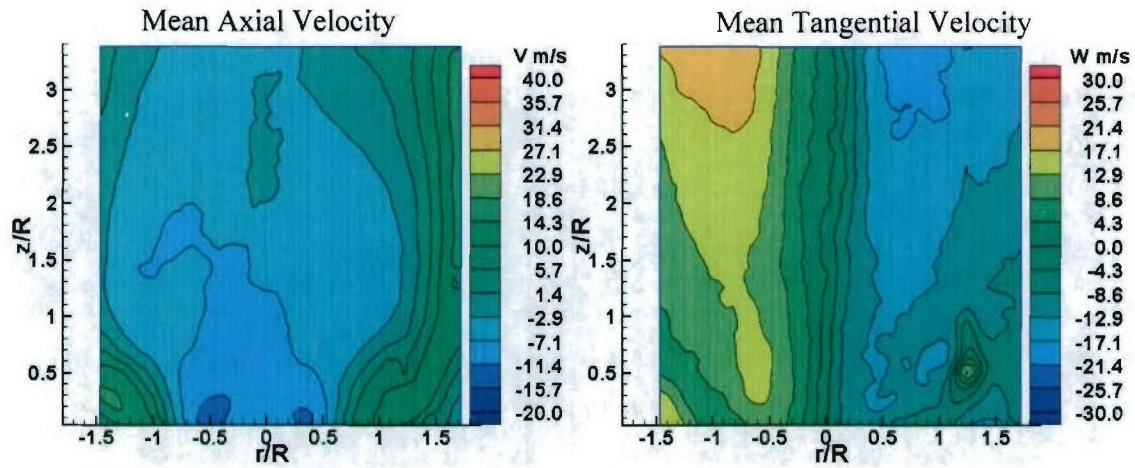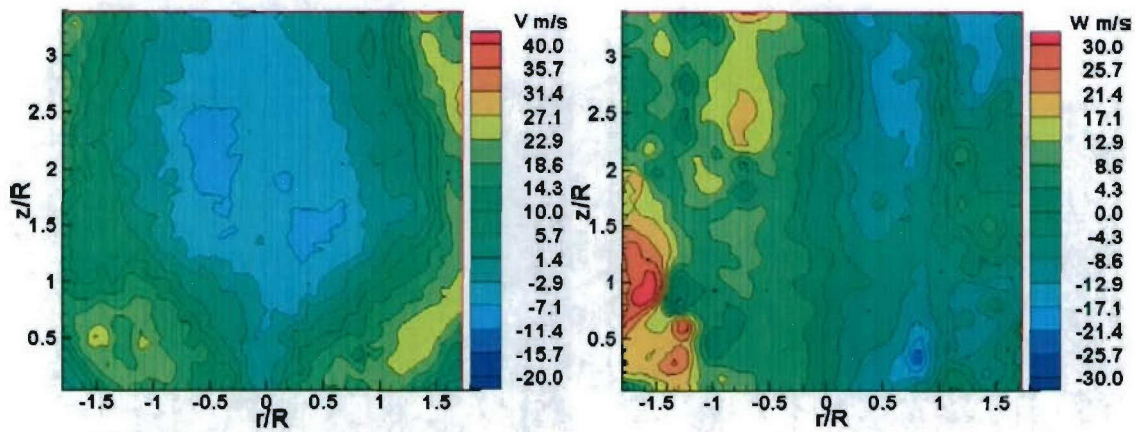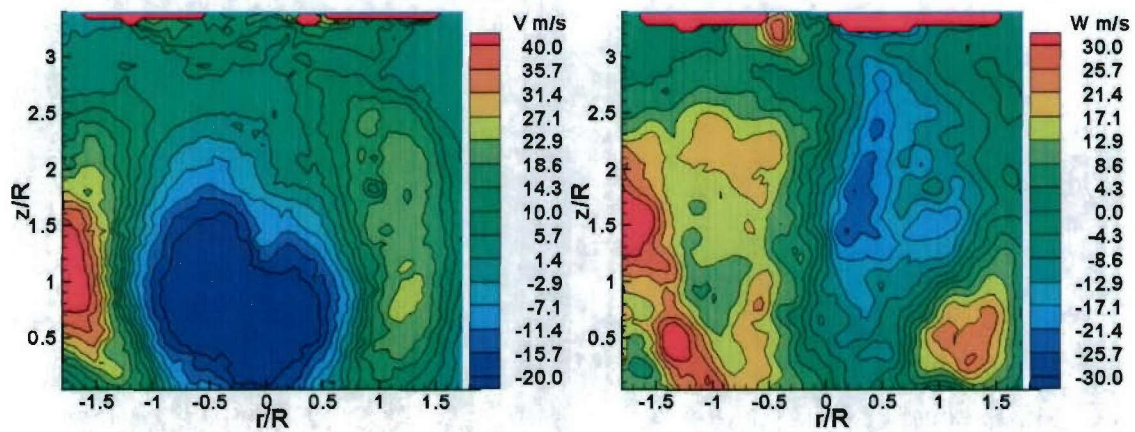
Mean Axial Velocity — Mean Tangential Velocity

Isothermal Flow: T_3=230°C

Stable Combustion: T_3=230°C

Unstable Combustion: T_3=230°C

Mean Radial Velocity / Total Turbulence Velocity
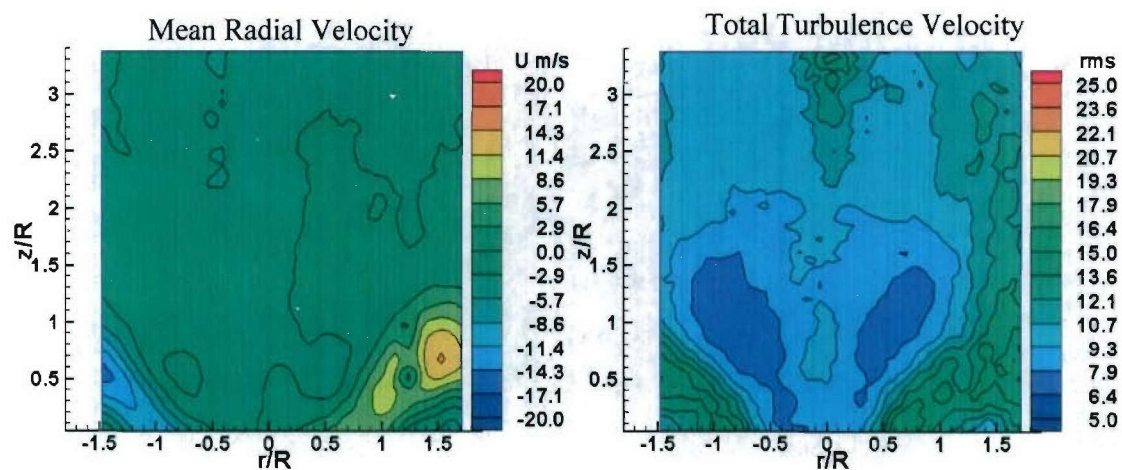
Isothermal Flow: T_3=230°C
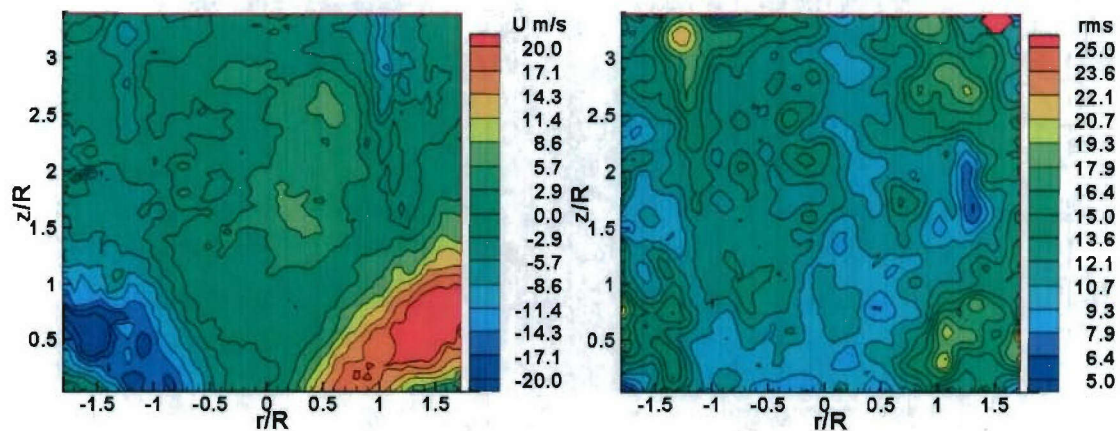
Stable Combustion: T_3=230°C
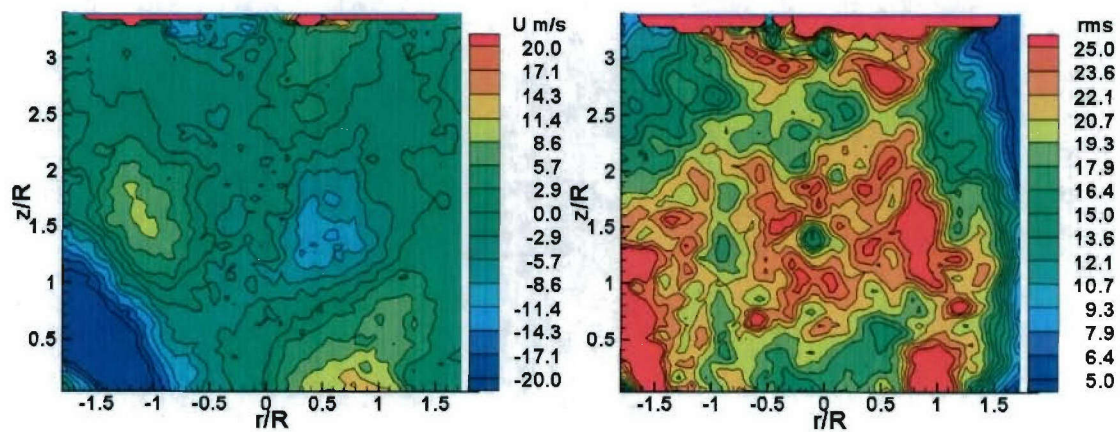
Unstable Combustion: T_3=230°C
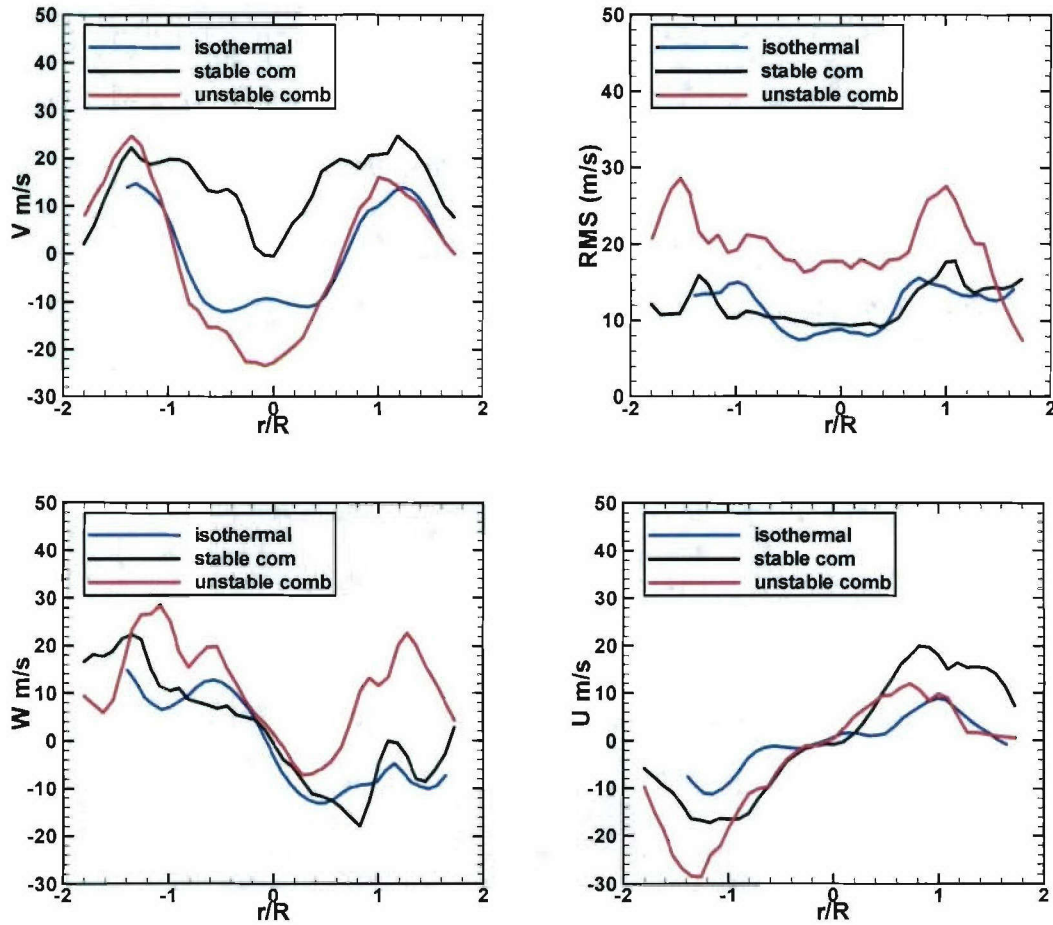
Figure 3.17: Contours of axial, tangential, radial velocity components, total RMS velocity fluctuation, and velocity profiles at z/R=0.2 for swirling flow fields at isothermal, stable combustion and unstable combustion cases. T_3=230°C, m_a=0.032kg/s.

Summary

Through phase-locked PIV measurements of the flow field on the streamwise and cross-sectional planes, the periodic behavior of the Precessing Vortex Core in swirling flow was demonstrated. The characteristic frequency parameter fD^3/Q of the PVC was constant for a fixed Swirl Number but increased linearly with the inlet air temperature. Viscosity effects should be taken into account when the inlet air temperature gets high because it increases the frequency

parameter for shorter tubes more than longer ones when viscosity gets high. The PVC is responsible for a periodic evolution of the magnitude of the axial and tangential velocity components and the core of the recirculation zone. Vector plots at three crosswise planes illustrated that the grow-up of central solid-body rotating flow region as flow traveling downstream.

Vortex shedding from the dump plane was phase-locked with the acoustic driving signal at the system preferred mode. The vortices were located at the outer edge of the emanating jet and periodically formed and merged with the jet at the driving frequency. The dynamic behavior of this vortex closely related to the periodic movement of the jet stream. A "kidney" shaped flow structure along the interface of jets and the vortices may be one possible carrier transferring energy between these two flow regions.

The inlet air temperature significantly enhances the magnitude of reversed velocity in CRZ, turbulence velocity fluctuation, and Reynolds Stress. These effects will impact fuel/air mixing, combustion dynamics and emissions. When combustion occurs, the turbulence intensity will increase but less dramatic when the combustion is stable. The central recirculation zone becomes smaller and lifted for the combustion case but the bubble shape still keeps. Radial velocity, however, increases significantly because of combustion, indicating the flow expands quicker for combustion than for isothermal case. The similarity between flow fields between isothermal and combustion cases states that the flow fields measurement from isothermal flow could be referred for combustion cases if the enhancement in turbulence velocity fluctuation and reverse flow strength are accounted.

4 COMBUSTION DYNAMICS AND CONTROL

Combustion dynamics during unstable combustion and lean blow off process are discussed in this section, as well as the correlation between these dynamic phenomena and emissions under the effects of geometry factors, inlet temperature and air-assist.

Combustion instability occurs when heat release and pressure oscillation couple with each other. As reviewed in Chapter I, this self-excited combustion instability can be either vortex driven or caused by fluctuation of fuel supply, or some other mechanism that may introduce heat release or pressure oscillation. Combustion instability in swirling flow can take place in different modes, axisymmetric longitudinal mode or helical asymmetric mode, depending on the specific combustion geometry and operating conditions. The circumferentially installed OH*/CH* optical fibers (three channels OH* and two channels CH*), together with the one installed at the center of TARS, provides dynamic light emission signal that can be referred to heat release. The pressure signals are from upstream plenum pressure transducer and the microphone that is 0.5m away from the combustion chamber.

At the different locations, the optical fibers detect different radical signals: the center one (noted as OH*/CH*_CRZ or OH*/CH* 1) looks at the flame in the central recirculation zone whereas the other three (noted as OH*/CH*_2, OH*/CH*_3, OH*_4) watching the flame holding at the shear layer. These signals are also affected by fuel property, flow parameters and combustor geometry factors. The intensified CCD camera with 310nm filter images the whole flame zone and provides overall information of OH* chemiluminescence when fuel equivalence ratio is gradually reduced. The integration of all pixel values in one image is noted as Total OH*.

One example of the RMS signals of these seven optical fibers and the integrated OH* is shown in Fig. 4.1 for propane (left column) and Jet-A fuel (right column). In the beginning, all

the optical fibers are adjusted to have the same output signal level by illuminating the fibers using a flame torch so the signal level during tests are roughly proportional to the radical emission intensity from the line sight view. For OH* of propane. the fiber 4 sees the most intense flame and gives the strongest signal level contrast to that from fiber 2. The signal from fiber 1 first reduces with decrease of Φ and then increases gradually when approaching LBO. The specialty of signal of propane from fiber 1 can also be discerned from Jet-A OH*1 and will be shown as an important pre-LBO identification feature in the later section. For CH* of propane, the three fibers show comparable signal levels and similar trends as corresponding OH* signals: the signal levels gradually decreased when the overall fuel equivalence ratio reduced (Fig. 6.1c). Similar observation can be made from OH*/CH* of Jet-A fuel, the OH* and CH* follow the same trend, indicating the close relationship between them as is suggested from chemical reaction (5.1 &2). Interestingly, the increment of RMS OH* of Jet-A near LBO manifested simultaneously from fibers 1, 3 and 4. This characteristic feature implies possible relationship between the change of radial emissions and LBO. Similar conclusions are held for Ethanol fuel also. For preventing overwhelming data presentation from all these optical fibers, OH* from fibers 1 and 4 are picked to characterize the flame dynamics of both gaseous and liquid fuel.
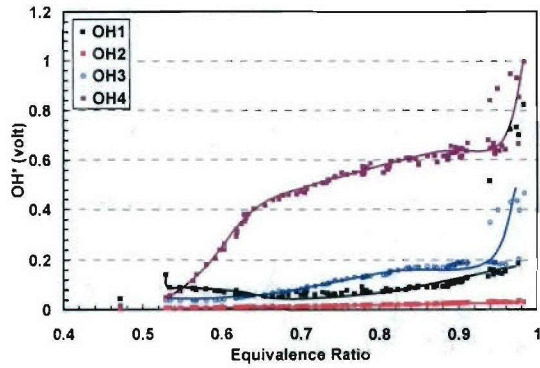
(a) RMS OH* signals: propane   Jet-A 100% pilot fuel
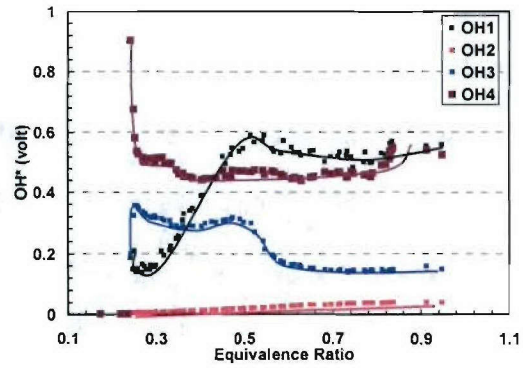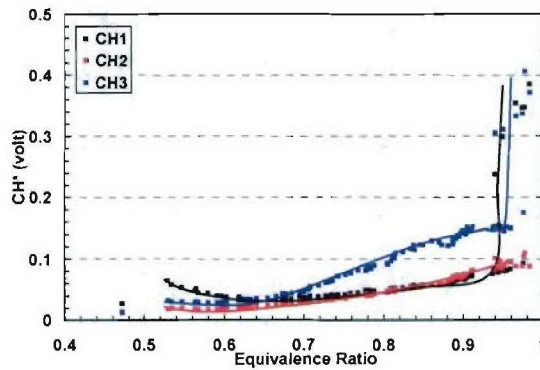
(b) RMS CH* signals: propane   Jet-A 100% pilot fuel
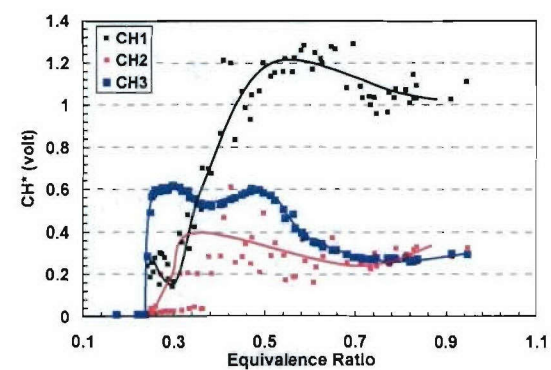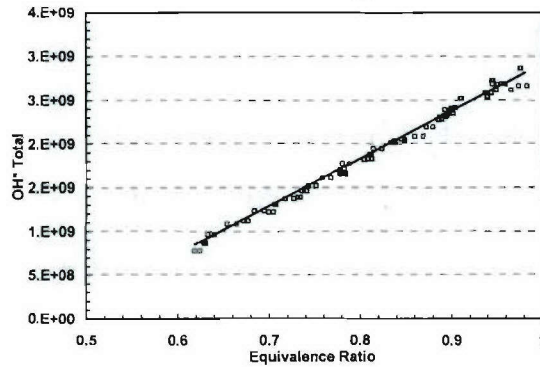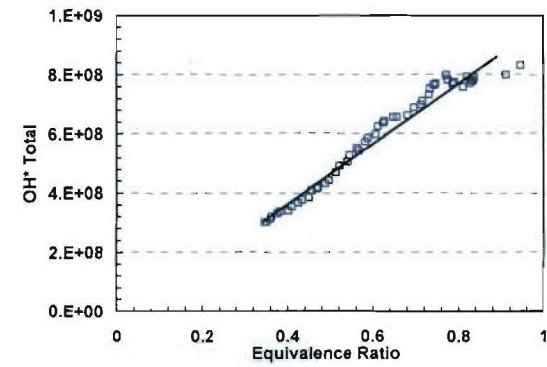
(c) OH* total: propane   Jet-A 100% pilot fuel

Figure 6.1: Dependence of (a) OH*, (b) CH* optical fiber signals and (c) OH* integrated signals on Φ at different locations for propane and Jet-A fuel: T_3=230°C, m_a=34g/s.

4.1 Effects of Flow Parameters on Combustion dynamics

4.1.1 Inlet Reynolds Number and Inlet Air Temperature

As discussed in previous chapters, inlet air flow rate and temperature affect the Reynolds number and bulk flow velocity, change the CRZ and swirling jet strength, and consequently influence the combustion dynamics and emissions.

The effects of R_{eD} and T_3 on pressure and flame oscillations of combustion with propane are shown in Fig. 4.2. The R_{eD} are calculated based on mass flow rates and T_3. At the same equivalence ratio, higher R_{eD} generally causes higher pressure oscillation (Fig. 4.2a left). This pressure oscillation, represented by RMS p', increases gradually with fuel equivalence ratio when $T_3=25°C$ but shows sudden dramatic jump when T_3 increased to 230°C. The jump locations are $\Phi=0.76$, 0.96 for $R_{eD}=34600$ and 22800, respectively, indicating earlier transition from stable combustion to unstable combustion when R_{eD} gets higher. After this equivalence ratio, the combustion encounters instability and clear acoustic tones are manifested in spectra plots in Fig. 4.3a. The dominant frequency of this combustion instability is not a function of R_{eD} because the peak frequencies are almost identical, which are 386, 385Hz for $R_{eD}=22800$ and 34600, respectively. The oscillations of flame at the CRZ increase when Φ reduces close to LBO for both Reynolds numbers at $T_3=25°C$. This phenomenon, however, is not as obvious when $T_3=230°C$ as in the lower inlet temperature (Fig. 4.2b). This indicates that when the flame is approaching LBO the oscillation of flame at the CRZ is stronger for lower inlet air temperature. At lower inlet temperature, the fuel mixing is not as good as higher inlet temperature case. The uneven distribution of lean and rich mixture spots within CRZ intensifies the variation of local chemical reaction and therefore strong oscillations in OH* radicals. When $T_3=25°C$ the flame anchored at the shear layer achieves its maximum oscillation in radical intensity at about $\Phi=0.72$

(Fig. 4.3c) but the flame within CRZ reaches its minimum. This is not coincidence because it holds for both Reynolds number and repeatable for several similar tests. We may say that the strongest flame oscillation shifts from the shear layer region to CRZ when equivalence ratio decreases. In other words, flame is more stable when strong oscillations of OH*/CH* radicals occurs in shear layer other than in CRZ. This is especially significant for lower Reynolds number. For higher inlet temperature, the maximum oscillation was not observed in the test range. Corresponding to the strong pressure oscillations, the radicals also manifest strong oscillations (Fig. 4.2b and Fig. 4.3b) at R_{eD}=22800 when Φ moves towards the rich side. The radical field within CRZ responses more strongly to pressure oscillations than the shear layer flame zone. This suggests combustion instability may closely relate to the dynamics of CRZ that will be further studied by PIV measurements.
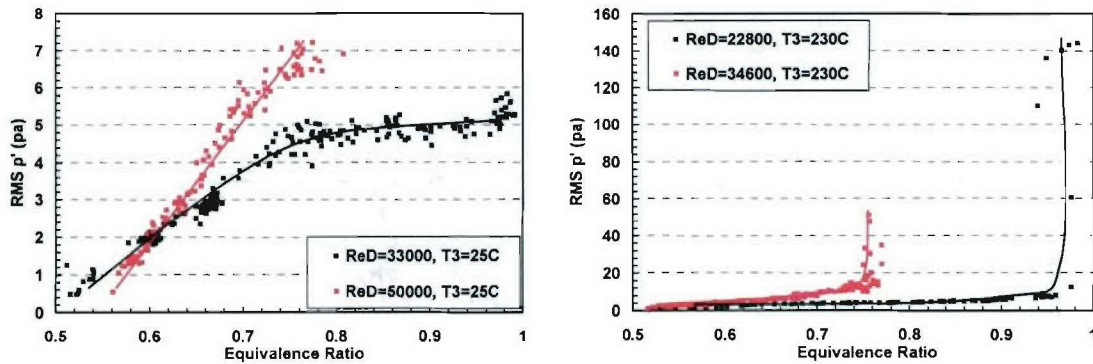
(a) RMS p'
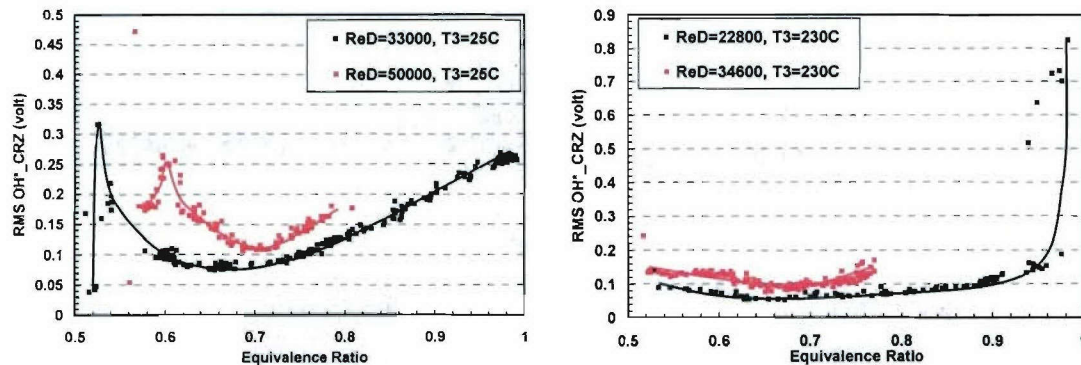
(b) RMS OH*_CRZ at central recirculation zone
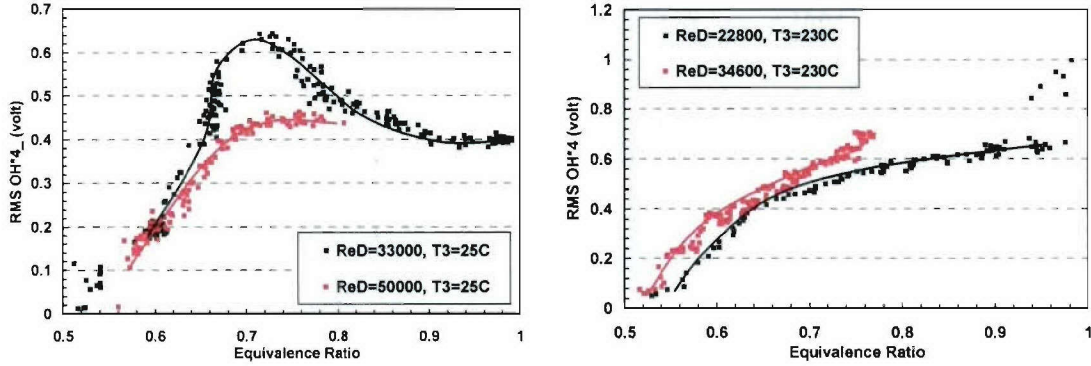
(c) RMS OH*_4 at the shear layer flame region

Figure 4.2: Comparison of RMS p', RMS OH*_CRZ, RMS OH*_4 for different R_{eD} at T_3=25°C, 230°C, propane, L_{mt} = 0, C_R=1, S5545C45.

(a) p', T_3=230°C, R_{eD}=22800;   p', T_3=230°C, R_{eD}=34600;
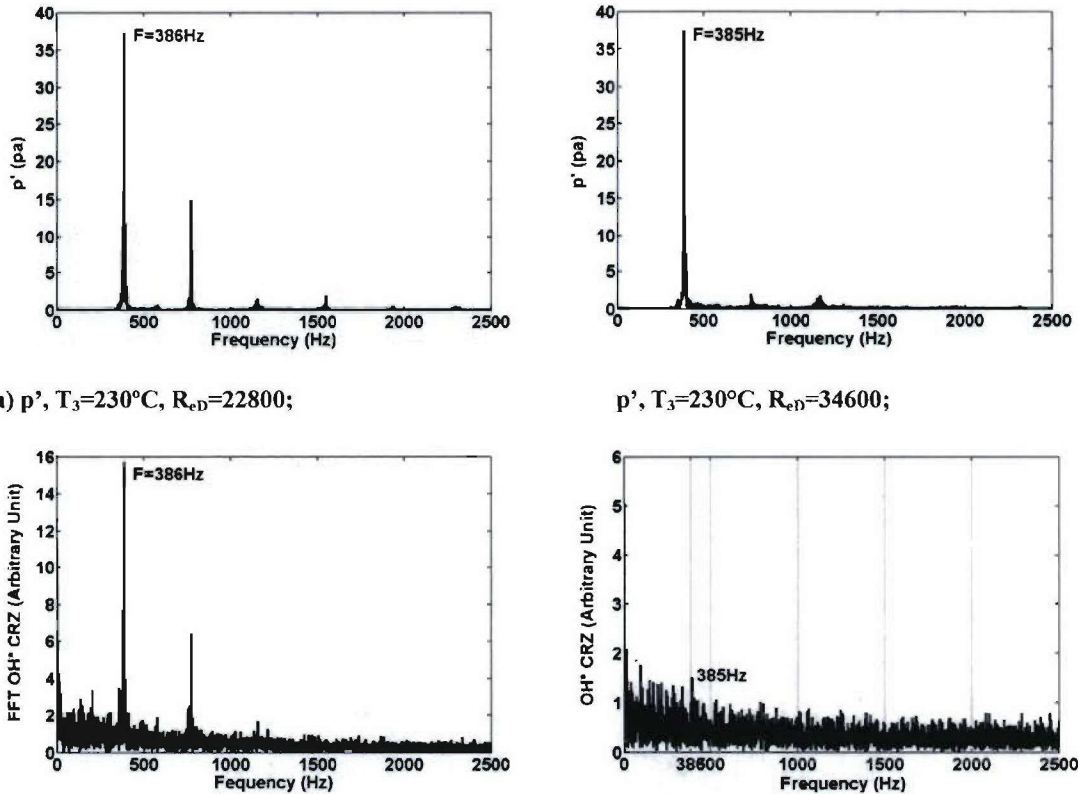
(b) OH*, T_3=230°C, R_{eD}=22800;   OH*, T_3=230°C, R_{eD}=34600;

Figure 6.3: FFT Spectra of p' and OH* for R_{eD}=22800, 34600 at T_3=230°C, propane, L_{mt} = 0, C_R=1, S5545C45.

The comparison of Total OH* (Fig. 4.4) shows the radical intensity or approximate reaction rate at T_3=25°C, 230°C follows the same trend line and the inlet temperature has little effect on the overall reaction rate when the inlet air mass flow rate is kept at the same.

For ethanol at 100% pilot fuel condition, the pressure oscillation was tremendously increased when Reynolds number reaches up to 45700 (Fig. 4.5), in which case the pressure drop cross the TARS is about 6.8%. Comparison of OH* between CRZ and shear layer flame zone shows that the oscillations of the overall flame in these two regions increase near LBO for all inlet flow rates. The oscillation of radicals within CRZ, however, has minimum values somewhere around 0.45 ~ 0.6, which increases with the Reynolds number. Correspondingly, the LBO is also shifted toward rich side with the increment of Reynolds number. This is understandable because the higher the flow rate the higher the turbulence velocity and strain rate and the easier the flame to blow off.
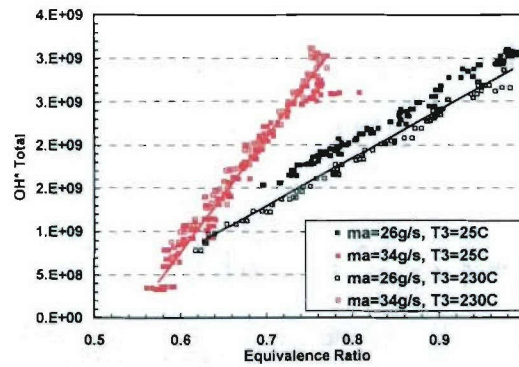
Figure 4.4: Total OH* chemiluminescence (from the integration of OH* image) versus Φ for m_a=26, 34g/s, T_3=25°C, 230°C, propane, L_{mt}=0, C_R=1, S5545C45.
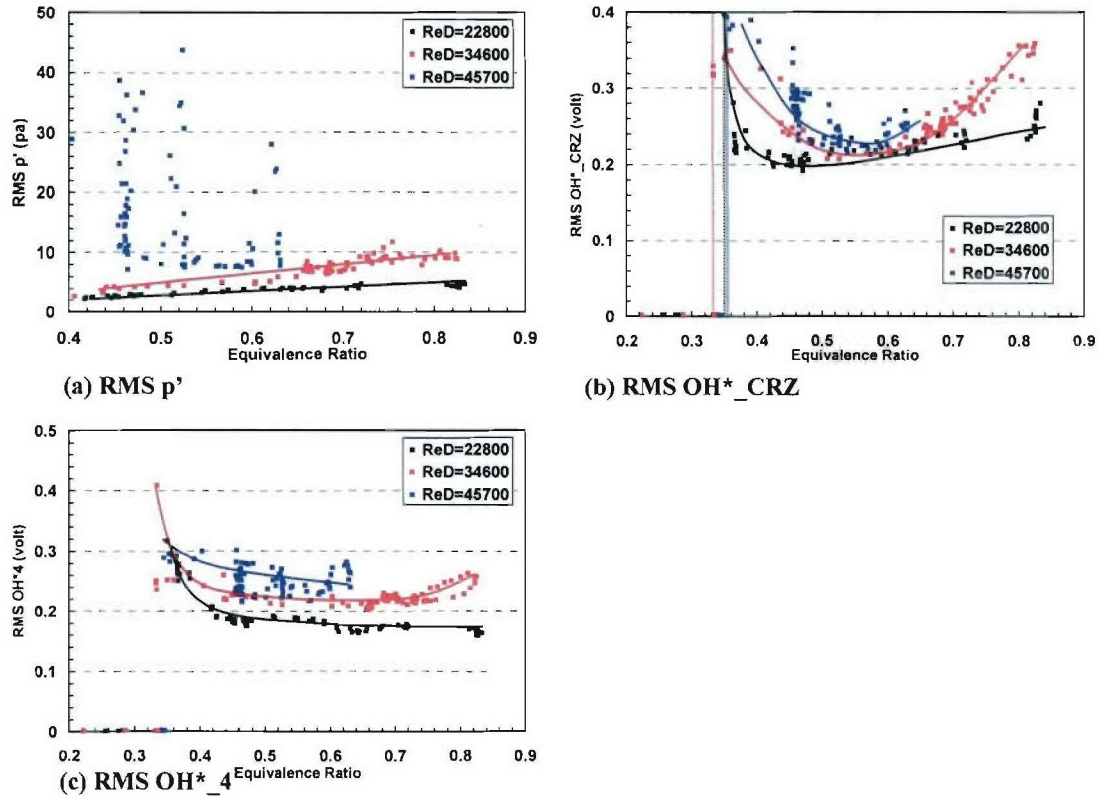
Figure 4.5: Comparison of (a) RMS p', (b) RMS OH*_CRZ, and (c) RMS OH*_4 for R_{eD}=22800, 34600, and 45700 at T_3=230°C, Ethanol, 100% pilot fuel, S5545C45, L_{mt}=0, C_R=1.

6.1.2 Fuel Split

As discussed in last chapter, fuel split between pilot and main will affect emissions and pressure oscillation. 50% pilot fuel generates higher pressure oscillation but normally less NO_x emission. The combustion is easier to get into instability at higher flow rate than at lower flow rate, at partial pilot fuel case than at 100%. At R_{eD}=34600 and 50% pilot fuel, combustion instability occurs at Φ=0.76 and at R_{eD}=45700 and 100% pilot fuel it occurs Φ=0.56 (Fig. 4.6a). OH*_CRZ of Jet-A also characterizes flame pre-LBO behavior and so does the OH* radical from the fiber 4. The behavior of flame in both CRZ and shear layer regions for Jet-A is similar with that of ethanol, indicating this common feature is shared by liquid fuel with different

property and fuel split. 50% pilot fuel case has the smallest operation range whereas the LBO limit slightly increases with Reynolds number. This emphasizes the significant effect of fuel split on LBO.

The dominant frequencies of combustion instability change with operating conditions. The FFT spectra of two different operating conditions corresponding to sudden p' jump in Fig. 4.6a are shown in Fig. 4.7. The dominant instability frequency is shifted from 700Hz for R_{eD}=45700, 100% pilot fuel, to 1429 Hz for R_{eD}=34600, 50% pilot fuel. The distinction between the two frequencies indicates that distinct modes or harmonics of one fundamental frequency might be excited based on air flow rate and fuel distribution.
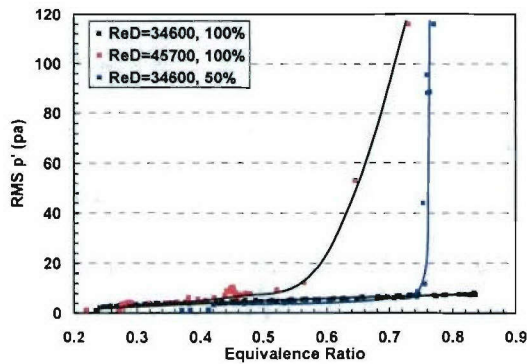
(a) RMS p'
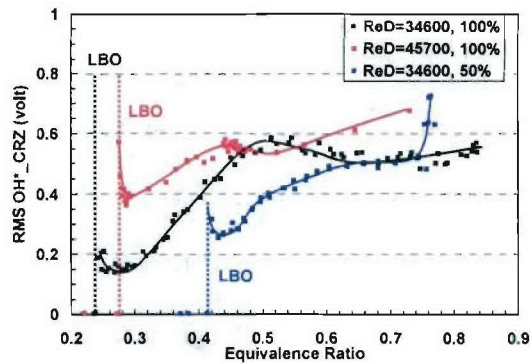
(b) RMS OH*_CRZ
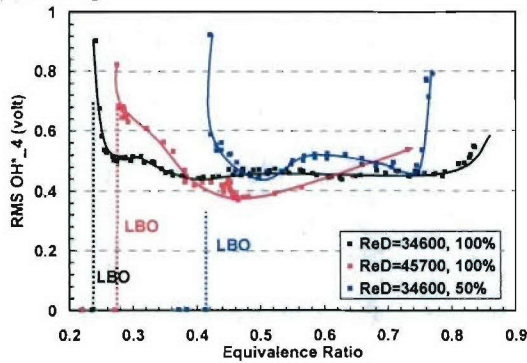
(C) RMS OH*_4

Figure 4.6: Comparison of (a) RMS p', (b) RMS OH*_CRZ, and (c) RMS OH*_4 for Jet-A 50%, 100% pilot fuel at R_{eD}=34600, 45700, T_3=230°C, S5545C45, L_{int}=0, C_R=1.
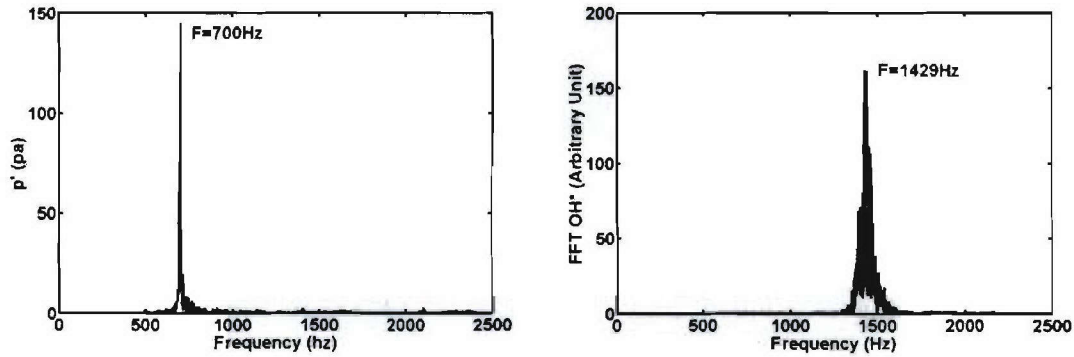
(a) R_{eD}=45700, 100% pilot fuel, Φ=0.6   (b) R_{eD}=34600, 50% pilot fuel, Φ=0.75

Figure 4.7: Spectra for different operating conditions: (a) R_{eD}=45700, 100% pilot fuel; (b) R_{eD}=34600, 50% pilot Jet-A fuel, S5545C45.

6.2 Effects of Geometry Parameters on Combustion dynamics

6.2.1 Swirl Configurations

Oscillations of pressure and flame radicals of two swirler configurations, co-rotating swirler S554545 and counter-rotating swirler S55454C45, are compared in Fig. 4.8. Due to the difficulty in balancing optical signals for different swirl configurations, the comparison of oscillations in flame radicals is limited to the signal trend other than their absolute values. The oscillations of pressure slowly increase with equivalence ratio for both configurations but at slightly larger slope and magnitude for co-rotating case. At L_{mt}=0.5, the occurrence of combustion instability for counter-rotating swirler at Φ=0.68, is richer than co-rotating one at Φ=0.58, indicating the counter-rotating swirler has more margin to avoid severe combustion instability. The oscillations of flame in CRZ reach the maximum value at Φ=0.58, 0.50 for the co- and counter rotating swirlers, respectively. The concurrence of strong oscillations in pressure and flame for co-rotating swirler (Fig. 4.8 a and b, L_{mt}=0.5) may contribute to its early initialization of combustion instability. This initialization, which is very important for further understanding of combustion instability, may have close relationship with the flame oscillations in the central

recirculation region. This point is further clarified by the flat section of oscillation in OH*4 of shear layer flame region over $\Phi = 0.3 \sim 0.65$ for both swirlers with/without mixing tube. Pandalai and Mongia (1998) realized that the flame instability was improved when the central recirculation zone was either absent or minimal for certain designs of DLE engine. The close correlation between oscillation in CRZ and pressure may be one explanation for this observation.
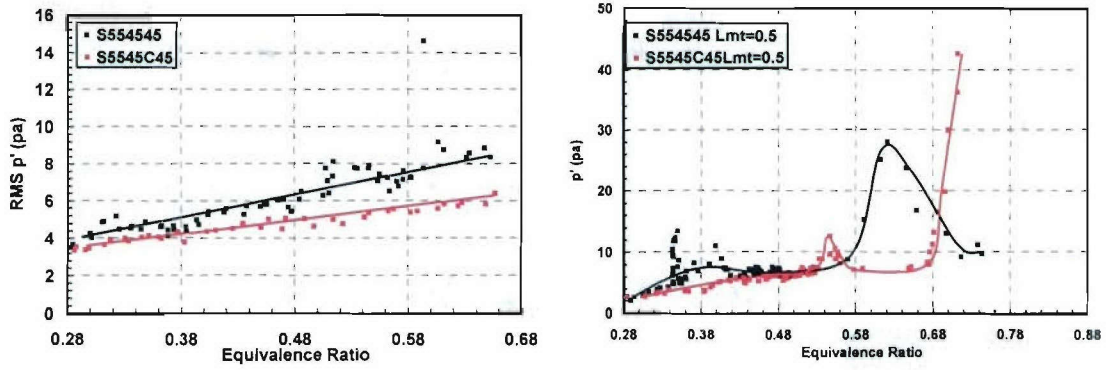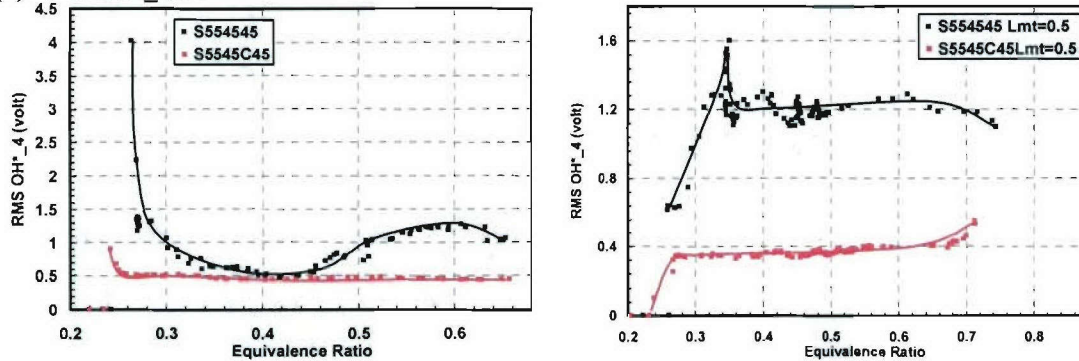

(a) RMS p'
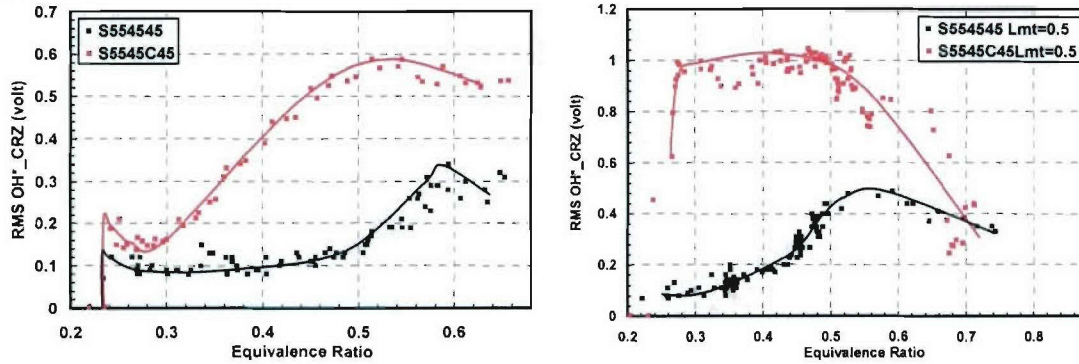
(b) RMS OH*_CRZ

(3) RMS OH*_4 $L_{mt}=0$ $L_{mt}=0.5$

Figure 6.8: Comparison of oscillations in pressure and flame for swirler configurations of L_{mt}=0, 0.5: S554545 and S5545C45: (a) RMS p'; (b) RMS OH*_CRZ; (c) RMS OH*_4. 100% pilot Jet-A fuel.

Figure 4.9 depicts the oscillations in pressure and OH* for 50% pilot fuel case. The combustion of the counter-rotating swirler is fairly stable over Φ =0.38~0.76 but the early initialization of combustion instability for the co-rotating swirler is also manifested at Φ =0.56. Oscillations for co-rotating swirler are also stronger both in central and shear layer flame regions. Because the fuel split distributes more fuel and thus reaction at shear layer region, oscillations of flame in this region (Fiber 4) show clearly increment of OH* near LBO.
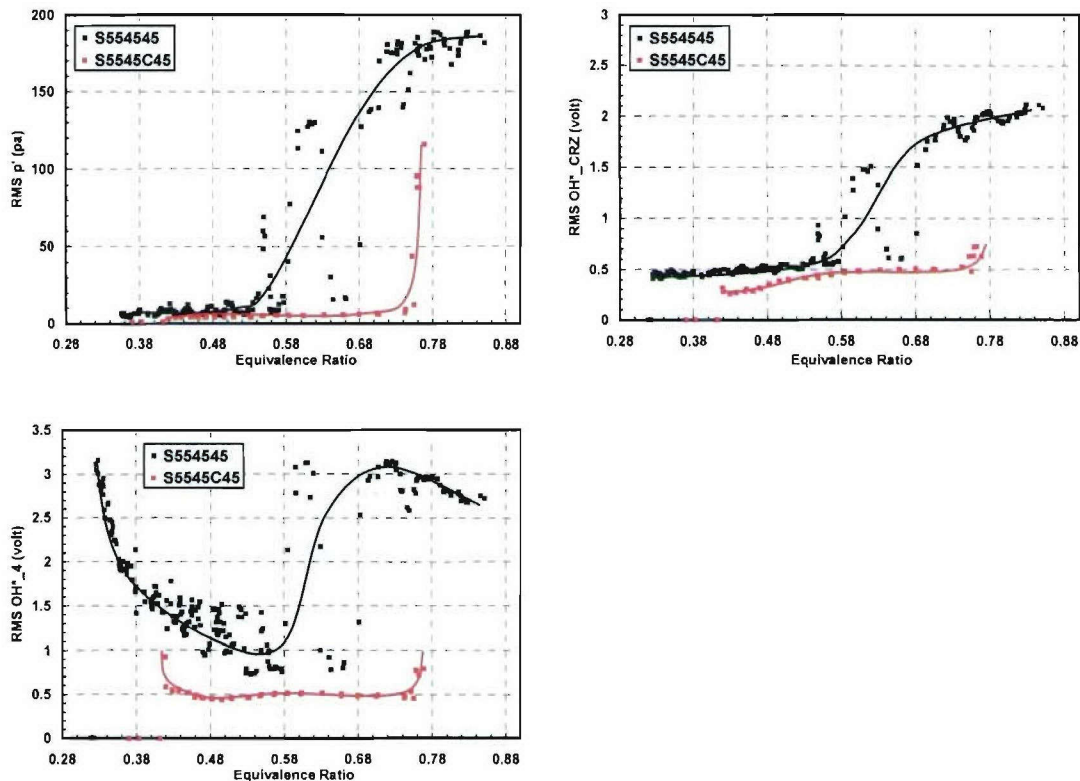
Figure 4.9: Comparison of oscillations in pressure and flame for swirler configurations: S554545 and S5545C45 at 50% pilot fuel, Jet-A, L_{mt}=0.

Spectra of pressure oscillations of the two swirlers at $L_{mt}=0$, 0.5 are shown in Fig. 4.10. As shown in the hotwire measurement, the spectra characteristics of these two swirlers ensemble each other in isothermal flows. The spectra of pressure oscillations confirm the similarity between these two swirler configurations at $L_{mt}=0.5$ (Fig. 4.10 b and c) in terms of dominant frequencies, 336Hz and 339Hz and their magnitudes (30~35pa). The frequency of $L_{mt}=0.5$ is lower than that of $L_{mt}=0$ because the over all combustion chamber length is longer when mixing tube is added and combustion occurs inside this tube.

(a)

(b)

(c)
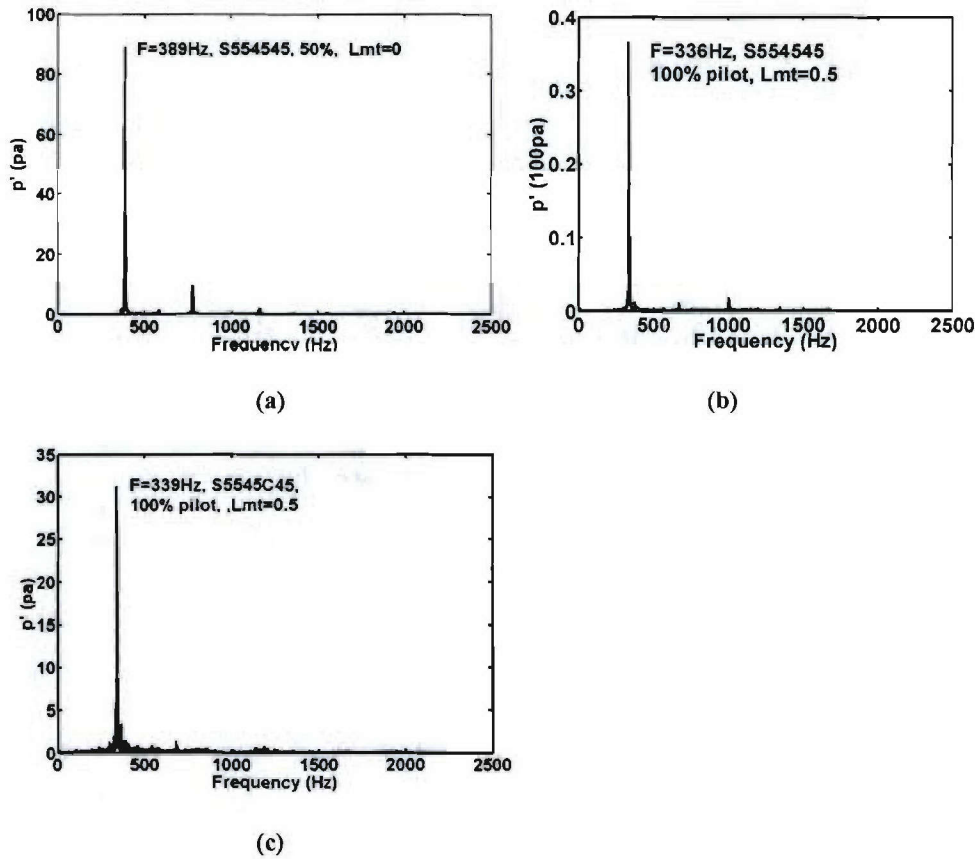
Figure 4.10: Spectra of different geometries: (a) S554545, 50% pilot fuel, $L_{mt}=0$; (b) S554545, 100% pilot fuel, $L_{mt}=0.5$; (c) S5545C45, 100% pilot fuel, $L_{mt}=0.5$.

Therefore, from combustion dynamic point, the co-rotating swirler has leaner LBO but is easier to run into combustion instability especially in case of partial pilot fuel with mixing tube.

The counter-rotating swirl may be a better option for premixed combustion in avoidance of unstable combustion.

4.2.2 Length of Mixing Tube

The effect of mixing tube on oscillations of pressure and flame can also be seen from Fig. 4.8. Mixing tube causes combustion instability and generates large oscillation of pressure and flame in the shear layer region when the combustion is sufficiently rich. It is interestingly to notice that the flame oscillation within CRZ for counter-rotating swirler keeps at high value from $\Phi=0.3$ to 0.5, possibly causing LBO at higher equivalence ratio.

6.2.3 Air-assist

Air-assist is effective on modify the combustion dynamics through its enhancement of fuel injection, penetration and fuel/air mixing. The oscillation of pressure and flame is suppressed by air-assist for both 100% and 50% pilot fuel cases (Fig. 4. 11). By suppression of pressure oscillation, the occurrence of instability was postponed from $\Phi=0.68$ to 0.76 for 100% pilot and was totally eliminated for 50% pilot fuel case. The Air-assist reduces locally the flame oscillation both in CRZ and shear layer region by dispersing the flame and forming a large combustion region. This dispersion in fuel/air mixing and chemical reaction helps in suppression of pressure oscillation and also reduction of NO_x and CO emissions as shown in last chapter.
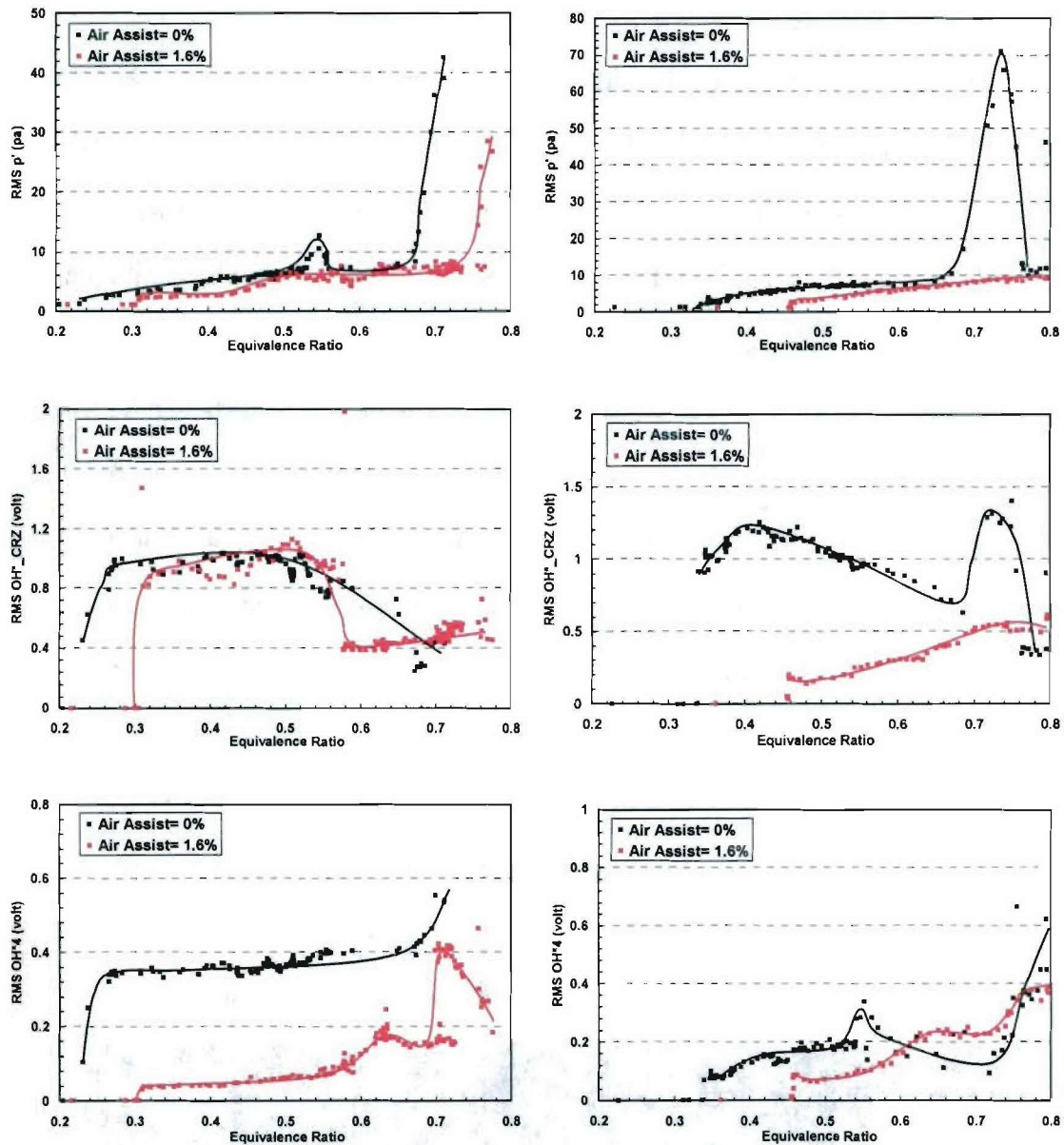
100% pilot fuel   50% pilot fuel

Figure 6.11: Comparison of oscillation in pressure and flame for air-assist with 100% and 50% pilot fuel: S5545C45, L_{mt}=0.5, R_{eD}=34600, T_3=230°C, Jet-A.

4.3 Lean Blow Off (LBO)

Lean blow off occurs when the combustion gets over lean flammability limit. When the fuel equivalence ratio becomes lower and so the flame temperature and heat release rate, the flame strain rate caused by turbulence velocity fluctuation will extinguish the flame (Warnatz, et al. 1996). LBO may take different forms depending on premixed or non-premixed combustion and the type of fuel used. A sequence of OH* chemiluminescence images of premixed combustion is shown in Fig. 4. 12 when Φ decreased down to LBO. The chemical reaction rate, which is represented by the pixel intensity, gradually weakens as Φ reduces from 0.86 to 0.71. The change of flame shape is fairly small during this phase till $\Phi=0.69$ when the flame is lifted, showing a long and narrow "neck" with the flame propagating straight upwards at almost zero expansion angle. Very close to LBO at $\Phi=0.67 \sim 0.57$, the "neck" of flame totally disappears and the flame floats above the fuel nozzle. The detachment of the flame occurs in a manner of sudden and this discontinuity in flame oscillation was detected by optical fibers 1 and 4 simultaneously (Fig. 4.13). The sudden lift moves the flame away from these optical fibers and dramatically reduces their signal levels. This lift-off flame behavior is typical for premixed combustion with gaseous fuel at low inlet temperature, which is also pictured by Muruganandam et al. (2004).
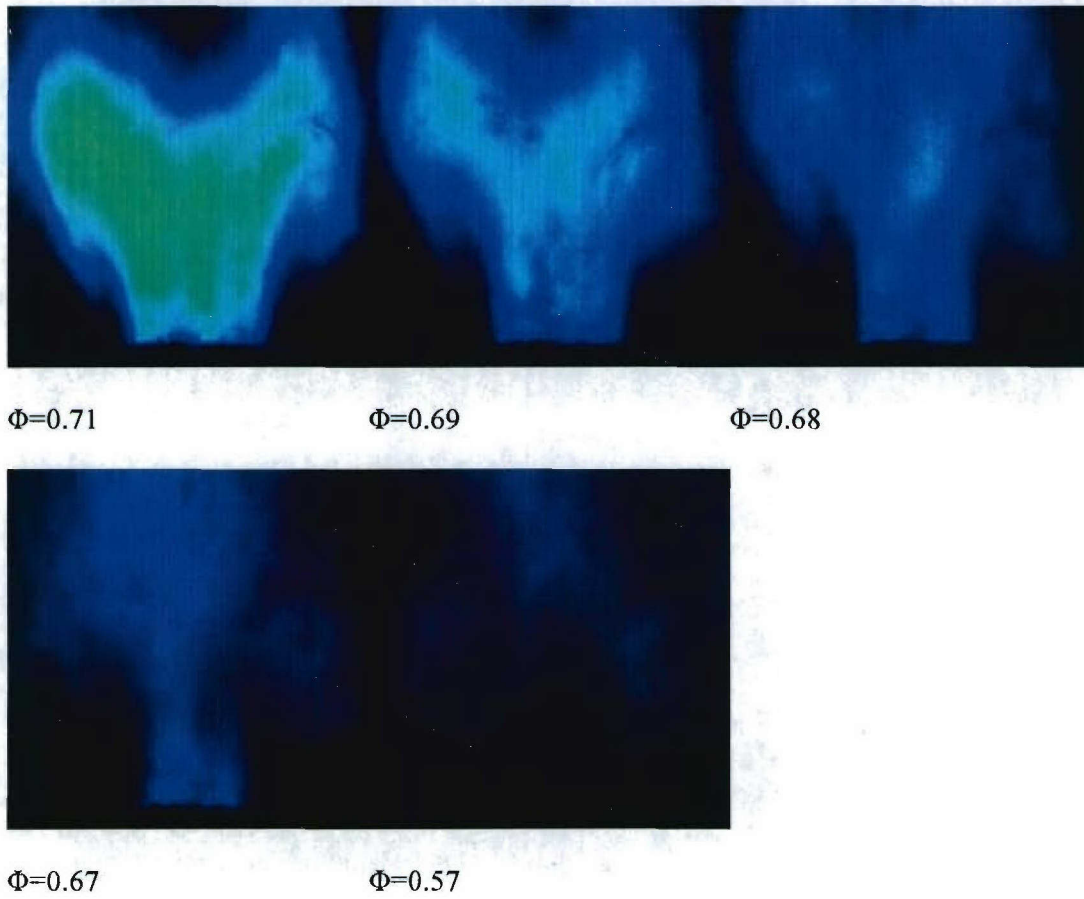

$\Phi=0.86$ $\Phi=0.83$ $\Phi=0.78$

$\Phi=0.71$ $\Phi=0.69$ $\Phi=0.68$

$\Phi=0.67$ $\Phi=0.57$
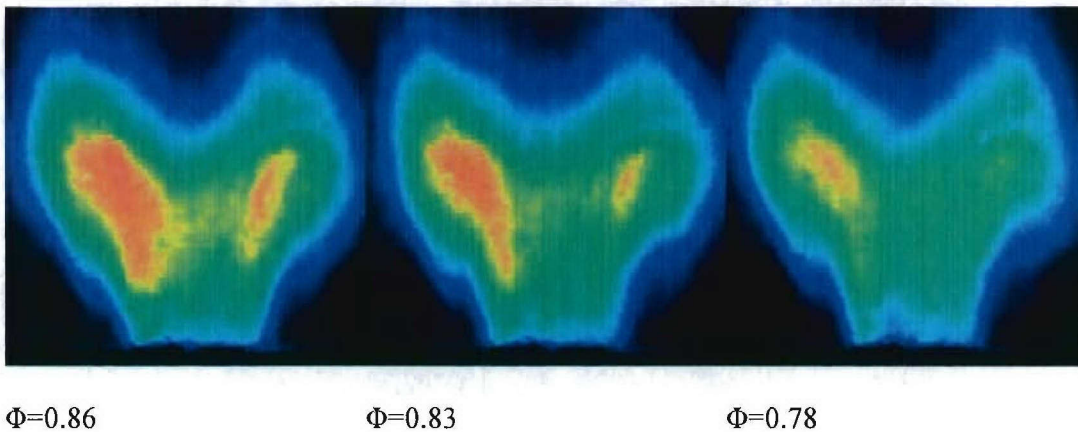
Figure 4.12: Sequence of OH* chemiluminescence images with Φ approaching LBO at $\Phi=0.53$. S5545C45, Propane, $R_{eD}=33000$, $T_3=25°C$, $L_{mt}=0.5$.
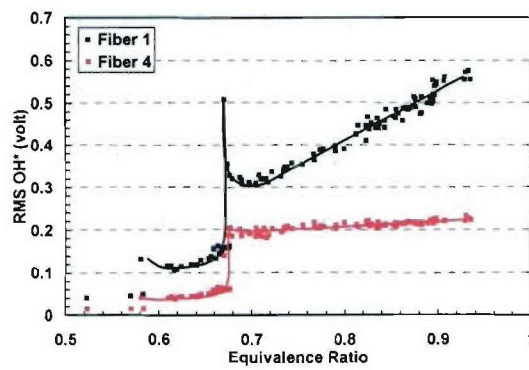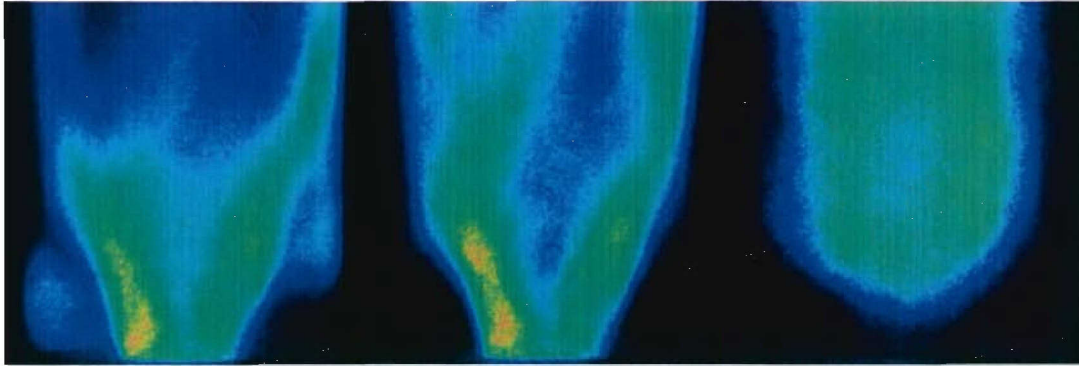

Figure 4.13: Dependence of OH* on equivalence ratio for two fibers: Propane, $R_{eD}=33000$, $m_a=26g/s$, $T_3=25°C$, $L_{mt}=0.5$.

Φ=0.48 Φ=0.47 Φ=0.46

Figure 4.14: Sequence of OH* chemiluminescence images with Φ approaching LBO at Φ=0.45. S554545, Propane, R_{eD}=22800, ma=26g/s, T_3=230°C, L_{mt}=0.5.

LBO can be extended if co-rotating swirler is used at higher inlet air temperatures. As in Fig. 4.14, the flame is anchored at the left corner in addition to the main flame zone. This corner flame extinguishes first when approaching LBO. Unlike flame for counter-swirling case, there is no straight "neck" region for this flame. Very close to LBO, the flame still attaches to the nozzle with a very small contact area. This transition behavior eliminates the sudden lift off of flame and extends the LBO from 0.53 to 0.45.

Flame without sudden lift-off is also observed from non-premixed combustion with counter-rotating swirler in Fig. 4.15. Without mixing tube, the flame has an expansion angle of about 60° (Φ =0.76) as contrast to less than 30° for L_{mt}=0.5. Along with the decrement of Φ from 0.69 to 0.59, the intense flame moves from the jet zone towards the combustor wall and the corner. At Φ =0.58, no corner flame is observed and local extinction regions show up, interweaved with weak flame zones. The flame keeps attaching to the nozzle even barely seen right near LBO. Sporadically, small intense flame sparkled inside the central weak combustion zone, manifested as the increment of flame oscillation in Fig. 4.16 for fiber 1. Meanwhile, the flame outside the

CRZ gradually reduces its intensity as the trend line of fiber 4 signal. The flame oscillation within CRZ is also shown by the comparison of spectra of fiber 1 signal at Φ=0.6, 0.7 in Fig. 6.16b. Magnitude of flame oscillations increase about 50% in the lower frequency band less than 50Hz when Φ decreases from 0.7 to 0.6.
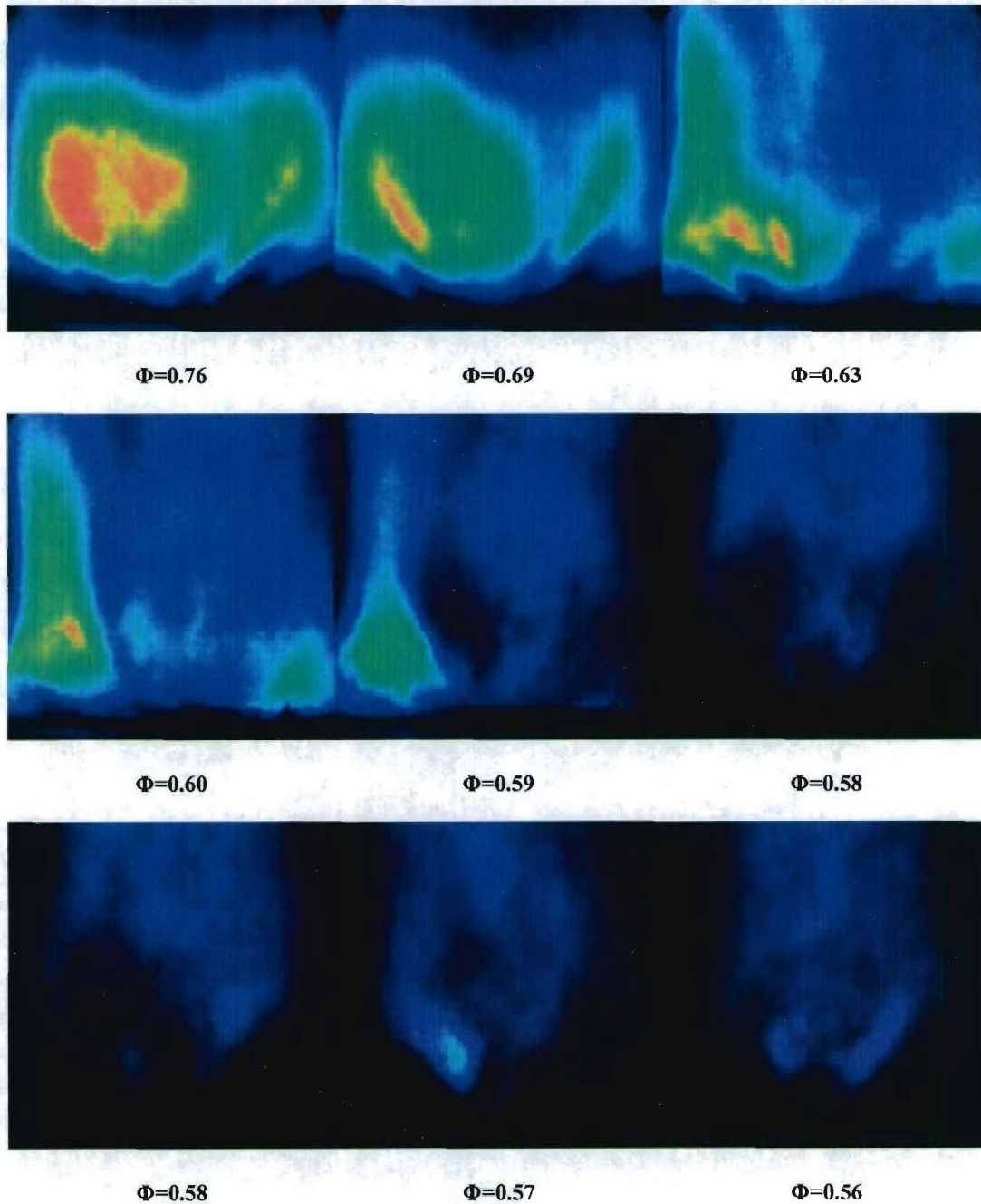

Φ=0.76   Φ=0.69   Φ=0.63

Φ=0.60   Φ=0.59   Φ=0.58

Φ=0.58   Φ=0.57   Φ=0.56

Figure 4.15: Sequence of OH* chemiluminescence images approaching LBO without flame lift-off: propane, S5545C45, R_{eD}=50000, T_3=25°C, L_{mt}=0.

Spectra analysis of dynamic signals from the microphone and fiber 1 shows the relationship between the dominant frequencies, their magnitudes and the equivalence ratio. The magnitude and dominant frequency of combustion noise (p') has quasi-linear relationship with Φ. The peak frequency clusters in a band of 360 ~ 420Hz. The optical signal, however, has fairly large dispersion of the dominant frequency, up to 240Hz at most stable state (Φ=0.7) and low down to few Hertz at Φ=0.6. The peak magnitude follows the same trend as RMS value of OH* in Fig. 4.16. This peak oscillation near LBO is, if not the determinate, essential for final flame extinction. The manifestation of high dominant frequency at most stable case and lower frequency near LBO in Fig. 4.17 suggests that high frequency pulsation for pilot flame, which burns at the CRZ, would be one possible approach for extending LBO without hurting NO_x emission by increase of pilot fuel flow rate.

(a) (b)
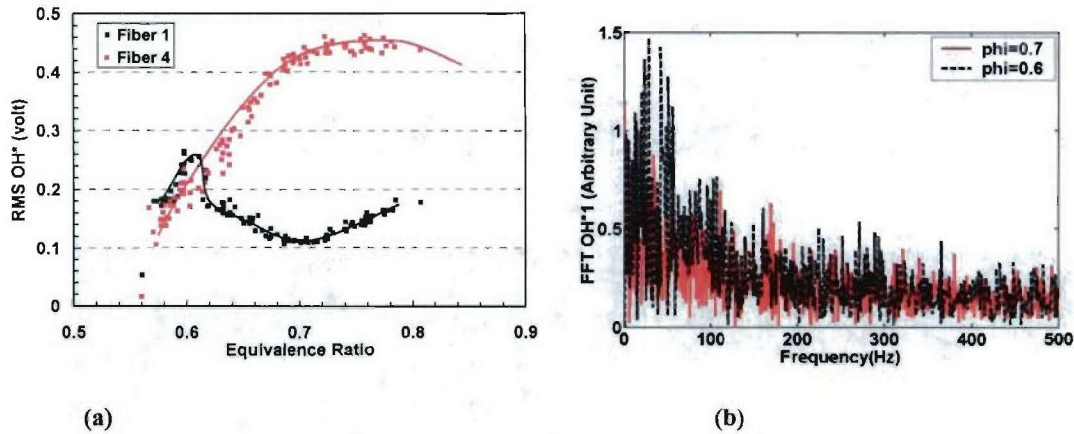
Figure 4.16: (a) Dependence of OH* on equivalence ratio at two fiber locations and (b) comparison of spectra of fiber 1 signal at Φ=0.6, 0.7: Propane, R_{eD}=50000, T_3=25°C, L_{mt}=0.
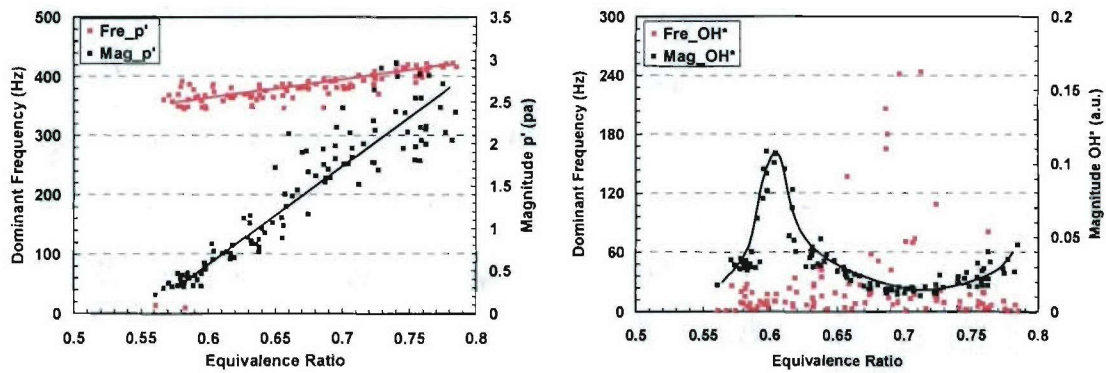
Figure 4.17: Dominant frequency and magnitude of pressure and OH* oscillation versus Φ. Propane, R_{eD}=50000, T_3=25°C, L_{mt}=0.

For spray combustion in swirling flow, such as Jet-A for TARS, LBO is also manifested by the increment of flame oscillation near LBO. A sequence of OH* images of 50% pilot fuel non-premixed flame is shown in Fig. 4.18. The flame is fairly compact and intense, gradually moving close to fuel nozzle as Φ decreases. The flame shrinks its shape along with Φ decrement while keeping its attachment to the nozzle. The change of the flame shape on its edge reflects on the oscillation of flame observed by fiber 4 in Fig. 4.19. The dependence of spectra on Φ for microphone and OH*4 signals is also included in this figure. Except for the combustion instability at Φ=0.75, the dominant frequency of OH* is less than 50Hz and mostly around single digit, while the pressure oscillation has its dominant frequency at around 360Hz over Φ=0.42 ~ 0.78. When instability occurs, the large magnitude oscillations of pressure and OH* are in the same frequency. This dominant combustion instability frequency is among the dominant frequency of dynamic pressure when combustion is even far away from instability. This suggests that acoustic combustion instability is buried in stable combustion and pressure oscillation may be the primary trigger leading instability. This conjecture, although hardly

proved due to the feedback coupling loop of pressure and heat release, is indicated by the time tracing of p' and OH*. We will discuss this in the next section.

The LBO limit for different operating cases are summarized in Table 4.1. Mixing tube tends to move LBO to fuel rich side so does the counter-rotating swirler. LBO is not sensitive to air-assist, indicating an advantage of this active control approach for emission control. Fig. 4.19 shows the LBO of co/counter rotating swirlers at different air flow rates. In terms of LBO, co-rotating swirler is advantageous compared with the counter one.

Φ=0.77 $\quad\quad\quad\quad\quad$ Φ=0.68 $\quad\quad\quad\quad\quad$ Φ=0.58

Φ=0.48 $\quad\quad\quad\quad\quad$ Φ=0.43 $\quad\quad\quad\quad\quad$ Φ=0.42
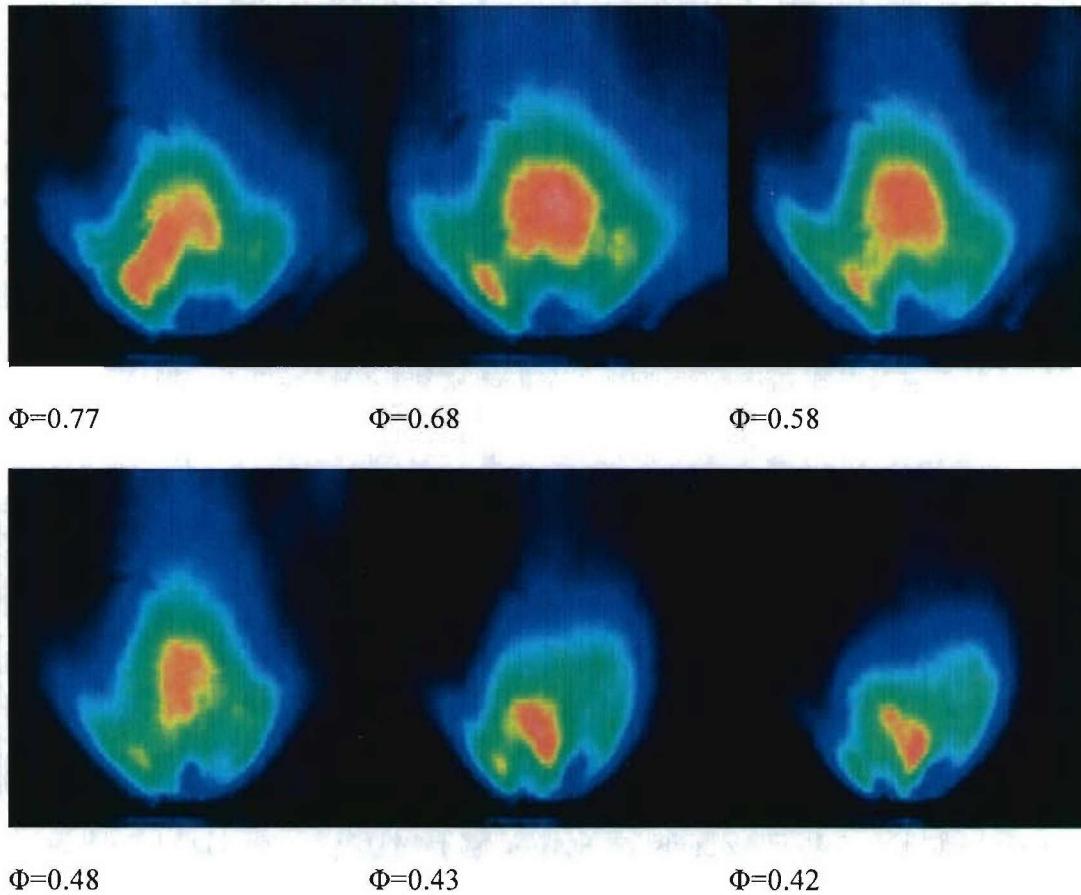
Figure 4.18: Sequence of OH* chemiluminescence images approaching LBO without flame lift-off: Jet-A, 50% pilot fuel, R_{eD}=34600, m_a=34g/s, S5545C45, T_3=230°C, L_{mt}=0.
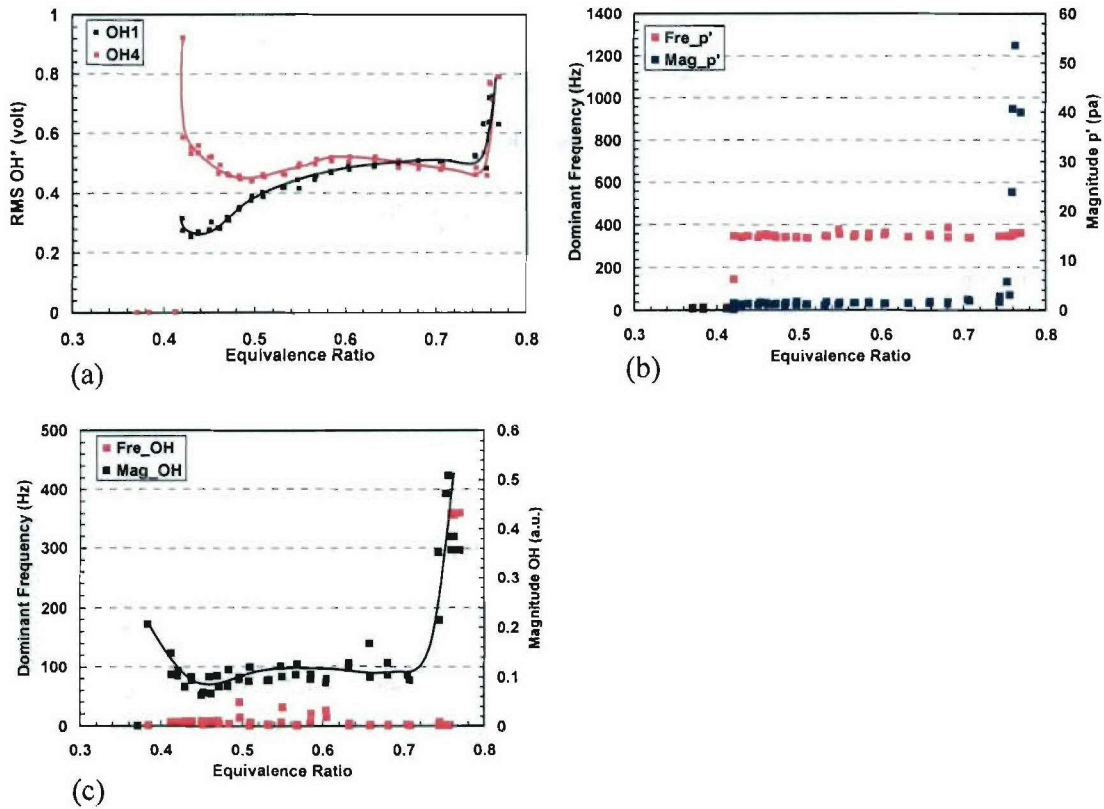
Figure 4.18: Oscillations of OH* and pressure in time and frequency domain: (a) RMS OH* versus Φ; (b) dominant frequency and magnitude of pressure; (c) dominant frequency and magnitude of OH* versus Φ. Jet-A, R_{eD}=34600, T_3=230°C, L_{mt}=0.
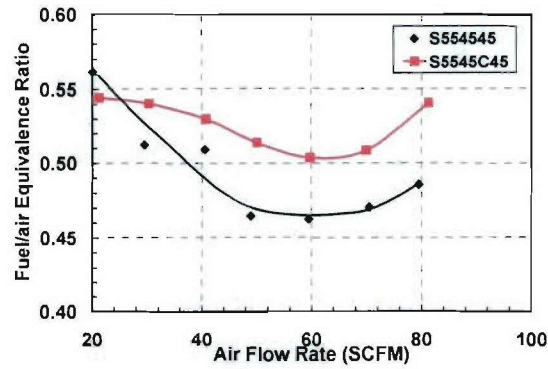
Figure 4.19: Comparison of LBO for swirler configurations: S554545 and S5545C45: Propane, T_3=230°C, L_{mt}=0.

4.4 Combustion Instability

For the combustor system we study here, combustion instability occurs when fuel gets sufficiently rich, more fuel is distributed into main fuel circuit liquid fuel, or the mixing tube is inserted. In this section, we mainly discuss different modes manifested as combustion instability for different geometries or operating conditions, their initialization and the relationship between combustion instability and emissions of different cases.

4.4.1. Propane without mixing tube

For propane without mixing tube, the combustion bursts into unstable above $\Phi = 0.936$. The analysis of pressure and OH* dynamics signals and corresponding NO_x and CO are shown in Fig. 4.19a~f. The test starts with increment of fuel up to unstable combustion and then slowly ramps down to the lean blow off. The combustion noise concentrates in the band of 300~400Hz (Fig. 4.20a) where the instability manifests itself at 386Hz (Fig. 4.20b). Several harmonics are also shown up along with this fundamental frequency. OH* oscillations from all optical fibers show the same instability frequency in addition to the pressure oscillation. A 4th order Butterworth filter centered at the instability frequency with 100Hz band width is used to filter raw dynamic signals of pressure and OH*. The filtered signals are shown in Fig. 4.20d. All signals are approximately in phase with each other, indicating the flame mainly oscillates in the longitudinal direction. The FFT spectra for each of the four OH* signals are shown in Fig. 4.21. In addition to the fundamental (f=387Hz) and the secondary harmonic frequency (f=774Hz), the third harmonic (f=1161Hz) is also shown in circumferential OH*2, 3, 4 except OH*1 within CRZ. This high frequency may cause the phase difference in Fig. 4.20d because the slightly different in phase angle at the fundamental frequency may count for a bigger difference at higher

frequency, which is possibly in circumferential mode. As is shown in last chapter, the occurrence of unstable combustion causes discontinuity in NO_x emission curve and dramatically increases the NO_x formation. The strong oscillations in chemical reaction, which is reflected from oscillations of radicals, consequently cause large oscillations in heat release and temperature, counting for this extra formation of NO_x.
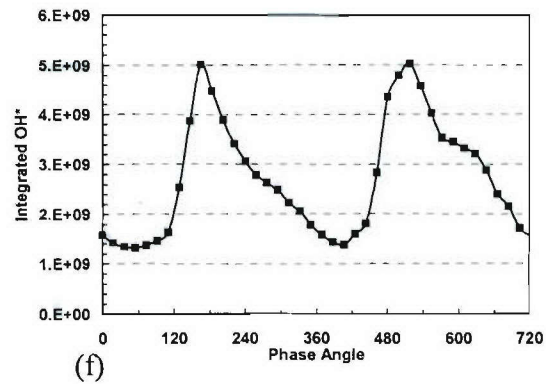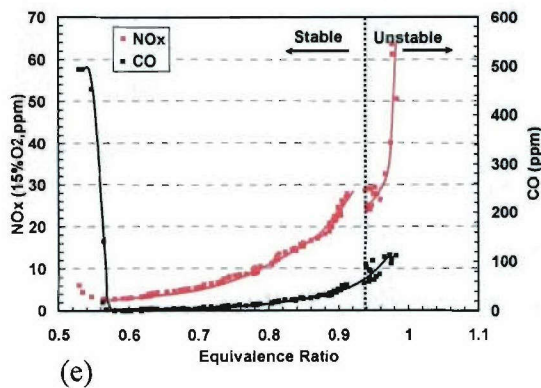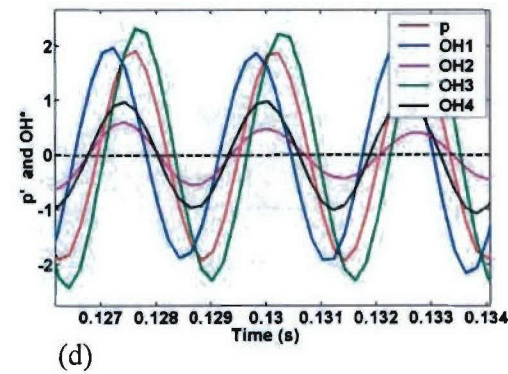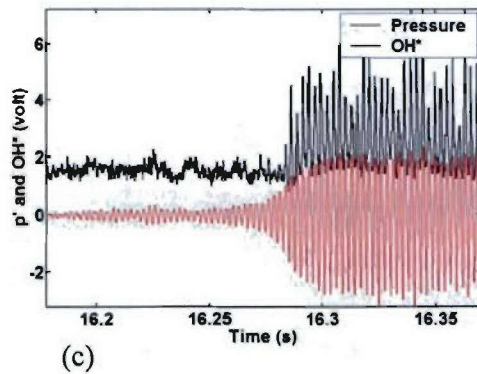

(a)

(b)

(c)

(d)

(e)

(f)
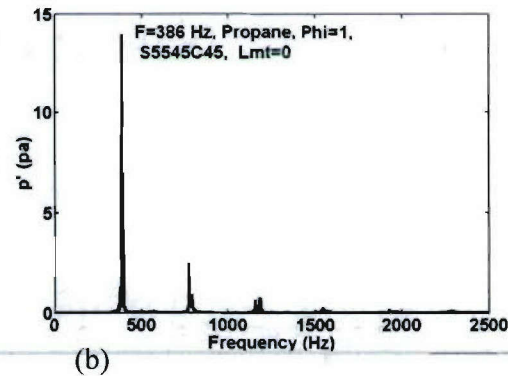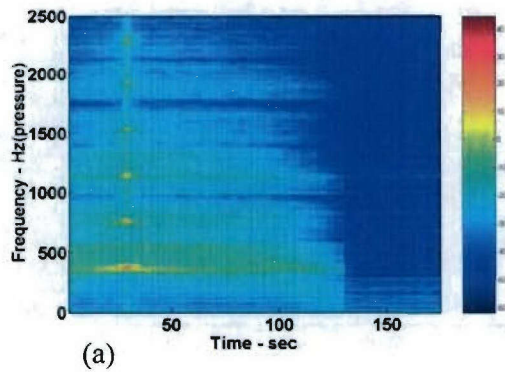
Figure 6.20: Dynamic signals at unstable combustion: (a) Spectra of pressure oscillation; (b) FFT spectra at Φ=1; (c) Initialization of oscillation; (d) Comparison of signals of p' and OH* from 4 channels; (e) Dependence of emissions on Φ; (f) Integrated OH* from images. Propane, T₃=230°C, R_eD=22800, L_mt=0, S5545C45.
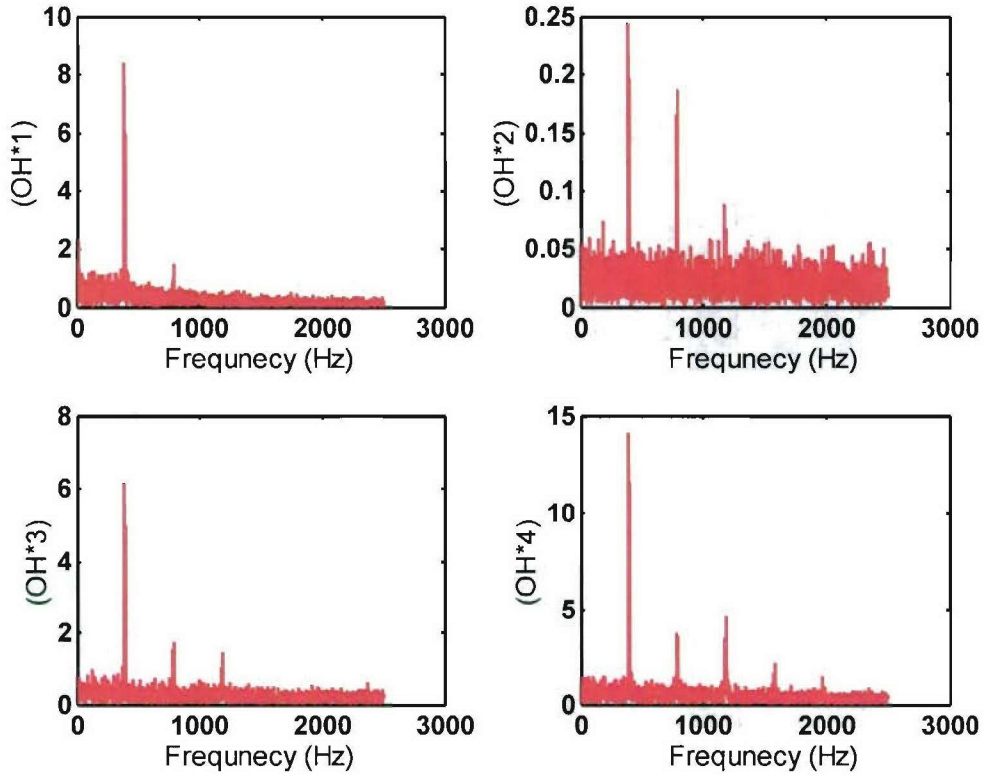
Figure 4.21: Spectra of OH* from 4 channels. Propane, T₃=230°C, R_eD=33000, L_mt=0, S5545C45, propane.

The initialization of this unstable combustion first starts from oscillation grown up in pressure. After a few oscillation cycles, the flame suddenly gets into strong oscillation to complete the feedback loop of hear release and pressure oscillations (Fig. 4.20c). The initial oscillation of pressure indicates that the perturbation from flow dynamics is the source of combustion instability. This mechanism is confirmed by phase-locked PIV measurement for

velocity flow field and will be discussed more in detail after several types of instability phenomena encountered in this multiple swirler are reviewed.

A sequence of OH* images of the unstable combustion at 387Hz is shown in Fig. 4.22. The integration of pixel intensity in each single image is plotted versus phase as Fig. 4.20f. The flame starts with a quasi-flat form at 0° and gradually moves in the axial direction up to 111°. In this stage, the flame also curves at the bottom surface as the consequence of vortex structures forming along the inner edge of the swirling jet. The images at phase 92.5 ° and 111° clearly show this flame structure. Large amount of fuel/air mixture is brought to the central flow ration by the large vortical structures. Flame intensity during this state increases fairly slow, only distributed close to the top surface. After this phase angle, the intense flame region quickly expands to almost the whole flame zone from 129.5 to 166.5 ° when the mixture accumulated from the first stage gets burning. The flame starts to split at 222° and no intense flame region can be distinguished from fairly uniform radical intensity on the both sides of the jet. Flame length gets shorter in a slow pace from 240.5 to 351.5° with distance between the two sides becoming larger and larger.

This type of instability can be identified as longitudinal form from the phase of OH* signals and the motion of flame. The exhaust temperature is measured by type-B thermocouple to be 1400K after correction of thermal radiation. The sound of speed of hot gas can be estimated as 722 m/s based on this temperature. The corresponding quarter wave mode frequency is 395 Hz, which is very close to the instability frequency 387Hz for this case.
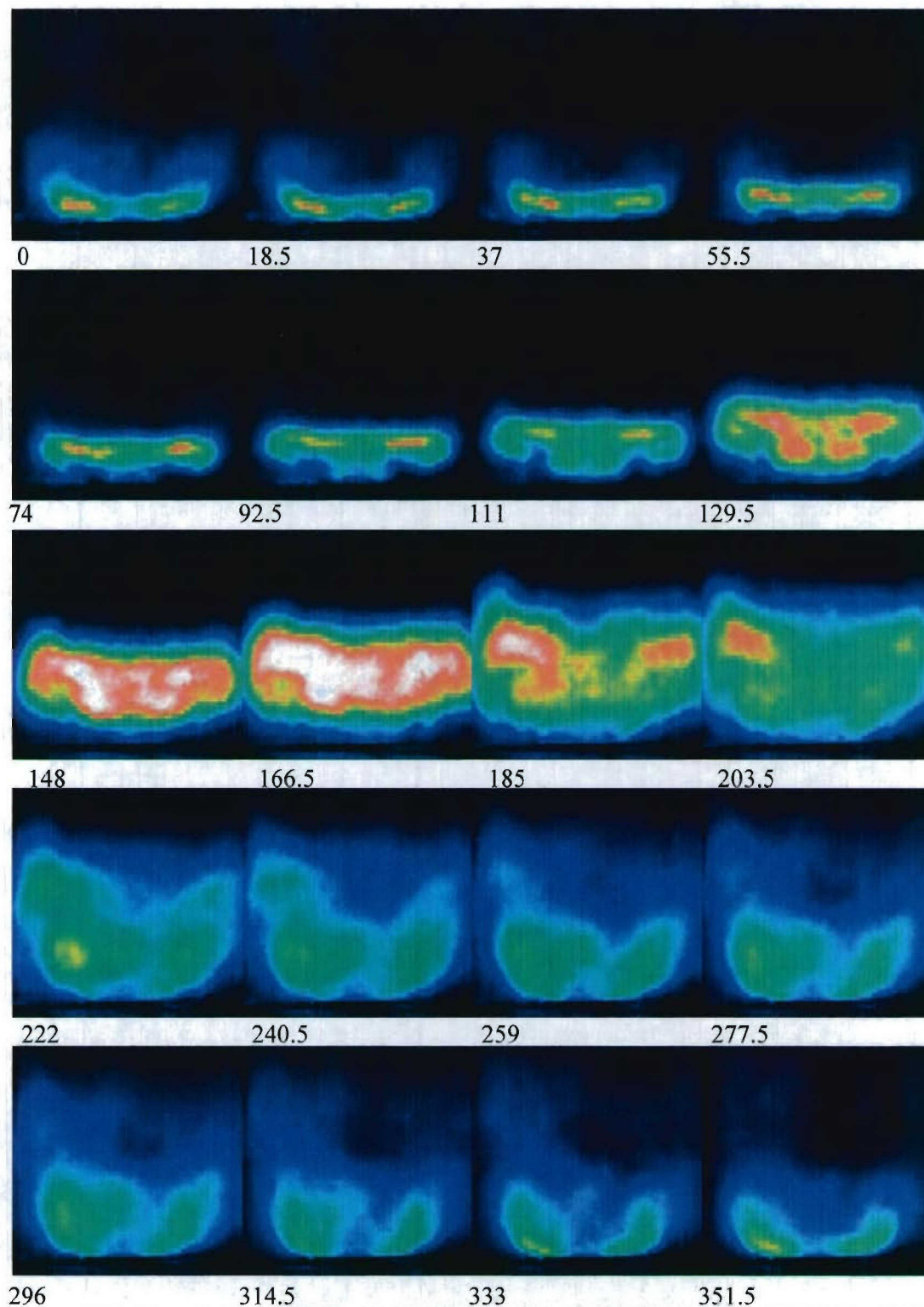
Figure 4.22: Phase locked OH* images at different phase angles. Propane, T_3=230°C, R_{eD}=22800, L_{mt}=0, S5545C45, Φ=1.

4.4.2. Propane with mixing tube

Mixing tube promotes the occurrence of combustion instability. For same operating condition at L_{mt}=0, large magnitude instability takes place at Φ =0.73 and beyond. The instability frequency is around 360Hz and slightly changes with equivalence ratio (Fig. 4.23a, b). The fundamental frequency is lower than that of L_{mt}=0 because the one inch mixing tube increases the combustion chamber length. From the phase relationship in Fig. 4.23c, all other signals are approximately in phase except for the OH*1, which is almost out of phase with the other three optical signals. Despite of the huge variations in dynamic pressure and flame versus Φ as are on RMS p' and OH* curves (Fig. 4.23d), the NO_x and CO emissions continuously increase with Φ without showing maximum at Φ=0.8 (Fig. 4.23e). The integration of OH* images also periodically changes along with p' (Fig. 4.23f).
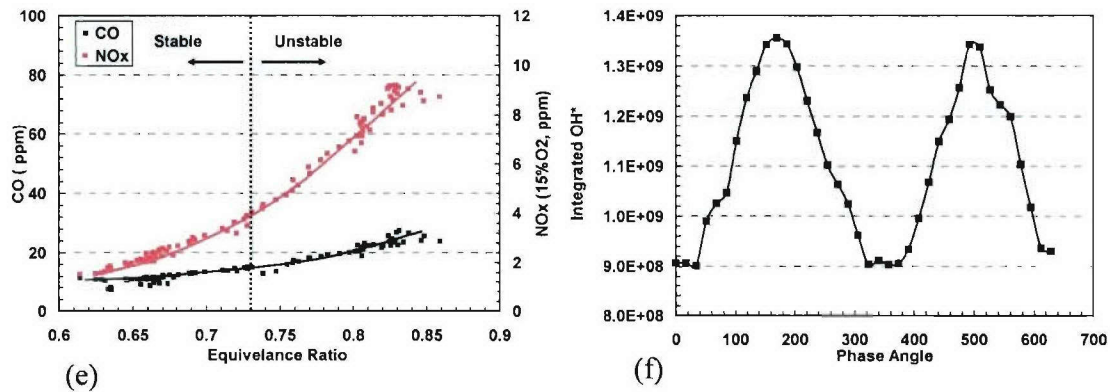

(b)

(c)

(d)
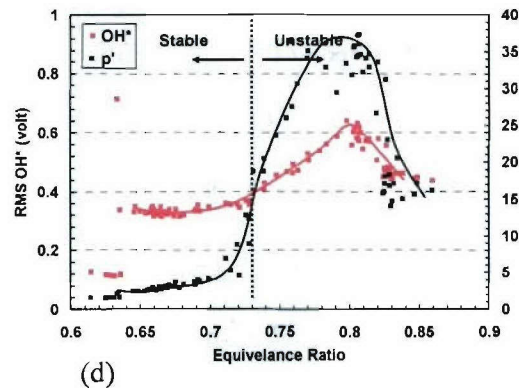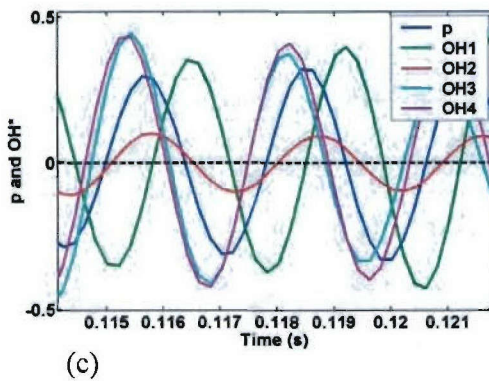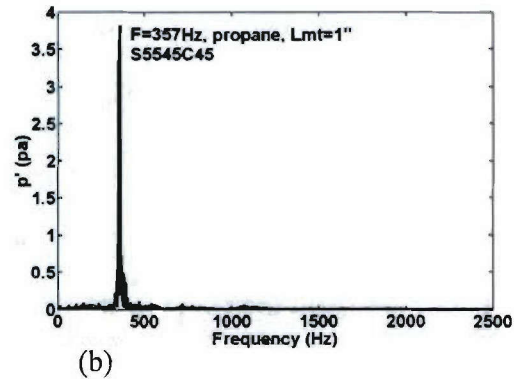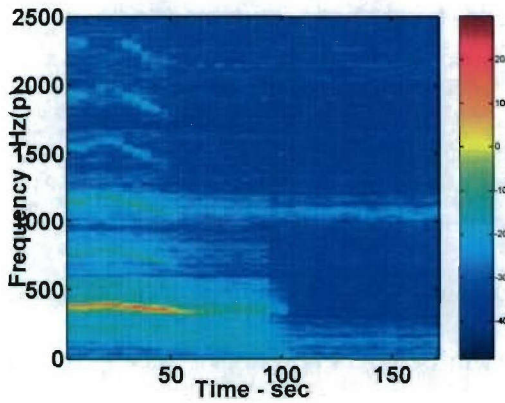
Figure 4.23: Dynamic signals at unstable combustion: (a) p' Waterfall spectra; (b) Spectra of p' at Φ=0.75; (c) Comparison of signals of p' and OH*; (d) Dependence of RMS p' and OH* on Φ; (e) Dependence of NO$_x$ and CO on Φ; (f) Integrated OH* image versus phase angle. Propane, T_3=230°C, R_{eD}=22800, L_{mt}=0.5, S5545C45.

The sequence of OH* images (Fig. 4.24) shows very different behavior for this unstable combustion as compared with that of L_{mt}=0. According to its structure, the flame can be divided into two parts: root and stem. The root part is close to the mixing tube outlet and the stem is on top of the root with larger flame area. During the first half cycle from 0 to 187°, the flame grows up from the root, becomes more and more intense and matures with only stem part left. Then the flame weakens in the stem part until 255°. Starting from this phase, the root part grows into high intense flame along with the flame weakening in the stem part. This cycle periodically repeats with pressure oscillation. The oscillation in flame is possibly caused by periodic change in jet velocity, which has been proposed by Poinsot et al. (1987) to explain vortex driven combustion instability for dump-combustor. The difference in phase angle of OH* signals can be explained by the oscillation of flame in root and stem parts. OH*1 detects the flame in CRZ, which mainly consists the root flame, and captures the strongest oscillation at the about 357°. All the other three fibers detect the flame of stem part that is most intense at 187°. The flame intensity from

root and stem parts is integrated separately and plotted in Fig. 4.24. The OH* from the root and
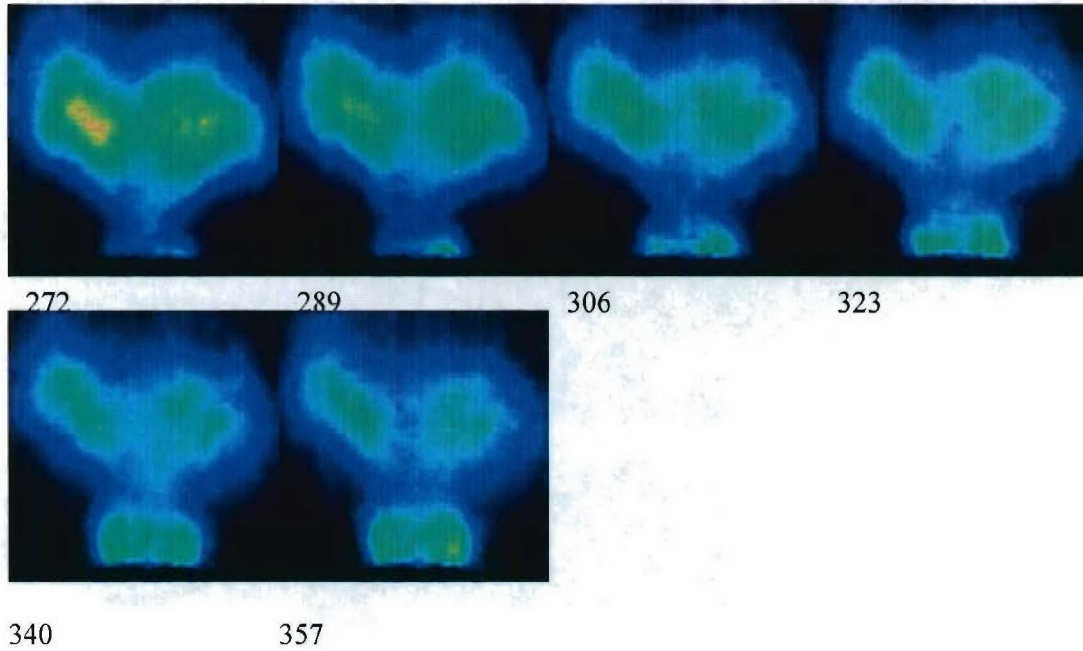
the stem is shown clearly out of phase.
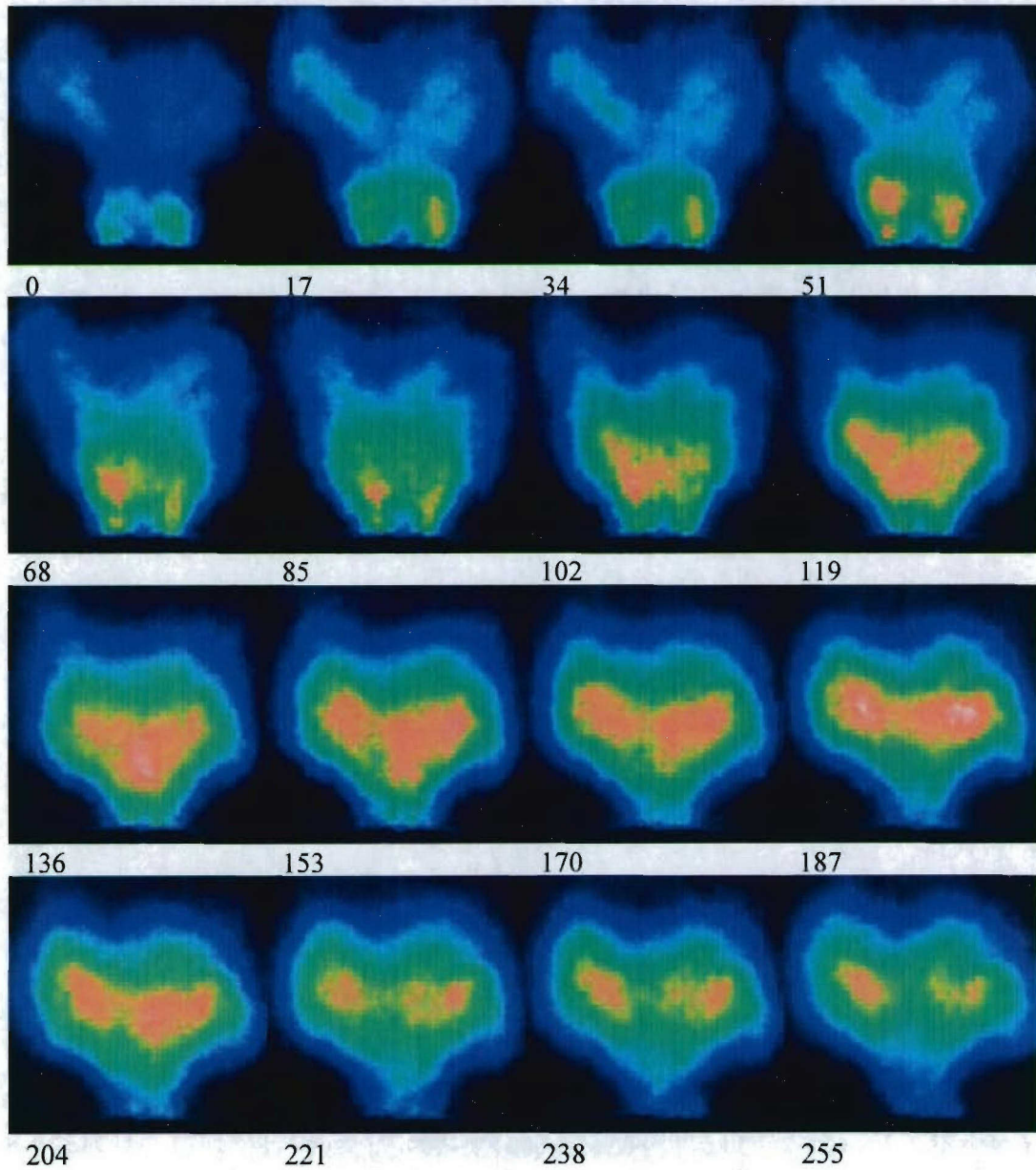
Figure 4.24: Sequence of OH* images in one cycle at different phase angles for unstable combustion. Propane, T_3=230°C, R_{eD}=33000, L_{mt}=0.5, S5545C45, Φ=0.75.

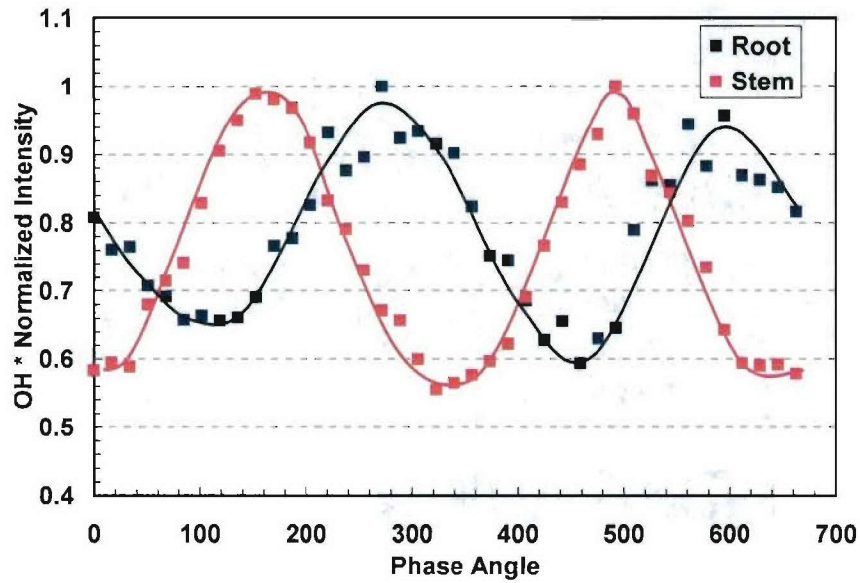**Figure 4.25:** Periodic change of integrated OH* from root and stem parts versus phase angle. Propane, S5545C45, L_{mt}=0.5, T_3=230°C, R_{eD}=22800.

4.4.3. Liquid fuel with 50% pilot fuel

(a)

(b)

(c)

(d)

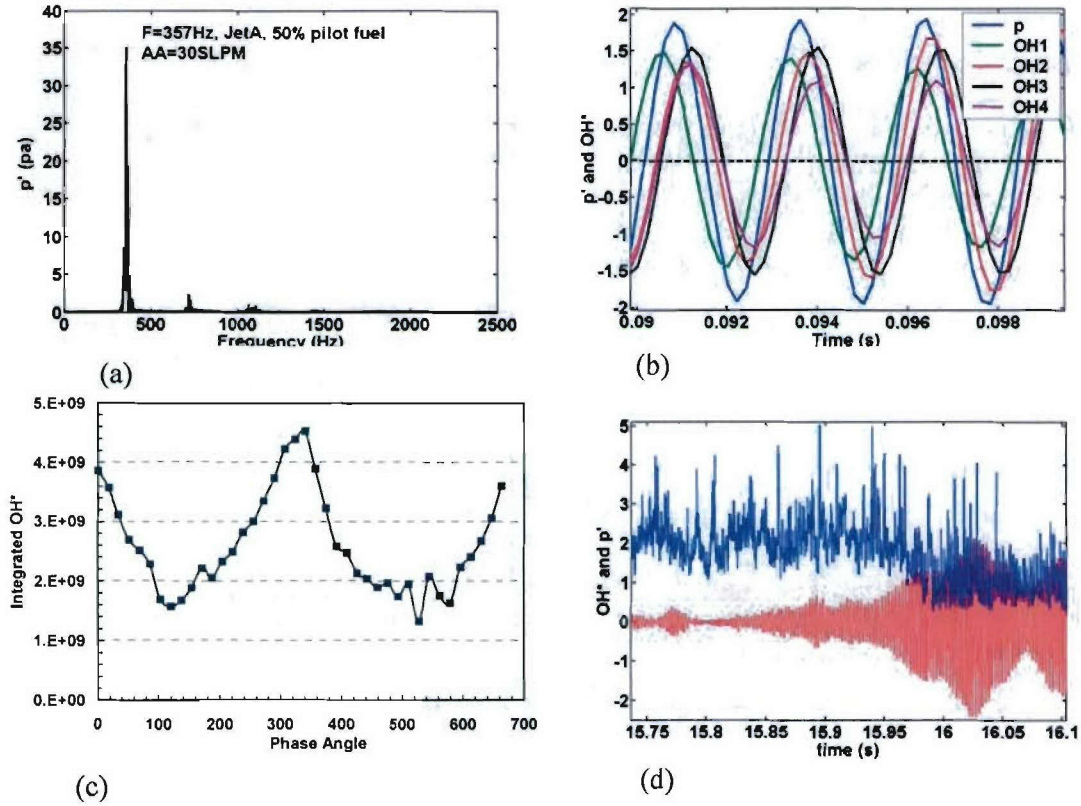**Figure 6.26: Dynamic signals at unstable combustion: (a) Spectra of pressure oscillation; (b) Comparison of signals of p' and OH*; (c) Integrated OH*; (d) Initialization of instability. Jet-A, 50% pilot, T_3=230°C, R_{eD}=34600, L_{mt}=0, S5545C45, Φ=0.6.**

Spray combustion easily gets into unstable combustion when more fuel is distributed from the main circuit for this multiple swirl combustor. Jet-A and Ethanol fuel is used to study combustion instability at 50% pilot fuel case. Spectra of instability pressure signal, the phase relationship of p' and OH* signals, integrated OH* and initialization of unstable combustion of Jet-A are shown in Fig. 4.26 a~d. The dominant frequency is 357Hz at Φ =0.6, with all signals approximately in phase. Phase-locked OH* images shows periodic cycle same as the dominant frequency. The initialization of instability is first triggered by pressure oscillation, same as the

gaseous fuel. This further supports the proposal that combustion instability is mostly rooted from flow dynamic rather than from flame oscillation, which is also identified as one driven mechanism for some cases of combustion instability (Ducruix, et al. 2003). Spectra of the OH* signals show single dominant frequency for circumferential fibers, indicating less possibility to have circumferential instability (Fig. 4.27).
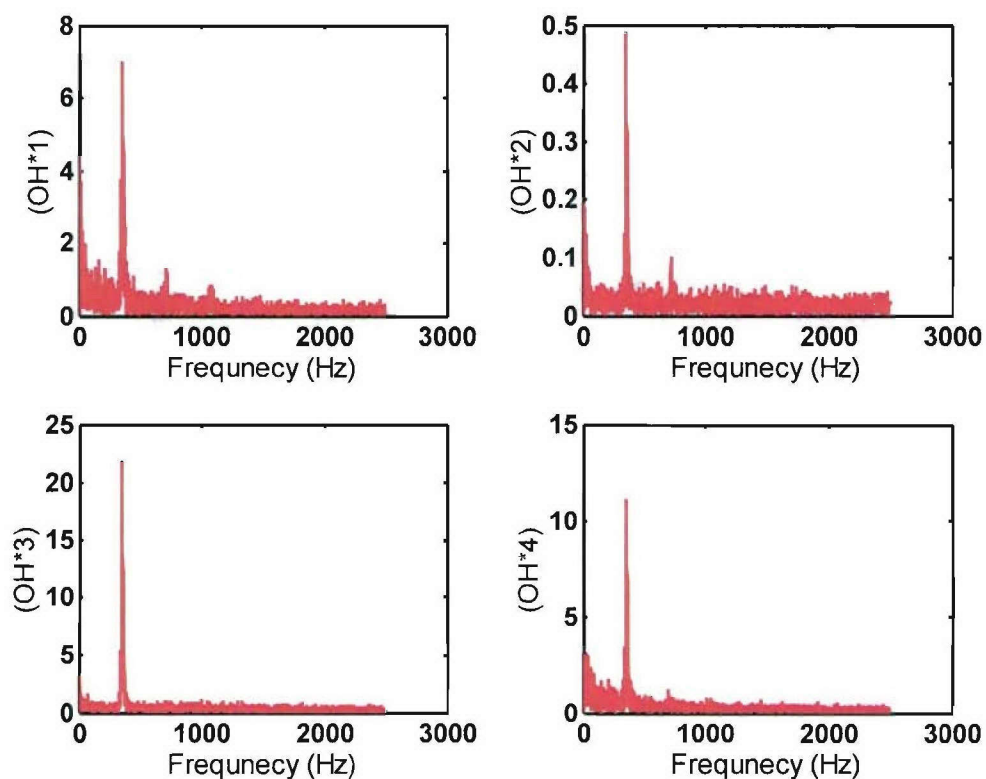

Figure 6.27: Spectra of OH* at unstable combustion: Jet-A, 50% pilot fuel, S5545C45, T_3=230°C, L_{mt}=0, R_{eD}=34600, Φ=0.6.
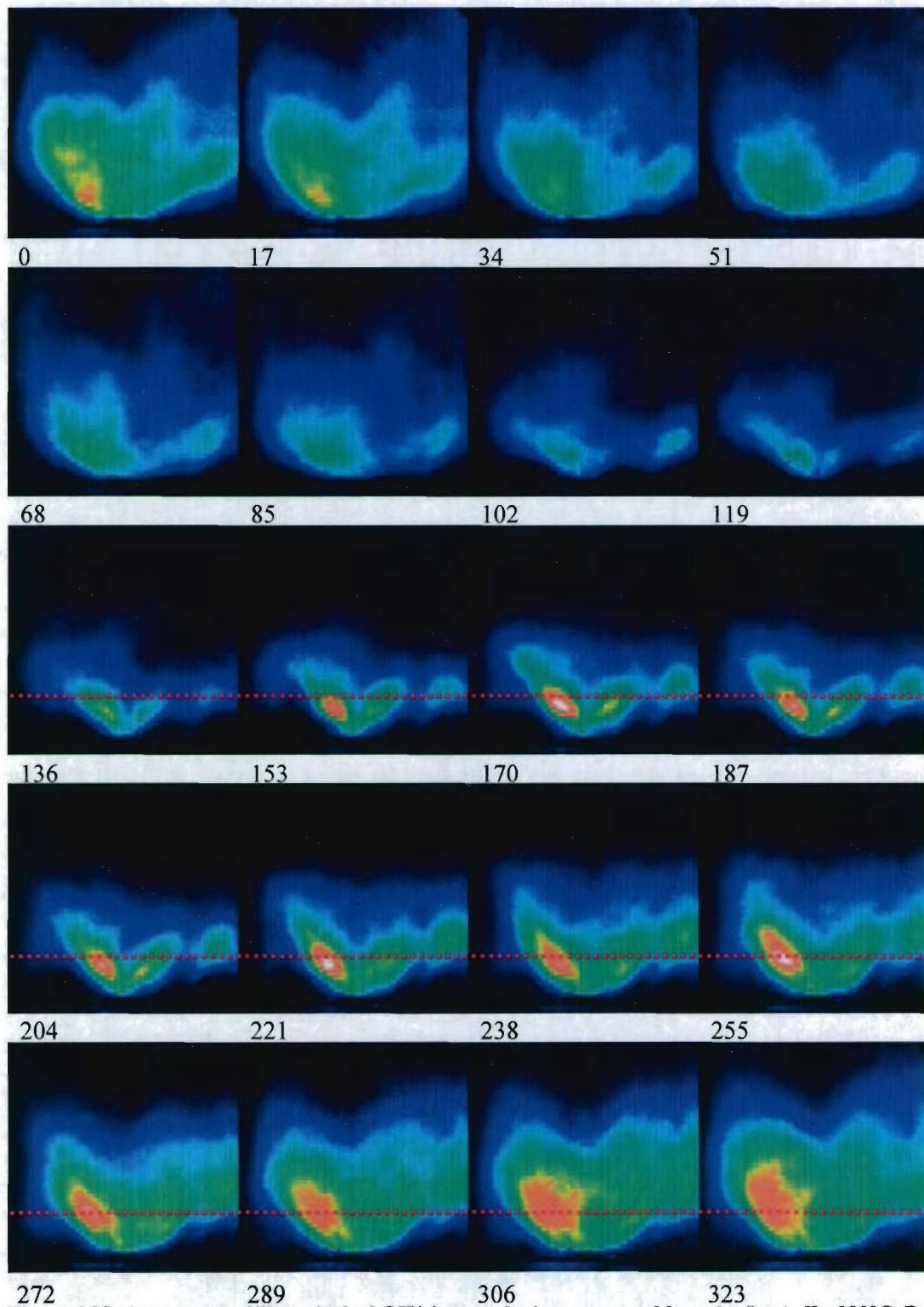
Figure 4.28: A sequence of Phase-locked OH* images during one unstable cycle. Jet-A, T_3=230°C, R_{eD}=22800, L_{mt}=0, S5545C45, Φ=0.6, 50% pilot fuel.

Unlike gaseous fuel, the spray combustion of Jet-A fuel is quite asymmetric. Figure 4.28 is a sequence of OH* chemiluminescence images within one cycle of instability. The flame is anchored to the nozzle during the unstable combustion process, extending downstream along two leaves with an intersection angle about 90°. Starting from the weakest flame at 119°, the reaction gets intense on the left side to form a strong reaction core. Although the length of the flame gradually increased, as well as the flame intense and flame area from 136 to 255°, the intense flame core only slightly moved. Intensity of this reaction core reduced when the flame further increases its area from 272° to 323° and then decreases into next cycle. During this instability cycle, no clear flame curvature was observed to claim vortex involved in this process. Therefore, it is more likely the fuel pulsation related to the jet velocity pulsation causes periodic heat release and sustains combustion instability.

For ethanol, the spectra and phase angle relationship (Fig. 4.29) are quite similar with those of Jet-A. Different from Jet-A, two more flame leaves are formed in addition to the central two. Also, the central flame is born at very close to the fuel nozzle, growing up and then moving toward downstream. It can be clearly seen that the combustion mainly occurs along the region fuel sprays: first concentrates on fuel stripes and then spreads out when fuel is vaporized and mixed with surrounding air. For gaseous fuel, no such distinct flame stripes can be discerned.

All these combustion instabilities may be categorized as longitudinal mode because the dominant flame oscillation is in the axial direction and the phase angles of all optical signals are not different much. The combustion instability, depending on the fuel types and geometries, manifests as different flame motion. The oscillation in flame, when combustion instability occurs, is triggered by the oscillation from pressure. This is evidenced by the lead of oscillation growing in pressure than flame and the enclosure of instability frequency within combustion

noise band. The curvature of flame with the gaseous fuel may be the manifestation of vortical structure involved in the instability process. For liquid fuel, the periodic variation in the emanating jet strength can modulate the fuel spray and thus affect the local equivalence ratio. The vortex dynamics, as well as the velocity variation of swirling jet, can play an important role for driving combustion instability. The essential information can be obtained from velocity flow field measurement phase-locked with pressure oscillation.
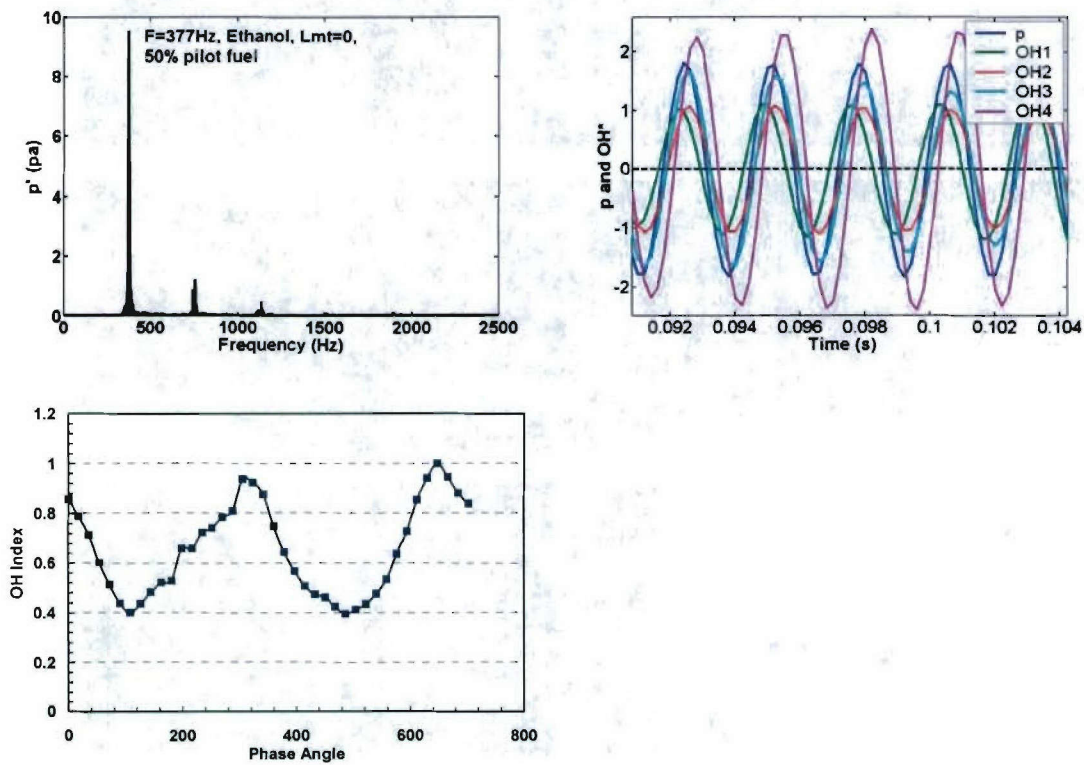

Figure 4.29: Dynamic signals at unstable combustion: (a) Spectra of p'; (b) Comparison of signals of p' and OH*; (c) Integrated OH* from images. Ethanol, T_3=230°C, R_{eD}=34600, L_{mt}=0, S554545, Φ=0.75, 50% pilot fuel.
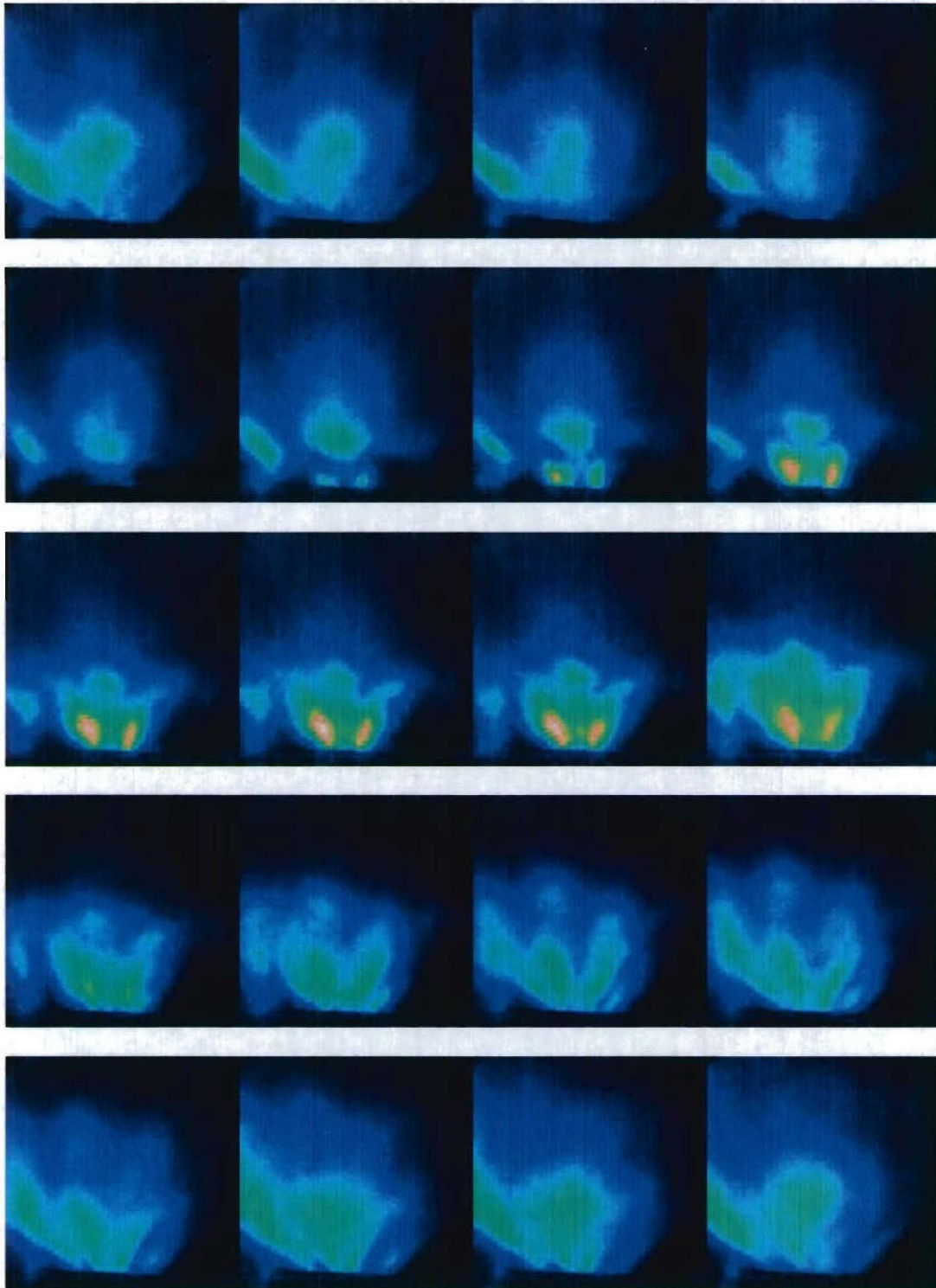
Figure 4.30: Phase locked OH*. Ethanol T_3=230°C, R_{eD}=34600, L_{mt}=0, S5545C45, Φ=.75.

4.5 Flow Dynamics and Combustion Instability

3-D PIV was used for resolving the flow dynamics during combustion instability. Unstable combustion occurs at $\Phi=0.8$, 46% pilot fuel, $T_3=230°C$ for co-rotating swirler S554545. Ethanol fuel was used for preventing soot covering the optical window. When combustion occurs, the flow field will be complicated by the variation in fuel/air distribution, local combustion intensity and temperature field, compared with isothermal cases. During the unstable combustion, pressure oscillation had peak-to-peak magnitude of 1 psi at 414 Hz. Trigger signal generated by the microphone was sent to the PIV and ICCD cameras. Both PIV and ICCD were triggered at the rising edge of the 5 volts trigger signal. The sequences of 3-D vector and OH* images within one instability cycle are shown in Fig. 4.31. Fig. 4.32 depicts the normalized pressure oscillation, light oscillation detected by optical fiber, and OH* index integrated from OH* images. The three signals fell in phase when combustion instability occurs. Along the inner edges of jets, i.e. along the boundary of the CRZ zone, two large vortical structures form at 0° and gradually reduce their strength until disappear at 126°. Subsequently, the large vortices reformed at 252° (Fig. 4.31a). The OH* images (Fig. 4.31b) show that the flame starts curving at the bottom from 189° corresponding to the starting point of vortices forming at the center, and then shows "horn" shape structure when the vortices clearly formed at 252°. Following this phase, the vortical structure stretched out. The flame structure became more diffused, and fluctuated in the axial direction.
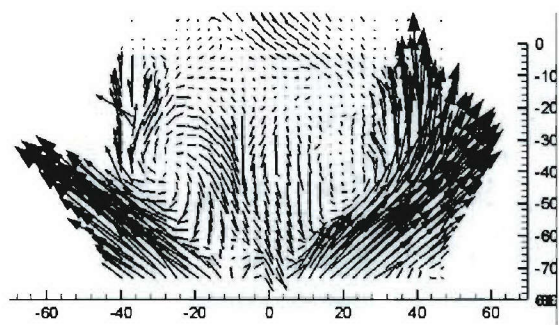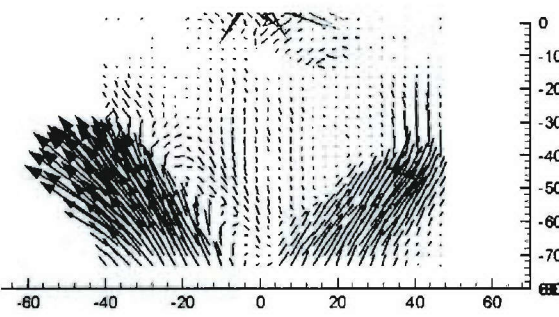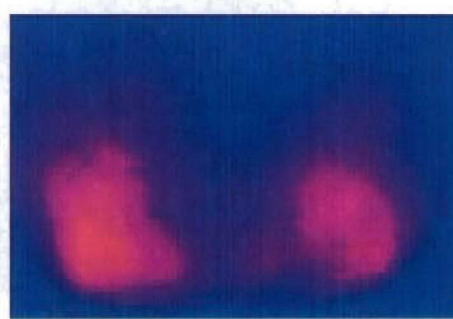
0°
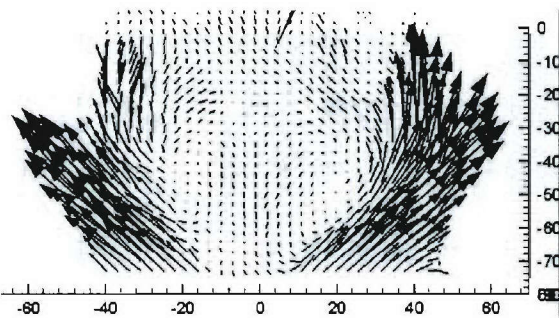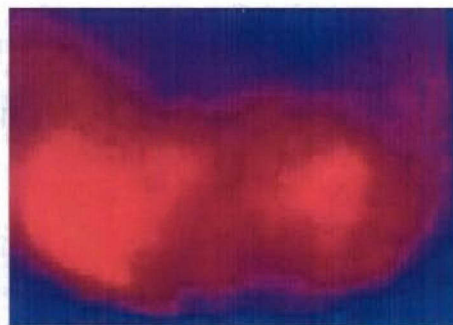
63°
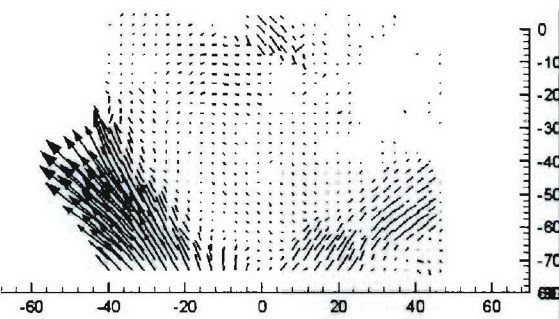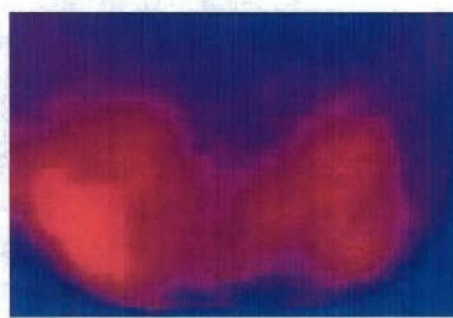
126°

189°
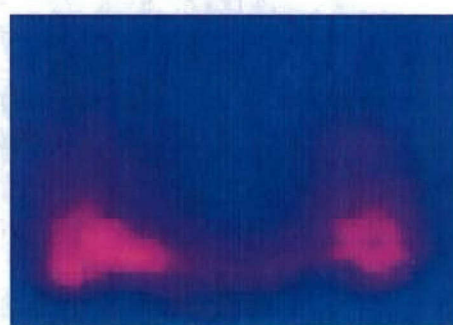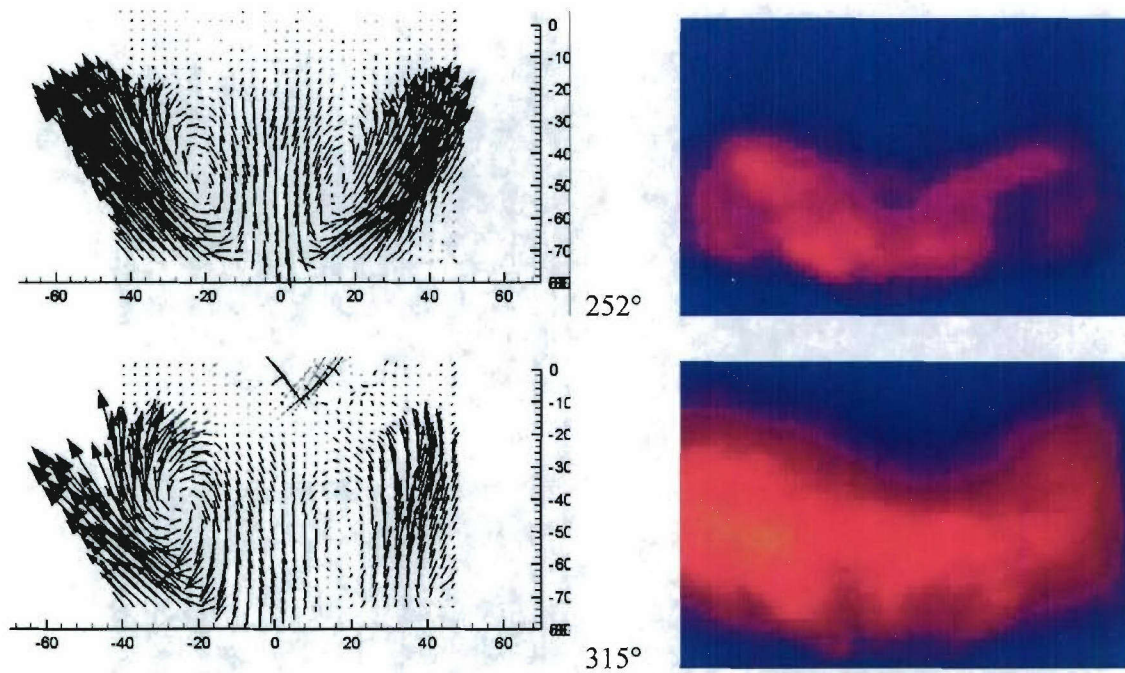
Figure 4.31: Sequences of 3-D vector plots and OH* images phase-locked with pressure oscillation signal. Ethanol, $\Phi = 0.8$, pilot fuel =46%, T_3=230°C. Instability frequency is 414Hz.
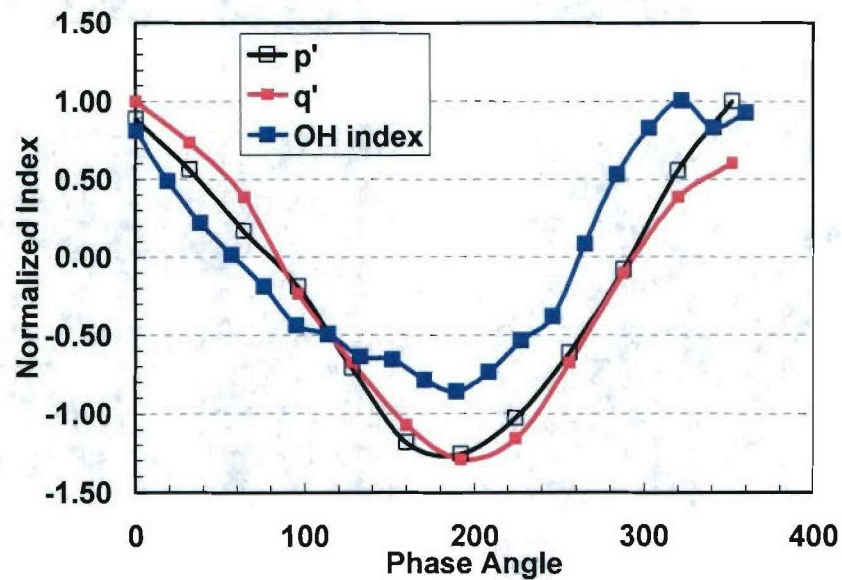
Figure 4.32: Normalized pressure oscillation p', light oscillation q' and OH index integrated from OH image within one period for combustion instability.
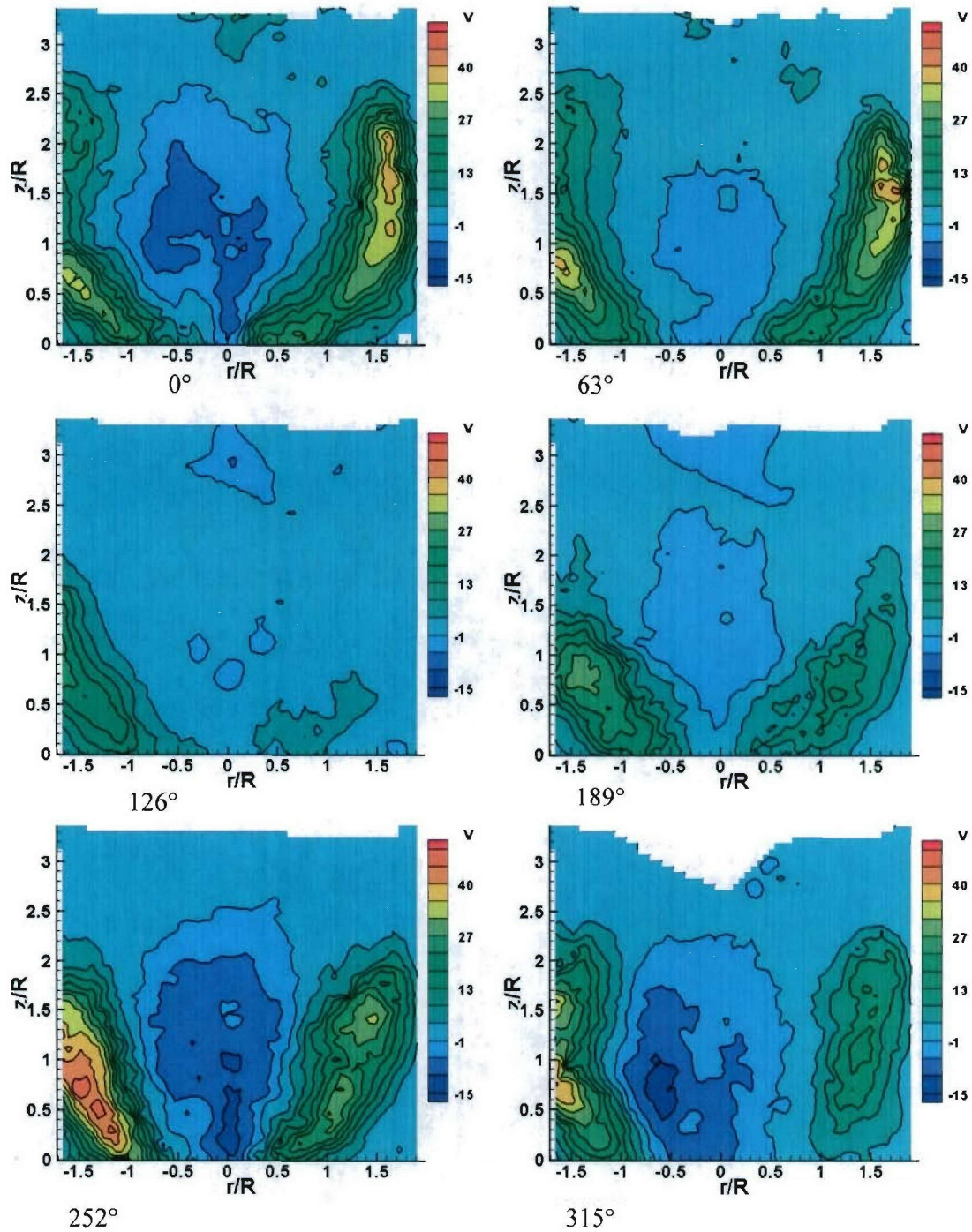
Figure 4.33: Contours of axial velocity at different phase angles of one instability cycle.

This dynamic behavior was quasi-axisymmetric. Meanwhile, the jet strengths on the left and right sides changed asymmetrically: the left jet strength increased from 0° to 252°, achieving its

maximum at 252°, whereas the right jet strength decreased from 0° to 126° and regained its strength thereafter. Two points need to be emphasized: (1) the jet strength, i.e. velocity magnitude, oscillates with pressure oscillation cycle; (2) the asymmetric motion of jet on the left and right sides. The first point was proposed by Poinsot et al. (1987) as one main feature that characterizes vortex-driven instability together with convection, acceleration and combustion of the vortex, and unsteady heat release. As shown in Fig. 4.33, the central recirculation zone decreased and increased its reversed flow magnitude in synchronization with the central vortices dynamics. Meanwhile, the axial velocity of the jet periodically changes with the CRZ dynamic. At phase 126°, the velocity field of CRZ is almost uniformly at zero, being a quasi-stagnation zone. The dynamical behavior of CRZ under combustion instability is also observed by Dawson et al. (2004). They stated that CRZ exhibited a sinusoidal response to the pressure fields with similar behavior for the recirculated flow rate.

Although the nearly axisymmetric evolution of the central vortices and OH* imaging shows clearly the flame oscillating in the longitudinal direction and strongly suggests a longitudinal mode, the asymmetric evolution of emanating jets complicated the combustion dynamics, making the combustion mode less clearly defined as purely either longitudinal or azimuthal mode. To compare the flow field quantitatively, the mean and RMS velocity profiles at $z/R=1$ are extracted from the contours and shown in Fig.4.34. From 0° to 315°, peak axial velocity decreases from 35m/s to about 1m/s and then increases to 25m/s, while the reversed velocity changes from -8 to 0 and -10 m/s. Surprisingly, the tangential velocity (highlight in the right side of the figure) reverses its direction within one cycle, starting -20m/s (63°) to 0 (126°) and then +20m/s (252°). This suggests that the flow locally circumferentially vibrates when the flow oscillates mainly in the longitudinal direction. The radial velocity, together with the axial

velocity, characterizes the jet motion in the direction of about 38° (inverse tangential of peak radial velocity versus axial velocity).
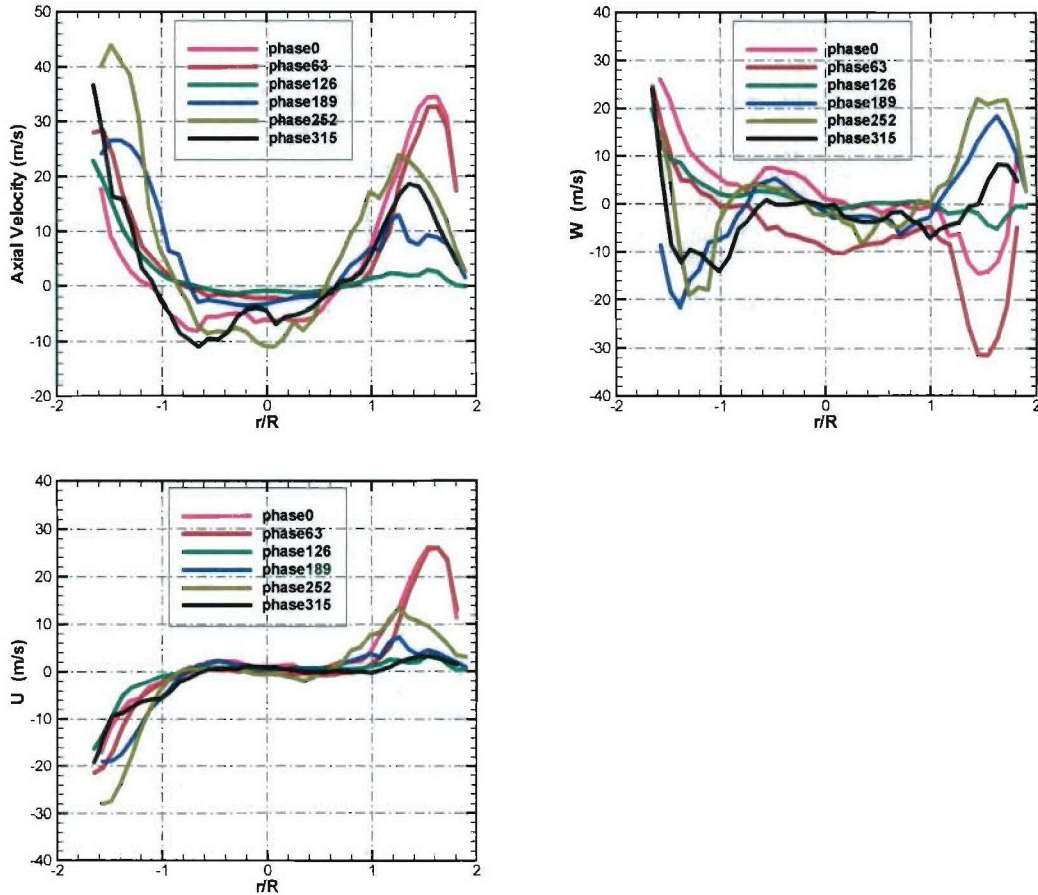
Figure 4.34: Comparison of Mean axial (V), tangential (W) and radial (U) velocity components at z/R=1 for different phase angles of one cycle in combustion instability. Ethanol, 46% pilot fuel, T_3=230°C.

The instability frequency, 414Hz, was somewhat closer the quarter wave mode frequency based on the tube length (40 cm) and the combustion gas temperature (estimated 1500K), which was about 450Hz. For swirl-dump combustor, the superposition of swirl effect to the emanating jet behavior of dump combustor, causes more complicated flow fields and may bring extra error for linear acoustics analysis from which the quarter wave mode is derived. The local vibration of

tangential velocity can be one evidence of the swirl effect on this combustion instability. The vortices along the inner jet edge, which are observed with phase-locked flow field measurements for PVC, may play an important role in the combustion instability process of swirl-dump combustor. This point emphasizes the influence of PVC in swirl to combustion instability which is less noticed in previous research.

Based on the cold flow and combusting flow fields' data, it may be proposed that vortex-driven combustion instability in swirl-dump combustors is related to the oscillation of swirling jet strength and the vortical dynamics of the vortices formed at the inner edge of swirling jet. These vortices are excited and move along the jet direction when combustion instability occurs. This oscillation is also affected by PVC as evidenced by the asymmetric change of the jet strength in both isothermal flow and combustion cases and the local vibration of tangential velocity.

4.6 Summary

Combustion dynamics of swirling flow closely correlate to the fluids dynamics. The behavior of flame close to LBO and at occurrence of instability are extensively studied by OH*/CH* radical sensors, pressure transducers and Phase-locked OH* imaging. The conclusions are delineated as following:

1) When approaching LBO, the increment of RMS OH* radical intensity within CRZ is manifested for propane, Jet-A, ethanol fuel with/without mixing tube and different swirler configurations. It is a good option for LBO pre-detection provided optical port is available in the practical facility.

2) The flame oscillation is specific to different locations. The oscillation of flame at the central recirculation zone is different from that at the jet flame region. The flame is most stable when

oscillates at high frequency and small magnitude. This indicates a potential method for LBO extension by modulating the flame at high frequency when approaching LBO.

3) LBO is affected by swirler configuration and mixing tube, but is not sensitive to air assist. Generally to say, co-rotating swirler has lower LBO limit than counter-rotating swirler. The mixing tube tends to make the combustion unstable and worsen the LBO.

4) Combustion instability, indicated by RMS p', was shown correlated to the flame oscillation in CRZ. Therefore, reducing CRZ region may be an option for control combustion instability. The counter-swirler manifests lower magnitude oscillation compared with co-swirler because it has smaller recirculation zone.

5) There is certain tradeoff between LBO and combustion instability. The good option for LBO may not be a good option for reducing instability.

6) Combustion instability may manifest in many different flame oscillation styles, depending on the fuel properties, premixed and non-premixed combustion. The oscillation in jet velocity and associated vortical structure are proposed to be the main driven mechanism for the instability. The phase-locked PIV measurement provides valuable information in understanding combustion instability and its control.

CONCLUSIONS

This study extensively investigates the swirling flow field, its dynamic structures, combustion dynamics, emission characteristics, and the temperature field of a multiple swirl gas turbine combustor by utilizing state-of-art laser diagnostics, gas analyzer and optical sensing. Through this study, we have explored the effects of flow parameters, a variety of passive and active control approaches on control of emissions and combustion dynamics, both for non-premixed and premixed combustion with gaseous and liquid fuels. The detailed measurements of swirling flow velocity field provide insight for understanding the three dimensional unsteady flow and the correlation between the fluids dynamics and combustion dynamics, both LBO and unstable combustion, and NO_x and CO emissions. Application of a novel Tunable Diode Laser in-situ temperature sensor and a transient non-thermal pulsed plasma actuator in gas turbine combustors demonstrates their potential in control of combustion dynamics and emissions.

The main conclusions are delineated as following:

1) Systematic study of swirling flow in non-reacting and reacting conditions is an efficient and effective approach for investigating complex flows and correlating combustion dynamics to fluids dynamics. The knowledge of velocity flow field and large vortical flow structures obtained from isothermal flow measurement is helpful in understanding phenomena in combustion cases.

2) Passive control approaches, including swirler configurations, exhaust nozzle contraction ratios, mixing tube length, are shown to be effective for control of flow field, emissions and combustion dynamics but each has certain limitations.

    a. The co-rotating swirler, which has larger swirl number and therefore forms larger central recirculation zone and stronger turbulence velocity within this zone, normally

generates more uniform and lower temperature distribution and less NO_x formation compared with the counter-rotating swirler for gaseous fuel and ethanol. But this superiority is less significant when Jet-A is used and fuel/air mixing is not sufficient. The co-rotating swirler is also shown to be advantageous in leaner LBO limit. On the other hand, the co-rotating swirler is easier to run into unstable combustion because larger CRZ is more susceptible to disturbance.

b. The mixing tube promotes the formation of strong jet coming from the tube and the upstream movement of large vortical structures, intensifies turbulence velocity and strain rate along the swirling jet. The enhanced jet velocity pushes and extends the high temperature region downstream, forms a lower temperature dome zone and less NO_x formation. The movement of large vortical structures into the mixing tube enhances the combustion dynamics and generates extra combustion acoustic noise, allowing unstable combustion occurring easier and reducing the operating range.

3) As one of active control options, air assist is demonstrated to be promising way of reducing NO_x and suppressing combustion instability without affecting the LBO limit. By helping fuel penetration, the air assist evens temperature distribution and reduces the oscillations of flame both within CRZ and the shear layer flame zone. The proper combination of air assist with passive control approach such as mixing tube can reduce NO_x and CO simultaneously.

4) LBO can be pre-detected based on the flame oscillation in the central recirculation zone. It is typical for both gaseous and liquid fuel combustion at non-premixed and premixed conditions that the flame oscillations, which are represented by oscillations of OH*/CH* radicals, reduces to the minimum at certain equivalence ratio away from LBO and

gradually increases when approaching the LBO. It is also shown that the most stable combustion is characterized by high frequency low magnitude oscillation whereas the flame close to LBO oscillates at much lower frequency. This is a very useful implication in future high frequency pulsation for extending LBO.

5) Combustion instability of this multiple swirl combustor manifests in different flame oscillation manners but closely relates to swirling jet velocity oscillation and the dynamics of vortical structures within CRZ. The oscillation in jet velocity, either directly causing fuel pulsation and thus equivalence ratio or indirectly causing periodic vortex formation and flame oscillation, bridges the coupling between heat release and acoustic fluctuations. Phase-locked PIV measurement and OH* chemiluminescence clearly demonstrate this relationship in combustion instability cycle.